4-11-2023

Impact of Particle Sizes on MRI Signal Relaxation in Phantoms for Assessment of Hepatic Steatosis and Iron Overload

Sarah Caroline Brasher

Impact of Particle Sizes on MRI Signal Relaxation in Phantoms for Assessment of Hepatic Steatosis and Iron Overload

by

Sarah Caroline Brasher

A Thesis

Submitted in Partial Fulfillment of the

Requirements for the Degree of

Master of Science

Major: Biomedical Engineering

The University of Memphis

May 2023

Acknowledgements

First and foremost, I would like to express my deepest gratitude to my major advisor, Dr. Aaryani Sajja, for her continual support throughout these past two years. Her presence has been a rock—a resilient and steadfast foundation I could always rely on for matters both personal and academic. Without her patience, guidance, and remarkable knowledge, this thesis would not have been possible. Her persistence in the pursuit of science and education is admirable, and I know she will accomplish great things in the years to come.

Additionally, I would like to thank the members of my committee: Dr. Omar Skalli, Dr. Amy Curry, and Dr. Carl Herickhoff. Their encouragement and insightful comments have tremendously improved the content of this work. Special thanks also goes to Dr. Felio Perez who patiently helped me in operating the scanning electron microscope in tandem with Dr. Skalli. Also, I would like to give my sincere appreciation to Dr. Ernő Lindner for his helpful advice in academics and giving spirit. I will miss our little conversations by the coffee machine.

To all my fellow lab members, thank you for your support and companionship. You made the good days excellent and the hard days worthwhile. I look forward to seeing where everyone is in the future. I must also extend my appreciation to my close friends who never failed to encourage me and always provided a place to unwind.

Last but certainly not least, I would like to express my gratitude to my family— my mom, dad, and two brothers. To my parents, the depth of your support these past two years truly had no end. No complaint fell on deaf ears, and no problem was too petty to help. I simply could not have done it without you. To my brother JM, thank you for keeping me grounded on what the future holds. Finally, to my brother Stephen, thank you for being my best friend all these years. You put up with a lot of nagging, so thanks for sticking with me.

Preface

Chapter III, a comprehensive review on MRI phantom literature, is composed of the following journal article: “Quantitative MRI of Diffuse Liver Diseases: Techniques and Tissue-Mimicking Phantoms”, written for submission to *Magnetic Resonance Materials in Physics, Biology and Medicine (MAGMA)*.

Abstract

Magnetic Resonance Imaging (MRI) is emerging as a powerful tool to non-invasively evaluate diffuse liver diseases such as hepatic steatosis and iron overload. To test new MRI techniques, phantom studies are utilized in place of patients but often do not consider the microscopic interactions of particles suspended in the media which may cause a notable difference in the signal. Hence, this study investigates the impact of differing particle sizes on the magnetic resonance signal using phantoms. To accomplish this, steatosis phantoms were created using two different mixing methods to control droplet size and while combination iron-fat phantoms featuring iron particles of differing diameters were used to emulate hepatic iron overload. Signal behavior from both sets of phantoms were resolved using linear calibrations to determine values from two known biomarkers, fat fraction and R2*, for steatosis and iron overload, respectively. Overall, evidence showing that particle size impacts the signal to a significant degree remains inconclusive, but fitting model performance in biomarker quantification varied. This study demonstrates different sequencing and post-processing assessments are critical for the analysis of sensitive biomarkers such as R2* and FF.

Table of Contents

List of Tables

Chapter III. Quantitative MRI of Diffuse Liver Diseases: Techniques and Tissue-Mimicking Phantoms

Chapter IV. Impact of Particle Sizes on MRI Signal Relaxation in Phantoms for Assessment of Hepatic Steatosis and Iron Overload

Appendix

List of Figures

Chapter II. MRI Physics

Chapter III. Quantitative MRI of Diffuse Liver Diseases: Techniques and Tissue-Mimicking Phantoms

Abbreviations

ADC	Apparent Diffusion Constant
ARMA	Autoregressive Moving Average
B-Gel	Bovine Skin Powder
BNF	Bionized NanoFerrite
CAG	Carrageenan-strengthened Agarose/Gadolinium Gel
CPMG	Carr-Purcell-Meiboom-Gill
CRN	Clinical Research Network
CT	Computed Tomography
DSPIO	Dextran-coated Superparamagnetic Iron Oxide
DWI	Diffusion-Weighted Imaging
ECM	Extracellular Matrix
FDA	Federal Drug Administration
FID	Free Induction Decay
FF	Fat Fraction
FFT	Fast Fourier Transform
FOV	Field of View
FS	Fat Suppression
DWI	Diffusion Weighted Imaging
G	Shear Modulus
G’	Storage Modulus
G_x	Frequency Encoding Gradient
G_y	Phase Encoding Gradient
G_z	Slice Selection Gradient
GRE	Gradient Echo
H&E	Hematoxylin and Eosin
HIC	Hepatic Iron Content
IR-Snapshot	Inversion Recovery Snapshot Fast Low Angle Shot
IR-UTE	Adiabatic Inversion Recovery Prepared Ultrashort Echo Time
ISMRM	International Society for Magnetic Resonance in Medicine
IVIM	Intravoxel Incoherent Motion
mGRE	Multi-Echo Gradient Echo
MOLLI	Modified Look-Locker Inversion Recovery
MR	Magnetic Resonance
MRE	Magnetic Resonance Elastography
MRI	Magnetic Resonance Imaging

MRS	Magnetic Resonance Spectroscopy
NAFLD	Non-Alcoholic Fatty Liver Disease
NASH	Non-Alcoholic Steatohepatitis
NIST	National Institute of Standards and Technology
NLI	Non-Linear Inversion
NLSQ	Non-Linear Least Squares
NMR	Nuclear Magnetic Resonance
QIBA	Quantitative Imaging Biomarkers Alliance
QSM	Quantitative Susceptibility Mapping
PAA	Polyacrylamide
PVA	Polyvinyl Alcohol
R2	Rate of Transverse Relaxation
R2*	Rate of Transverse Relaxation with Inhomogeneities
RF	Radio Frequency
ROI	Region of Interest
RSNA	Radiological Society of North America
SASHA	Saturation Recovery Single-Shot Acquisition
S	Stiffness
SE	Spin Echo
SE-EPI	Spin Echo Echo Planar Imaging
SE-IR	Spin Echo Inversion Recovery
SEM	Scanning Electron Microscopy
SIR	Signal Intensity Ratio
SNR	Signal to Noise Ratio
SPIO	Superparamagnetic Iron Oxide
SS-EPI	Single-Shot Echo Planar Imaging
T1	Longitudinal Relaxation
T2	Transverse Relaxation
T2*	Transverse Relaxation with Inhomogeneities
TE	Echo Time
TR	Repetition Time
TSE	Turbo Spin Echo
USPIO	Ultra-small Particles of Iron Oxide
UTE	Ultrashort Echo Time
VFA	Variable Flip Angle

Chapter I

Introduction

Motivation for Study

Iron is an essential mineral in many metabolic processes, particularly for the synthesis of the oxygen transport proteins, hemoglobin and myoglobin [5]. In the case of an imbalance of iron, homeostatic mechanisms can only regulate iron by limiting absorption during digestion as the human body has no natural physiological processes for excreting iron [6]. Thus, excess iron can build up in the liver, the primary organ for iron storage, under conditions of hereditary hemochromatosis or transfusional hemosiderosis [7]. In addition to iron storage, the liver plays a vital role in lipid metabolism [8]. Hepatic steatosis, the abnormal deposition of lipids in the liver, is a hallmark characteristic of many diffuse liver diseases such as viral hepatitis and alcoholic or nonalcoholic fatty liver disease [9,10]. Co-occurrence of hepatic steatosis and iron overload is well documented [11], and the disease progression of either or both diffuse liver diseases can lead to fibrosis, cirrhosis, and ultimately liver failure [10].

Liver biopsy is the current gold standard for evaluating hepatic steatosis and iron overload, but it has a few major limitations. Firstly, steatosis and iron overload can be heterogeneously distributed [12,13], and the small sampling size of the biopsy specimen lacks information on the spatial distribution of the liver, thus causing high sampling variability in quantitative measurements [7,14]. Biopsy is a painful and invasive procedure with a risk of bleeding and infection, leading to suboptimal patient compliance [15,16]. Additionally, frequent assessments of diffuse liver disease are needed to guide treatments, requiring multiple biopsies. Because of these drawbacks, MRI has arisen as a non-invasive alternative to liver biopsy and is

becoming increasingly recognized in the clinical sector to monitor hepatic steatosis and iron overload [17,18].

Quantitative MRI techniques for evaluating hepatic steatosis and iron overload have been developed but have limitations on the range of fat and iron deposition they can measure. To advance these techniques, extensive testing must occur on specified pulse sequences and scanning hardware. MRI examinations routinely take approximately 20-60 minutes per session [19], so acquiring volunteers to test new MRI sequences can be challenging especially across multi-site studies. Hence, researchers utilize imaging phantoms, specialized standards equipped to emulate a certain disease, to develop new MRI techniques. These phantoms contain materials that manipulate the MRI signal to produce characteristic effects that would be seen under certain pathologies, therefore targeting different MRI biomarkers. However, diffuse liver phantoms in the literature display little to no standardization in materials, volume, protocol, and even targeted biomarkers for a particular disease.

For this thesis, a question of particular interest is that concerning the microscopic interactions of iron and fat particles in the phantom media on the MR signal. In vivo, hepatocytes exist in a range of sizes between 20-25 μm in diameter, while steatotic lipid globules grow no larger than 15μm. Additionally, iron is usually stored in ferritin molecules that cluster in sizes of 50-70nm. However, under severe iron overload, hemosiderin is the primary iron storage molecule and clusters to sizes of 0.1-2 μm. In phantom literature, these physiological sizes are often not considered in the particles used to emulate diffuse liver disease and may show a much larger difference in magnitude than what is seen in vivo. This is a concern as it is theorized that substances such as iron will preferentially affect the signal produced by water over fat due to geographical limitations and solubility. Thus, adjusting the sizes of these particles may allow for

more or less interactions between iron, fat, and water, all of which affect the MR signal significantly.

Hence, there is a gap in our understanding of the impact of particle size on MR signal behavior. The following sections will establish fundamental MR techniques related to diffuse liver disease before culminating into a study investigating the impact of iron and fat particle sizes on the MRI signal. A foundational segment on MRI basics, sampling, and pulse sequences will first be discussed in Chapter II before moving onto a comprehensive literature review on hepatic phantoms in Chapter III. Following this, an analysis of the microscopic interactions in phantom media will be conducted in Chapter IV by varying sizes of fat and iron particles in phantoms emulating hepatic steatosis and iron overload on a scale relative to molecules seen in in vivo liver tissues. These phantoms will use two biomarkers that encompass clinical ranges: fat fraction (FF) for hepatic steatosis and R2* for hepatic iron overload. Additionally, particle size will be validated using light microscopy and scanning electron microscopy (SEM), and various signal fitting models will be tested for accurate and precise quantification of R2* and FF. Using these methods, an investigation on the impact of particle size on MR signal behavior will be performed. Finally, a discussion on potential expansions and adaptations to this study will be elaborated on in Chapter V.

Chapter II

MRI Physics

Basics of MRI Physics

While MRI is favored in most clinical environments due to its ability to provide spatial information, all MRI scanners operate based on the physical phenomenon of nuclear magnetic resonance (NMR). Since its development by Purcell [20] and Bloch [21] in 1945, NMR has been used as an analytical technique for elucidating chemical structures in solids by manipulating specific atomic species using weak oscillating magnetic fields. Only nuclei which have an odd number of neutrons and/or protons possess net spin and are considered NMR active and can display this phenomenon [22]. Many NMR-active species exist, including ^{1}H, ^{13}C, ^{15}N, and ^{31}P, all present in living tissues [23-25]. However, ^{1}H is utilized in clinical MRI scanners due to its relative biological abundance [26].

The NMR phenomenon begins with the presence of a strong, static magnetic field aligning NMR-active nuclei with or against the field [26]. This will cause the nuclei to precess at a unique Larmor frequency, thereby generating a spinning magnetic moment that can be represented as a net magnetization vector in the direction of the static magnetic field [26,27]. The equation for a given Larmor frequency can be seen below,

$$\omega_0 = \gamma B_0$$

where ω_0 is the Larmor frequency in MHz, γ is the gyromagnetic ratio of the nuclei, and B_0 is the static magnetic field strength in Tesla [27]. A coil in the scanner will then generate a current to produce a radiofrequency (RF) pulse, therefore inducing an oscillating magnetic field. This RF pulse will tip the net magnetization vector of the nuclei from the z-axis to the xy-plane with a flip angle depending on the strength and duration of the RF pulse. A secondary RF receiver coil will

detect the induced current caused by a change in the net magnetic field via electromagnetic induction. Inevitably, the spins of the nuclei will become dephased due to the interference of random thermodynamic interactions with neighboring nuclei, and the signal induced by the magnetic moments of each nucleus will decay as more return to the direction of the static magnetic field [28]. This phenomenon is known as relaxation, where the recovery of the longitudinal magnetization vector is termed T1 relaxation, and the loss of the transverse magnetization vector is termed T2 relaxation which can be shown graphically as a free induction decay (FID) [29]. Additionally, local field inhomogeneities can accelerate the signal decay in an effect known as T2* relaxation [30]. The preceding concepts are illustrated in Figure 1.

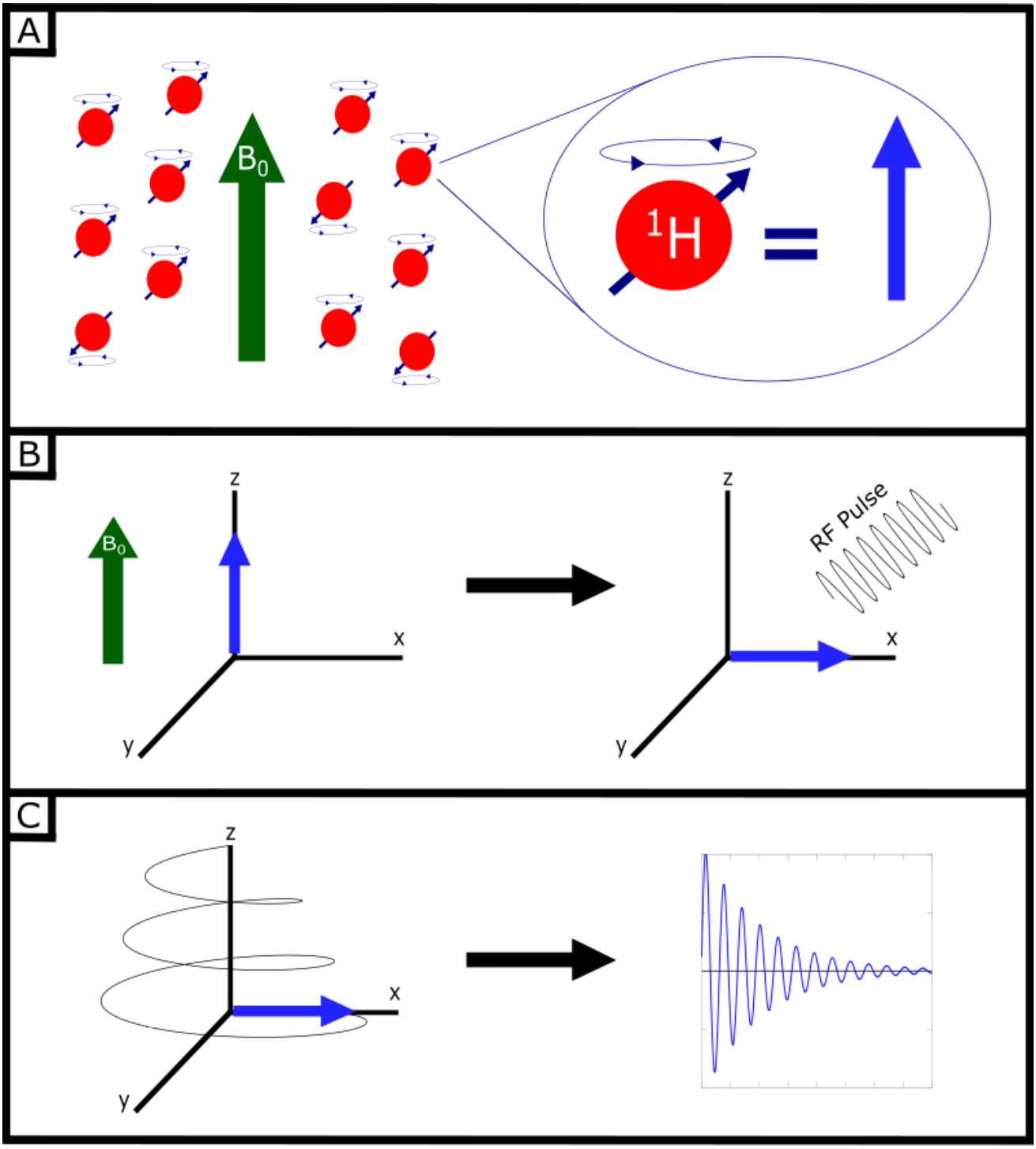

Figure 1. Overview of basic MRI physics. (A) Precession of NMR-active nuclei align toward the static magnetic field, B_0, and can be represented as a net magnetization vector. (B) The net magnetization vector is tipped from the direction of B_0 on the z-axis to the xy-plane by an RF pulse. (C) Relaxation of the magnetization vector results in an FID signal as the signal is lost in the transverse plane.

Cartesian and Radial Sampling

Using the Fourier transform, any oscillating signal can be broken up into a series of sinusoidal waveforms [31]. Hence, an FID produced via MRI can be translated into the frequency domain using the Fourier transform and represented in two dimensions through k-space [32,33]. In this visual representation of frequencies, the contrast information of the signal primarily resides in the center of k-space while the high-resolution spatial information resides in the periphery [33]. This information is filled into k-space by manipulating MRI gradients that subtly change the field strength [33]. Specifically, phase encoding (G_y) and frequency encoding (G_x) gradients store information on the y and x-axis, respectively. Performing an inverse Fourier transform can therefore recover the spatial MRI image from the frequency domain [34]. However, how one samples the acquisition through k-space plays an important role in MRI image acquisition and can create pronounced impacts on the final MRI image.

The standard method of sampling k-space data in most clinical MRI sequences is through Cartesian (rectilinear) sampling [34]. As seen on Figure 2, this method involves iteratively recording regularly spaced parallel data elements from left to right using independent phase and frequency encoding gradients until the entirety of k-space is filled [34]. This allows for the matrix of data elements to be placed into an array for the efficient processing through fast Fourier transform (FFT) to create MRI images [34]. Alternatively, non-Cartesian methods such as radial sampling have been gaining popularity for their unique benefits. Here, radial sampling involves the generation of center-out vectors in k-space formed by the utilization of simultaneous phase and frequency encoding gradients [1]. However, these vectors contain data elements that do not neatly settle into a rectangular matrix, so they must undergo “re-gridding” into a Cartesian matrix format before undergoing FFT [1,34].

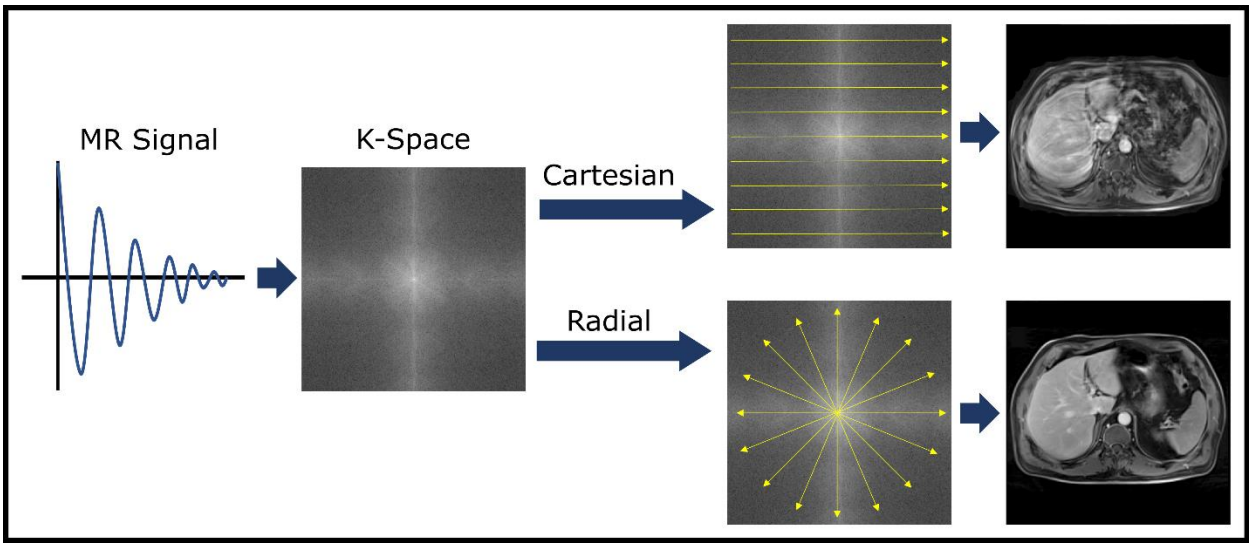

Figure 2. Schematic of Cartesian and radial sampling of k-space. Performing Fourier transform on a spatial 2D signal provides data that can be represented in the frequency domain through K-space. Phase and frequency encoding can be manipulated to perform cartesian (left to right) and radial (center-out) acquisitions followed by inverse Fourier transform to recreate the spatial image. The images provided are of a free-breathing abdominal exam with motion artifacts [1].

In today's clinical environment, Cartesian sampling remains the most dominant modality, but other approaches are becoming more popular in light of recent research developments. The main advantage of Cartesian sampling is that it can be simply transformed into an image with the FFT without additional processing. However, radial sampling is less sensitive to motion artifacts and has better contrast due to the oversampling of the center of k-space [1]. This redundancy allows for the correction of any movement in the signal as more is sampled at the center [1]. Nonetheless, radial sampling is prone to distinctive streaking artifacts that emerge from object motion or bright intensities in the image, but the streaks are relatively easy to identify and usually do not confound a diagnosis if the radiologists/technicians are trained prior [1,35]. Radial sampling also utilizes simultaneous phase and frequency encoding gradients without increasing the scan time, unlike Cartesian methodologies that use the gradients sequentially [1]. However, radial trajectories have less efficient coverage of k-space in the periphery, causing low resolution and image blurring [1].

GRE and UTE Sequences

In MRI, the physical properties of an FID can be manipulated by adjusting a number of parameters in the internal gradients of the scanner including echo time (TE), repetition time (TR), flip angle, echo train length, and field of view (FOV), among others [30,36]. By utilizing presets of these parameters, unique pulse sequences are generated to highlight specific physical phenomena at the discretion of the user. For diffuse liver diseases such as iron overload and steatosis, sequences that utilize the properties of chemical shift, i.e., the difference in resonance frequencies between nuclei, and R2* relaxometry are needed to capture relevant properties of the signal [37].

One of the most fundamental sequences featured in MRI is the gradient echo (GRE) which involves two rudimentary steps. First, an external dephasing gradient is applied in the frequency encoding step to squelch the FID by slightly altering the resonance frequencies of the sample [38]. After this, a rephasing gradient is implemented with the same magnitude as the before gradient, but in an opposite polarity [38]. This allows the FID to reform as a gradient echo that retains both the T2 and T2* information of the signal, hence GRE sequences can be used to assess pathologies that induce severe field inhomogeneities such as iron overload [30,39]. Additionally, a multi-echo gradient echo (mGRE) sequence shown in Figure 3 will allow for more echoes to be produced after the initial one through repeated applications of the rephasing and dephasing gradients, thus it can be utilized in chemical shift imaging in which multiple TEs are needed to measure “in-phase” and “out-of-phase” fat-water signals [40]. However, GRE sequences do encounter a few problems. Because the T2* information is retained, signal loss is much more rapid with GRE sequences compared to other sequence types such as spin-echo [39]. Also, because GRE sequences utilize Cartesian sampling methods, motion artifacts such as

breathing may become an issue in abdominal and pediatric imaging [41]. Hence, alternative sequences have been explored to better assess diseases such as iron overload and steatosis [35,42].

While GRE sequences are the traditional method of evaluating iron overload, ultrashort echo time (UTE) sequences have shown promising results in quantifying extreme concentrations of iron that GRE sequences inadequately assessed [35,42]. The structure of a UTE sequence optimizes the shortest possible delays between signal excitation and acquisition by utilizing TEs of ≤ 0.1ms [35]. Compared to the shortest possible TE of GRE, 1.0ms, a tenfold difference in TE allows UTE to sample the signal much earlier and can measure very short-lived signals such as those produced under high iron conditions [35]. This is accomplished by a few factors. First, UTE sequences utilize radial sampling of k-space which allows for simultaneous phase and frequency encoding gradients to reduce scan time while also reducing motion artifacts that might be seen in abdominal imaging [35,43]. As seen on Figure 3, UTE sequences also use "Half RF" pulses, but this requires two acquisitions with inverted slice selection gradients to obtain the entirety of the signal information [35,43]. By utilizing these parameters in tandem, the shortest possible TEs of ~0.1-0.02 ms are obtained in UTE sequences [35,43]. UTE sequences do have a few drawbacks, however. The utilization of half-pulse excitation makes the sequence sensitive to confounding out-of-slice signals due to eddy currents or gradient delays, all which may impede quantification of signal biomarkers [35]. Additionally, UTE sequences have only been validated in magnitude-based data, so quantification methods that utilize complex-based biomarkers require additional verification against biopsy data [42,44].

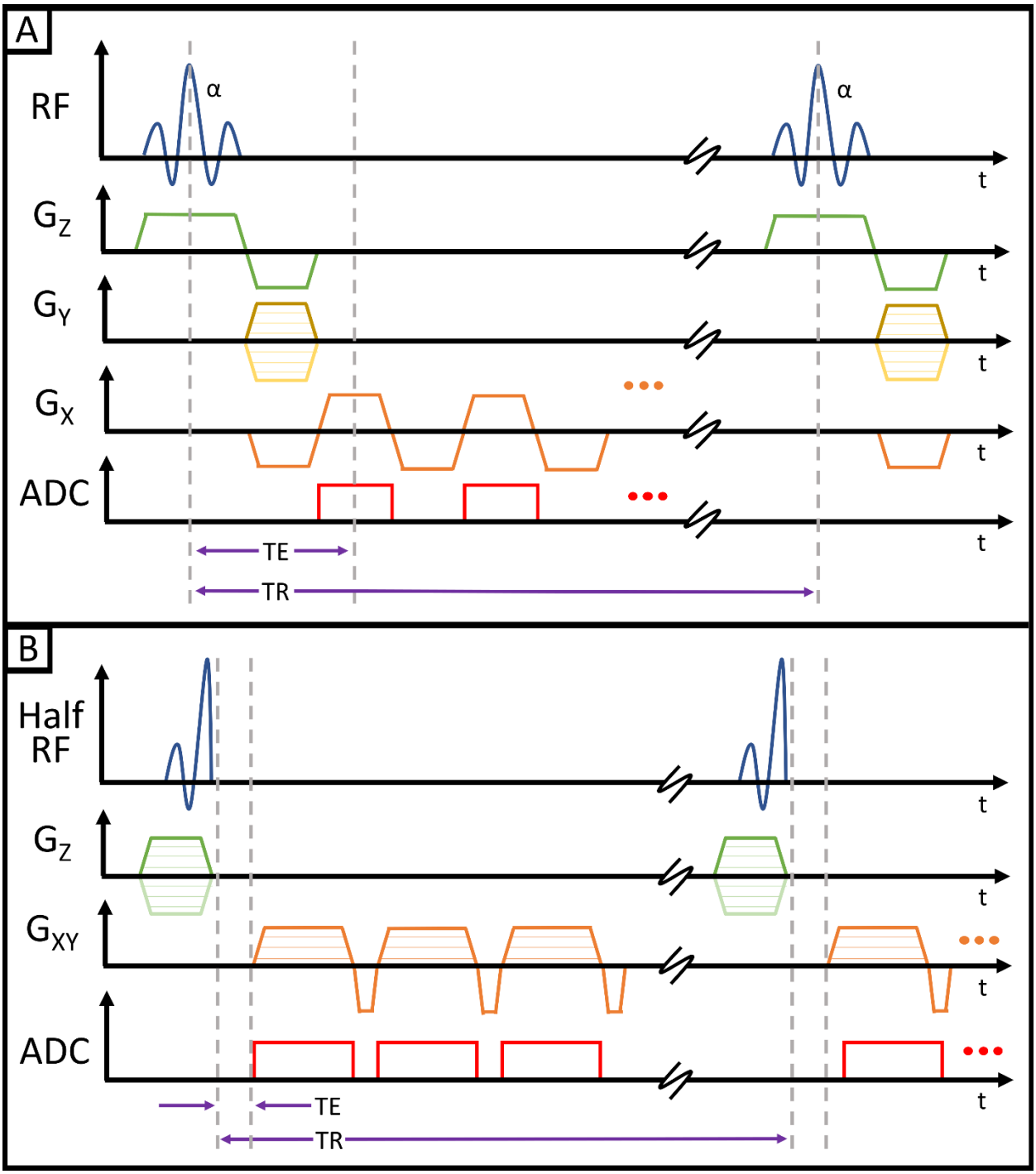

Figure 3. Pulse sequence diagrams of GRE and UTE sequences. (A) A mGRE (multi-echo gradient echo) sequence is shown with separate slice selection (G_z), phase encoding (G_y), and frequency encoding (G_x) gradients, and signal acquisition occurs during the rephasing gradient of the frequency encoding step. (B) A UTE (ultra-short echo time) sequence is shown with a half RF pulse along with an independent slice selection gradient (G_z) and combined phase and frequency encoding gradients (G_{xy}). The acquisition occurs only during the positive G_{xy} to prevent phase encoding errors.

Chapter III

Quantitative MRI of Diffuse Liver Diseases: Techniques and Tissue-Mimicking Phantoms

Introduction

Magnetic resonance imaging (MRI) has evolved as a noninvasive alternative to biopsy for the assessment of diffuse liver diseases, primarily hepatic iron overload, steatosis, and fibrosis [17,18,45]. Hepatic iron overload is a manifestation of hereditary hemochromatosis and transfusional hemosiderosis and is also common in some chronic hepatopathies [46]. Likewise, hepatic steatosis is the abnormal accumulation of fat in the liver and is a hallmark feature of non-alcoholic fatty liver disease (NAFLD), the most common diffuse liver disease that currently affects about 20%-30% of the U.S. population [47]. The co-occurrence of hepatic fat and iron overload, referred to as combined storage disease, is also being increasingly recognized [10,11,48]. Hepatic fibrosis is another common outcome of various liver pathologies, including hepatitis, NAFLD, and iron overload, and has a high prevalence of up to 25% in the general population [2,49,50]. The coexistence of fat, iron overload, and/or fibrosis with any pre-existing liver disease can accelerate disease progression. As early stages of these diseases are reversible conditions, techniques that can provide early diagnosis, allow disease monitoring, and guide therapeutic intervention are crucial for better prognosis.

Over the last two decades, several technical developments in quantitative MRI techniques have emerged that enable more precise and frequent monitoring of these diffuse liver pathologies to guide treatment and prevent disease progression and long-term complications. For testing, validating, and standardizing quantitative MRI methods across sites, vendors, and field strengths, phantoms are used as stand-ins to human tissue to mimic various liver pathologies. Quantitative

liver phantoms also play an essential role for quality assurance in multi-center clinical trials and drug discovery studies that rely on quantitative imaging biomarkers as primary endpoints [51-53]. Organizations such as Radiological Society of North America (RSNA) Quantitative Imaging Biomarkers Alliance (QIBA) have laid out guidelines in bringing quantitative liver imaging to the clinical sector by collaborating with researchers and healthcare professionals to perform multi-site and multi-vendor validation studies on some promising MR biomarkers using phantoms [54-57]. However, currently, there is no standardization in the preparation of MRI phantoms for emulating diffuse liver diseases, as different studies utilize various types and sizes of iron and fat particles to mimic iron overload and steatosis respectively, different materials for mimicking fibrosis, and different matrices like water, agarose, or gels [58-64]. Further, with MRI, the co-occurrence of liver iron, fat, and fibrosis can confound or interfere with the quantification of each other. To address these challenges, novel MRI acquisition methods and multi-spectral signal models are being developed for accurate and simultaneous assessment of these diffuse liver diseases [44,65-67]. In addition, recent attempts include creating combination phantoms to mimic coexisting liver pathologies of iron overload, steatosis, and fibrosis observed in vivo for validation and quality assurance of MRI techniques for quantification of diffuse liver diseases [68]. However, simply combining different materials for each pathology to create phantoms mimicking concurrent diffuse liver diseases do not mimic the MRI signal characteristics seen in tissues [68].

The purpose of this study is, therefore, to provide a comprehensive review of the published MRI phantom studies on diffuse liver pathologies of iron overload, steatosis, and fibrosis by first describing the disease morphology and discussing the MRI techniques and biomarkers for each pathology and then examining the phantom materials chosen for mimicking these diffuse liver diseases. In this study, a systematic review is performed using PubMed as the primary database to

identify and extract information from publications that constructed MR liver phantoms for mimicking iron overload, steatosis, fibrosis, and the combination of these pathologies. The key words used to search for these publications are phantom, liver, iron overload, steatosis, fibrosis, and MRI.

The following sections describe the desired characteristics and matrix materials of liver phantoms and briefly cover the in vivo morphology and quantitative MRI techniques for each pathology, followed by reviewing the phantom materials used to emulate each disease as well as elucidating their benefits and limitations.

Liver Phantoms

The design requirements of any quantitative tissue-mimicking MRI phantom are typically: (1) characteristic MRI signal behavior and relaxation times that accurately emulate biomarkers of disease while considering field strength dependencies, (2) cover relevant clinical ranges of the disease, (3) multi-site, multi-vendor, and multi-platform reproducibility for standardization, (4) stability over long periods of time, and (5) ease of fabrication and handling [58,69-72]. These tissue-mimicking phantoms can be constructed using a variety of materials to achieve these characteristics. However, phantoms emulating diffuse liver diseases have particular requirements that may limit the materials chosen, and these specifications are described below in the appropriate phantom material sections. Nevertheless, it must be understood that tissue-mimicking phantoms cannot simulate every facet of a tissue, but the phantoms must mimic the MRI signal characteristics observed in vivo of these diffuse liver pathologies.

Matrix Materials

Matrix mediums are a necessary requirement in phantoms for stabilizing the contents used to mimic liver pathologies. The most widely used matrix mediums for making phantoms are water,

agar, and agarose. Water is risk-free and easy to handle, but it has some disadvantages as a phantom medium. Water requires a 10-minute settling time to allow suspensions to stabilize and is more susceptible to vibrational effects that may cause motion artifacts [58]. Additionally, water has similar T1 and T2 relaxation times, and therefore, it does not mimic the behavior of human liver tissues in which T1 is much longer than T2 [73-75]. Alternatively, materials such as agarose, carrageenan, polyvinyl alcohol (PVA), polyacrylamide (PAA), and gelatin create a jelly-like medium that will hold the phantom contents in suspension, thereby reducing boundary artifacts and avoiding flow issues [58,76]. Both agarose and agar gel have T2 relaxation times that are similar to human tissue (~30-200 ms) depending on the chosen concentration [58,77]. However, the T1 relaxation times are not comparable to human tissues (~300-1500 ms) but can be adjusted with paramagnetic additives such as $CuSO_4$, $NiCl_2$, $MnCl_2$, or $GdCl_3$ to reduce T1 [58,77]. An alternative polysaccharide that is utilized in MRI phantoms is carrageenan gel, a more flexible and resistant substance that can be molded into unique shapes, but use of high concentrations can cause the T2 relaxation times to be longer than human tissues [76,78]. Like many polysaccharides, agar and agarose need thermal treatments (80-100°C) during the preparation process, so caution must be taken when using some phantom contents that have restricted temperature ranges [58]. Conversely, PVA-based phantoms benefit from greater longevity and structural stability than most matrix materials, but the need for freezing and thawing cycles to prepare the phantom may pose similar issues [76,78].

While there is no standard guideline to define an acceptable shelf life of a phantom, the phantom stability is greatly affected by the matrix material chosen. Some materials such as agarose and silicone are known to be mechanically stable over long periods of time, assuming no extreme fluctuations in temperature and humidity in storage, while other materials such as PAA are only

stable for a few months. [76]. Further, gel phantoms are prone to microbial growth and often use sodium azide or sodium benzoate as preservatives to retard mold formation and increase shelf life [58,61,68,79]. To mimic native tissues, some studies also used homogenized animal liver tissues as a matrix medium instead; however, special handling and storage of these tissue phantoms may be a concern [18,80,81].

Iron Overload

Pathophysiology & Morphology

Hepatic iron overload is a histological hallmark of primary (hereditary) or secondary hemochromatosis [7,82]. Hereditary hemochromatosis is caused by a defect in the genes that control intestinal iron absorption from food, primarily the HFE gene, and affected patients absorb iron at 5–10 times the normal rate (up to 10mg/day) [46,83]. Secondary hemochromatosis is usually the result of another disease or condition that causes iron overload, e.g., severe chronic hemolysis requiring chronic blood transfusions. Because the body has no physiologic mechanism for clearing excess iron, the extra iron accumulates in organs, primarily the liver, leading to hepatic iron overload. As the liver is a central organ in regulating iron homeostasis, iron is also one of the most common parenchymal deposits in other diffuse liver diseases like NAFLD apart from hemochromatosis [84]. The degree of liver dysfunction is directly dependent on the amount of hepatic iron deposition and progressive iron accumulation eventually leads to hepatomegaly, fibrosis, and finally, cirrhosis and liver failure [85-89].

The liver stores excess iron in hepatocytes and reticuloendothelial Kupffer cells, as ferritin and hemosiderin molecules. Ferritin is the principal iron storage molecule found in cells and is readily available to meet physiologic needs. Ferritin molecules in clusters have a size of 50-70 nm and are not visible individually on Perls iron stain, however, they can be seen as a diffuse blue

blush in the cytoplasm of hepatocytes on light microscopy [90-92]. If ferritin levels are persistently elevated, hemosiderin deposits can develop as conglomerates of clumped ferritin particles. Hemosiderin appears as granular, golden brown cytoplasmic deposits on hematoxylin and eosin (H&E) stain and as blue deposits on Perls iron stain as shown in Figure 1. During iron overload, aggregates of hemosiderin molecules are deposited in body tissues and range in size from 0.1 to 2 μm, eventually causing tissue damage and dysregulation of function [93]. Further, with an increase in iron overload severity, iron is deposited as clusters, and the deposition among hepatocytes are not uniform [93].

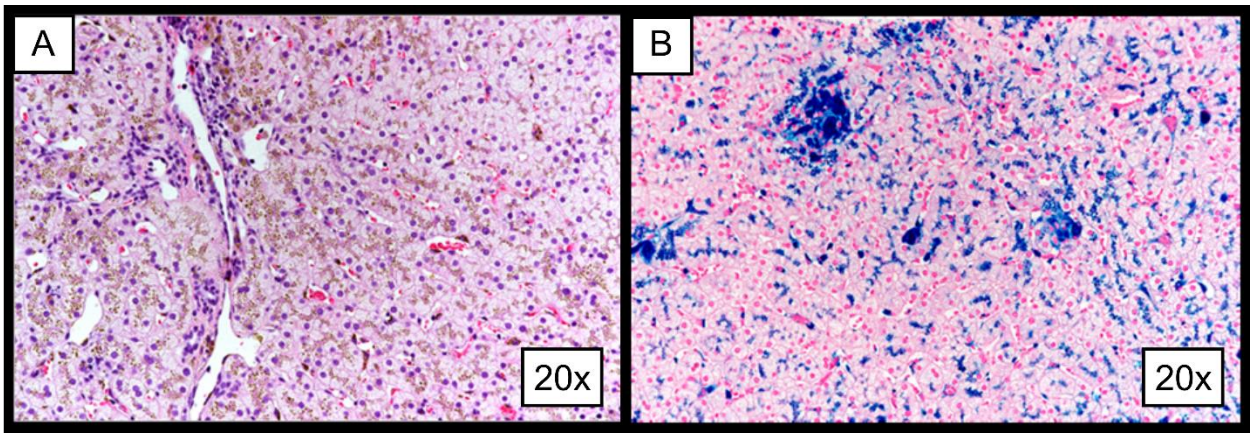

Figure 4. Hemosiderin deposits shown in the liver biopsy samples using hematoxylin & eosin (H&E) stain (A) and Perls Prussian blue iron stain (B) at 20x in a severely iron overloaded patient with biopsy hepatic iron content of 16.5 mg Fe/g. Iron deposits are seen as brown granules in the cytoplasm of the Kupffer cells and hepatocytes on the H&E stain and as blue pigment on Perls iron stain.

The amount of iron in the liver, or hepatic iron content (HIC), is a necessary metric for detecting and staging iron overload as HIC significantly correlates with total body iron stores [94]. The current gold standard to quantify HIC directly is by atomic absorption spectrophotometry on liver biopsy specimens, which measures HIC in milligram of iron per gram of dry liver tissue weight (mg Fe/g dry tissue wt.) [95]. Alternatively, iron deposition in biopsy specimens can also

be evaluated histologically on a semi-quantitative 5-point grading scale based on Prussian Blue staining of iron granules [46].

Quantitative MR Techniques

R2/R2 Relaxometry*

Currently, MRI techniques based on transverse relaxometry (R2/R2*) are considered robust and clinically accepted methods for non-invasively assessing HIC [96]. Iron in the form of ferritin and hemosiderin has paramagnetic properties, causing faster signal decay and increasing the R2 and R2* relaxation rates. R2 can be measured using a series of single spin-echoes, each acquired after a separate excitation [97] or with a train of spin-echoes acquired after a single excitation using a Carr-Purcell-Meiboom-Gill sequence [98-100]. St. Pierre et al. developed a R2-HIC calibration method that is commercially available as FerriScan (Resonance Health, Ltd, Claremont, Australia) for HIC determination [97]. The R2-HIC relationship is however curvilinear which saturates at high HIC, hence making the method less sensitive to severe iron overload.

On the other hand, R2* is measured using a multi-echo gradient-echo (GRE) sequence and fitting a mono-exponential signal model [2,101,102]. The R2*-HIC relationship is linear for the entire pathophysiological range of HIC making R2* measurements desirable for clinical assessments [103,104]. However, for extreme cases of iron overload (HIC > 30 mg Fe/g dry tissue wt. at 1.5T or HIC > 15 mg Fe/g at 3T), the R2* quantification with GRE sequences is limited by the shortest possible echo time (TE) of about 1 ms. To overcome this issue, ultrashort echo-time (UTE) techniques have been developed to improve the dynamic range of R2* relaxometry and have demonstrated high R2* accuracy even for severe iron overload [35,42,105]. One major limitation with R2* techniques is that the presence of fat (steatosis) introduces oscillations in the signal decay and confounds R2* measurements. To overcome this, multi-spectral signal modeling

techniques have been proposed for accounting for both the spectral complexity of fat and R2* decay. These techniques are discussed in more detail in the MR Techniques section under steatosis below.

Quantitative Susceptibility Mapping

Although relaxometry based methods are robust, they are confounded by other pathologies such as fibrosis, thus causing bias in HIC estimations [106,107]. Alternatively, quantitative susceptibility mapping (QSM) techniques can be used to estimate HIC by quantifying magnetic susceptibility, an intrinsic tissue property that is highly sensitive and linearly related to iron content, and is not affected by cellularity changes such as fibrosis [108]. Iron in the form of ferritin and hemosiderin induces a local susceptibility and affects the measured phase on GRE images. The local field map is then extracted from the phase data, and the susceptibility map is generated from the local field map by using a dipole inversion algorithm [109-112]. In contrast to the brain, QSM estimation in the abdomen must account for signals from multiple species (i.e., fat and water) and quantify a relatively wider range of iron contents (5-10 times greater iron deposition in liver iron overload than in brain). Recent studies have incorporated multi-spectral fat-water models to produce a fat-corrected field map estimation and used that in conjunction with QSM processing to generate susceptibility maps and have demonstrated a linear correlation between HIC and susceptibility values [113-117]. However, QSM is still limited to research due to both a lack of standardization of the technique and a not well-established relationship between susceptibility values and HIC [17]. Hence, it is not yet commercially available on MRI scanners for clinical HIC diagnosis [17].

Iron Overload Phantoms

The desired properties of an iron overload phantom are to maintain the characteristic relationship between MRI biomarkers (R2/R2*, susceptibility) and iron concentration, match the clinical ranges of MRI biomarkers in conditions of hepatic iron overload (R2*: ~40–1000 s^{-1} at 1.5T, susceptibility: ~0.2–6 ppm) [113,115-118] and preserve the size and distribution of iron particles seen in liver tissues throughout the phantom. MRI studies that constructed phantoms to emulate hepatic iron overload using a variety of paramagnetic materials are summarized in Table 1. Of the studies reviewed, the most common materials used for making phantoms mimicking iron overload are iron nanoparticles. Iron oxide nanoparticles exhibit varying levels of paramagnetic and superparamagnetic behavior depending on the oxidation state of iron (ferrous vs. ferric) and particle size, in turn altering the R2* relaxation [119,120]. Ferrous iron, such as that of iron sulfate, can be added to emulate the R2* range [51-434 s^{-1}] of iron content in clinical hepatic iron overload [121]. On the other hand, ferric iron molecules exhibit stronger paramagnetic behavior and have greater susceptibility than ferrous iron [120]. A recent study by Alústiza et al. compared iron oxide nanoparticles with different oxidation states and found that the decrease in MRI signal for ferric iron ($FeCl_3$) was more linearly correlated with the increase in iron concentration than compared to ferrous iron ($(NH_4)_2Fe(SO_4)_2$), therefore more closely emulating the linear relationship between R2* and iron content observed in hepatic iron overload [64].

Table 1. MRI iron phantom studies listing phantom materials used, MR techniques, and R2*/QSM ranges.

Citation PMID	**Phantom Materials**	**MR Technique (Field Strength)**	**R2*(s^{-1})/QSM (ppm) Range**
St. Pierre et al. 2005 15256427 [97]	$MnCl_2$ (0.1-3.2 mM) Matrix: Water	Multi-echo SE	10-280 s^{-1} (R2)
Szurowska et al. 2010 20105330 [80]	$FeCl_3$ Matrix: Pork liver	GRE SIR (1.5T)	n/a
Chandarana et al. 2012 22997371 [122]	Ferumoxytol (Feraheme®, 1/2000-1/500) Matrix: Deionized Water	Multi-echo GRE (1.5T)	25-150 s^{-1}
Tsai et al. 2014 25120622 [123]	$Fe(OH)_3$ (0.1-25 mg/mL) Matrix: Pork liver	Multi-echo GRE (1.5T)	80-400 s^{-1}
Alústiza et al. 2015 25874207 [64]	$FeCl_3$ (0.05-4 mg Fe/mL) Matrix: Water	GRE SIR (1.5T)	n/a
Yokoo et. al 2015 25996989 [124]	$MnCl_2$ (0-25 mM) Matrix: Water	3D GRE (1.5T)	~1-1250 s^{-1}
Krafft et al. 2016 26308155 [59]	1) BNF (0.4-220 µg/mL), 2) DSPIO (0.2-125 µg/mL) 3) $MnCl_2$ (0-3.2 mM) Matrix: Agarose	Multi-echo GRE, FS GRE (1.5T, 3.0T)	1) 20-2700 s^{-1} 2) 20-600 s^{-1} 3) 3-250 s^{-1}
Ibrahim et al. 2016 26861202 [121]	$FeSO_4$ (0.5-4.5g) Matrix: Agarose	Multi-echo GRE (3.0T)	~51-435 s^{-1}
Guimaraes et al. 2016 27190762 [125]	MION 48 (1:50 - 1:10000 of 1 mg Fe/mL) Matrix: Saline	FS TSE, FS CPMG (1.5T)	n/a
Brown et al. 2017 27435747 [126]	USPIO (Resovist®, 0–246.48 µg/mL) Matrix: CAG gel	Multi-echo GRE (3.0T)	22–2829 s^{-1}
Krafft et al. 2017 28090666 [35]	BNF (0.4-220 µg/mL) Matrix - 2% Agar	Multi-echo UTE (1.5T, 3.0T)	20–2640 s^{-1}
Hong et al. 2017 27495266 [60]	Ferumoxides (Feridex®, 2-45 mM) Matrix: 0.9% Agarose	Multi-echo 2D-UTE, 2D IR-UTE, 3D UTE, 3D IR-UTE (3.0T)	~0.1-12 ms^{-1}
Lu et al. 2018 29314215 [127]	1) Gadopentetate Dimeglumine (Magnevist®,1.5-9 mg/mL) 2) Ferumoxides (Feridex®, 2-22mM) Matrix: 0.9% Agarose	Multi-echo 3D UTE (3.0T)	1) ~0.2-2.8 ppm 2) ~0.4-4.5 ms^{-1} ~0-52 ppm

Tipirneni-Sajja et al. 2019 30358001 [42]	BNF (0.5-220 µg/mL) Matrix - 2% Agar	Multi-echo UTE (1.5T)	~ 20-2500 s^{-1}
Headley et al. 2020 33207043 [128]	$FeCl_3$ (29.4-96.4 mg) Matrix: Water	Multi-echo GRE (1.5T, 3.0T)	103-420 s^{-1} (1.5T) 144-616 s^{-1} (3.0T)

Abbreviations: BNF, Bionized NanoFerrite; CAG, carrageenan-strengthened agarose/gadolinium gel; DSPIO, dextran-coated superparamagnetic iron oxide nanoparticles; CPMG: Carr-Purcell-Meiboom-Gill; $FeCl_3$, Iron(III) chloride; $Fe(OH)_3$, Iron (III)-hydroxide; $FeSO_4$, Iron sulphate; FS, fat suppression; GRE, gradient recalled echo; $MnCl_2$, Manganese chloride; MION 48, dextran-coated magnetic iron oxide nanoparticles; SE, spin echo; SIR, signal intensity ratio; TSE: turbo spin echo; USPIO, ultra-small particles of iron oxide; UTE, ultrashort echo time; IR-UTE: adiabatic inversion recovery prepared UTE.

Another component that impacts the efficacy of iron oxide nanoparticles is the organic coating over the iron core, impacting aqueous stability, conjugation potential, and reducing agglomeration and allowing uniform dispersion of iron particles in the medium [129,130]. For example, pure magnetite powder without a coat forms heterogenous clumps in phantoms [79]. Dextran is one of the most popular coatings used for iron nanoparticles as it is water-soluble and biodegradable [130]. BNF (Bionized NanoFerrite) particles are one example of dextran-coated iron nanoparticles and have been reported to produce a wide span of R2* values (20-2700 s^{-1}), thus covering the entire clinical range of R2* at 1.5T and 3T during iron overload [59]. Figure 5 shows representative MRI iron phantoms made using BNF particles in 2% agar, their corresponding R2* maps obtained using mono-exponential model and the excellent linear correlation obtained between R2* values and iron concentrations in these phantoms.

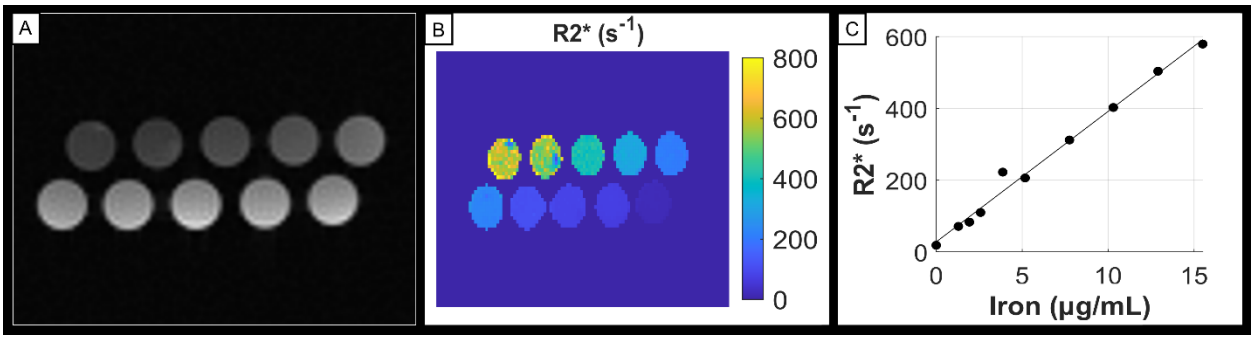

Figure 5. Representative MRI iron phantoms mimicking liver iron overload. (A) MRI magnitude images of iron phantoms consisting of BNF iron nanoparticles of size 80 nm in 2% agar, (B) R2* maps calculated by fitting a mono-exponential model [2], and (C) linear regression plot of R2* (s^{-1}) vs iron concentrations (%) demonstrating an excellent linear correlation with $R^2 = 0.9945$.

Alternatively, SPIO (superparamagnetic iron oxide) nanoparticles, which have emerged as specialized MRI contrast agents, can also be used for mimicking iron overload. The dextran-coated SPIO contrast agent, ferumoxides (Feridex®), is a common choice of iron material used in phantoms, yielding R2* and susceptibility values as high as 100-12000 s^{-1} and 52 ppm respectively at 3.0T [60,61,127,131]. Some previous studies also used the carboxydextran-coated SPIO contrast agent, ferucarbotran (Resovist®), for mimicking iron overload with R2* values of 22-2829 s^{-1} at 3.0T [126,132]. Alternatively, ferumoxytol (Feraheme®) can also be used for making iron overload mimicking phantoms by diluting with deionized water, with a reported R2* range of 25 – 150 s^{-1}; however, the R2* range can be increased with smaller dilutions [122].

Certain non-iron contrast agents such as extracellular gadolinium chelates (e.g., gadopentetate dimeglumine (Magnevist®)) and manganese-based contrast agents (e.g., manganese chloride) that are used clinically, also have magnetic properties comparable to those of iron, thereby providing a similar linear relationship between contrast concentration and R2*/susceptibility for mimicking iron overload [127,133,134,124]. Both gadolinium and manganese are water soluble, allowing them to be suspended in solution [133]. However,

compared to manganese-based contrast agents (1-1250 s^{-1}), gadolinium has been reported to provide higher R2* values at 1.5T (up to 3000 s^{-1}) [59,124,135].

One problem with the use of most iron particles is that they are produced on the scale of nanometers. However, in cases of iron overload, accumulated hemosiderin particles are on the scale of micrometers (0.1 – 2 μm [93]), a much larger size than iron particles available in commercial products. To mimic in vivo sizes of iron particles, Mobini et al. used insoluble magnetite powder with a mean diameter of 1.17 μm [0.5 – 5 μm] in their phantom design to emulate pathological conditions of liver iron overload [79]. However, the inhomogeneous suspension of magnetite resulted in microscopic iron clustering that altered relaxation times, hence leading to overestimated R2* at only mild iron contents [79]. In a recent study, Zhao et al. incorporated soluble iron microspheres with a diameter of 2.9 ± 0.14 μm, to mimic in vivo hemosiderin particles, and constructed phantoms that produced target R2* values of 100 – 500 s^{-1} at 1.5T and 3T, which however did not cover the entire clinical spectrum of R2* ranges [68].

MRI phantoms mimicking iron overload are also available ready-made to be purchased from commercial vendors. Calimetrix provides twelve R2* phantoms in the range of 15-1000 s^{-1} (R2* phantom, Model 300). These phantoms are designed to match clinical hemochromatosis and other iron overload conditions and specifically for testing and quality control of MR-based R2* quantification. CaliberMRI is another commercial vendor that provides a T2 phantom (ISMRM/NIST System Phantom, Model 130) utilizing $MnCl_2$ with T2 ranges of 5-550 ms (~2-200 s^{-1} R2 measured at 3T).

Steatosis

Pathophysiology & Morphology

Hepatic steatosis, or fatty liver disease, is the abnormal accumulation of lipids within the cytoplasm of hepatocytes, predominantly in the form of triglycerides. Approximately, 25% of the world population is affected by steatosis [136] and this number is projected to increase further with the increasing epidemics of obesity, diabetes, and metabolic syndrome [137,138]. The liver plays a critical role in lipid metabolism and any disturbances in these metabolic processes can lead to hepatic steatosis, which is a hallmark of many diffuse liver diseases including viral hepatitis and alcoholic and nonalcoholic fatty liver disease [10]. NAFLD can progress to non-alcoholic steatohepatitis (NASH), which is characterized by inflammation, cellular degeneration, and fibrosis and can ultimately lead to cirrhosis [139]. Cirrhosis associated with NASH is estimated to be the leading etiology of liver transplantation in the coming decades [140].

Steatosis can be characterized into two major types: microvesicular and macrovesicular steatosis, depending on the relative size of lipid vacuoles and the displacement of nucleus seen on histology. Macrovesicular steatosis is the predominant form seen in diffuse liver diseases with fat droplet sizes ranging from >1 μm to the order of the sizes of hepatocytes (20-25 μm) [141,142]. Steatosis is typically graded semi-quantitatively on histology based on the visually estimated percentage of hepatocytes infiltrated with fat deposits – less than 5% (normal), 5% to 33% (mild), 34% to 66% (moderate) and greater than 66% (severe) as shown in Figure 6 [143]. However, the clinical histological grading estimates only the percentage of affected hepatocytes but does not reflect the absolute fat percentage in the liver.

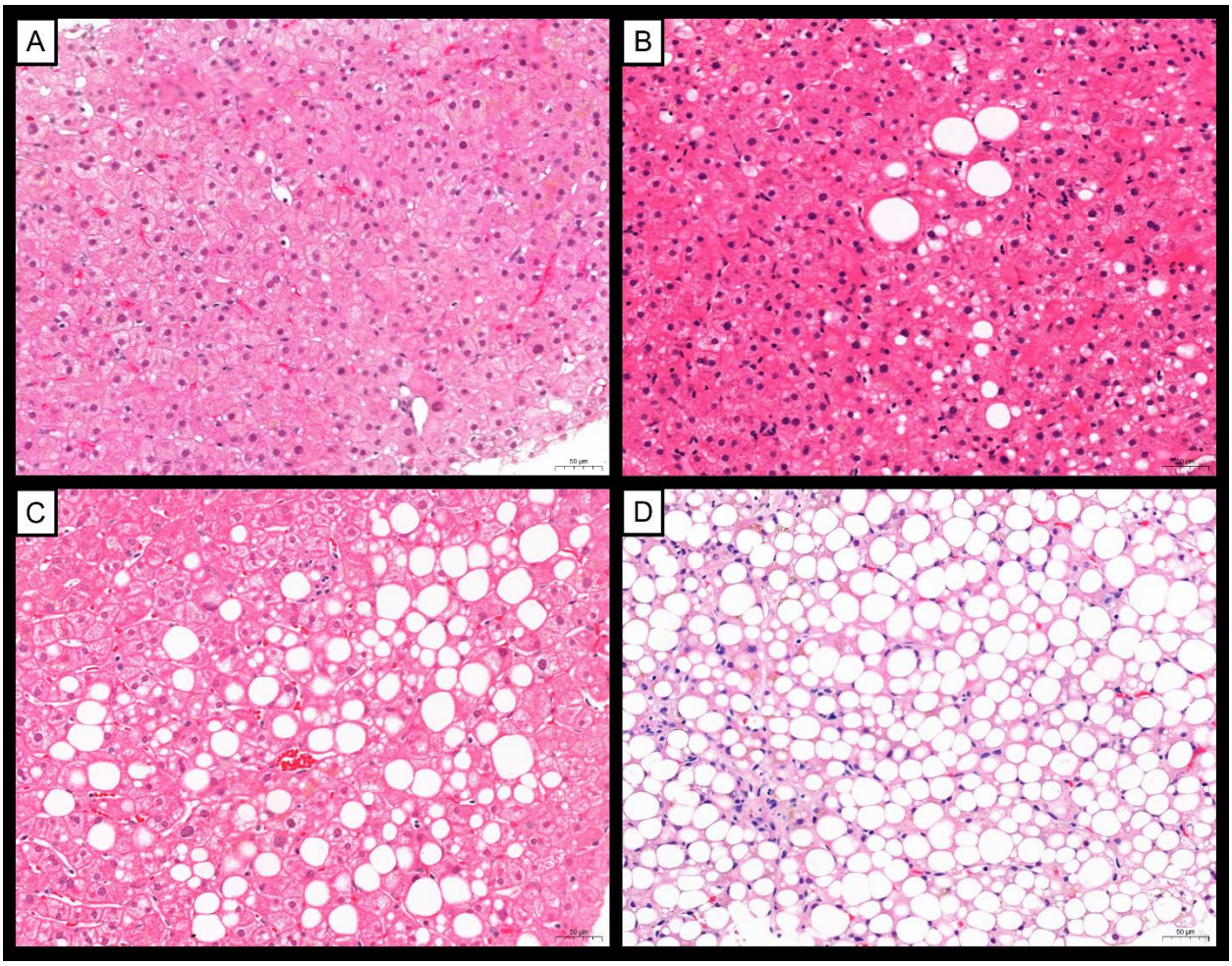

Figure 6. Histology images at 200x of liver biopsy samples stained with hematoxylin and eosin showing the fat droplet morphology and deposition in patients with macrovesicular steatosis. The steatosis grades of these liver biopsy samples based on the NASH CRN scoring system are (A) grade 0 (normal), (B) grade 1 (mild), (C) grade 2 (moderate) and (D) grade 3 (severe).

Quantitative MR Techniques

Magnetic Resonance Spectroscopy

Magnetic resonance spectroscopy (MRS) has been used as a noninvasive alternative to biopsy and is regarded as the most accurate technique to quantify fat [144,145]. MRS is based on the physical principal that MR-active hydrogen protons in specific molecules resonate at a unique Larmor frequency depending on the molecular structure of compounds. For example, fat and water molecules resonate at slightly different frequencies with a frequency difference of 3.4 ppm (224

Hz at 1.5T and 448 Hz at 3T) between the water (-OH) and main lipid peak (methylene, -CH_2) in liver in vivo [146,147]. Based on the priori known chemical shifts, water and fat peaks can be detected using MRS, and their proton densities (proportional to peak amplitudes) can be quantified to estimate fat fraction (FF) [148-150]. However, due to the small sampling volume (~0.2 - 2 cm^3 [151]) and the requirement of offline analysis by an experienced user, MRS has limited use for clinical purposes [145]. Alternatively, over the last two decades, chemical shift-based MRI techniques have been developed that provide 2D cross-sectional images or 3D whole liver coverage.

Chemical Shift Based Fat-Water Imaging

Chemical shift-based fat-water imaging is based on the same physical principle as MRS. Due to the difference in the resonance frequencies, fat protons precess at a slower frequency than water protons and develop a phase lag over time compared to that of water protons. For example, the main lipid peak (methylene, -CH_2) and water (hydroxyl, -OH) protons are in-phase at 4.6 ms and out-of-phase at 2.3 ms at 1.5T. The most common chemical shift-based fat-water separation method is 2-point Dixon imaging, which collects images when fat and water signals are in-phase and out-of-phase, and thereby generates fat-only and water-only images from which FF is computed [152,153]. Although 2-point Dixon is a useful technique to assess steatosis [154-157], this method is affected by magnetic field inhomogeneities and T1 bias [158-160], and most importantly, this technique does not consider R2* decay and the spectral complexity of fat which can corrupt FF estimates [158,161]. T1 bias causes overestimation of FF and can be minimized by reducing the flip angle, correcting using variable flip angles, or in post processing [44,162,163]. However, post processing corrections are generally based upon the assumed T1 values of fat and water in the liver, so in vivo pathologies such as iron overload and fibrosis or phantoms that deviate

from these T1 values can produce inaccurate FF results [162,163]. As the signal is collected over multiple echo times during which R2* decay occurs, not accounting for the signal decay can lead to underestimation of FF, especially in tissues with short T2* such as those containing excess iron [152]. Various Dixon techniques have been developed over the years that differ in the number of echoes (or points) that are sampled [164]. While traditional 2-point and 3-point Dixon methods are desirable for a shorter scan time, they typically provide only qualitative information about fat content [164]. On the other hand, using six or more echoes increases the scan time, but they allow for accurate modeling and provide quantitative FF results when fitted with multispectral fat-water R2* models described below. [164-166]. These chemical shift-based MRI techniques are well validated against MRS, showing an excellent agreement between MRS and MRI FF values [167-169]. Further, previous studies demonstrated that clinical MRI FF values can range up to ~50% in patients and showed a good correlation to severity of steatosis graded on histology [170-172].

Multi-spectral Fat-Water Models with R2 Correction*

Over the last decade, several multi-spectral signal modeling techniques have been proposed for accounting for the spectral complexity of fat and R2* decay. These techniques use multi-echo GRE acquisitions and perform multi-spectral fitting for simultaneous quantification of R2* and FF and thus, can enable the diagnosis of both hepatic iron overload and steatosis. One popular technique is based on nonlinear least squares (NLSQ) fitting of the fat–water signal model either using magnitude or complex data [67]. These models require priori information about relative frequencies and amplitudes of the multiple lipid peaks. Further, most NLSQ models assume a common R2* rate for fat and water for reducing model complexity [67], known as the single R2* model. However, this assumption will be incorrect if the R2* of fat and water are different, especially in cases of iron overload [173]. A dual R2* model has been developed and

was shown to improve the FF quantification accuracy as compared to the single R2* model in phantoms [173]. However, the dual R2* model can be unstable and complex due to the estimation of an additional parameter, and the single R2* model has been described to be more accurate in low SNR conditions for FF estimation [174]. Additionally, recent studies have reported that multipeak fat modeling with complex fitting and single R2* correction model performs better over a range of clinically relevant FF values [174,175].

Another multi-spectral signal modeling technique is based on autoregressive moving averaging (ARMA) that does not use any prior information of fat spectrum and determines FF and separate R2* values for water and lipid species [44,176,177]. A recent study demonstrated that both NLSQ and ARMA models accurately quantified R2* and FF values, but ARMA yielded inaccurate values at both high iron and fat conditions, whereas NLSQ overestimated R2* and FF values at high iron and no fat conditions; both models potentially failing due to rapid T2* decay at high iron overload conditions [44].

Steatosis Phantoms

The design considerations for steatosis phantoms are to emulate the MRI characteristic multi-peak fat spectra seen in adipose tissue, match clinical ranges of hepatic steatosis (~0-50% FF), and maintain the size and distribution of fat deposits seen in liver tissues homogeneously throughout the phantom. Table 2 details the lipid substitutes, FF ranges, and MR techniques used in steatosis phantom studies.

Peanut oil is the most common material used in fat phantom studies due to its availability, ease of preparation, and similar NMR spectrum as triglycerides in adipose tissue [51-53,178-180]. Other types of vegetable oils, such as canola or soybean, have also produced similar FF results to peanut oil despite slight differences in saturated and unsaturated fat content [81,150,181-185].

Animal products such as lard and pork fat are also used as lipid substitutes and are mixed with appropriate proportions of liver tissue to create a homogenate or heated until in a liquid form for making steatosis phantoms [18,186]. As seen on Table 2, mayonnaise is another animal product used in steatosis phantoms and has been shown to display similar MRI signal behavior as other lipid substitutes when used in combination phantoms [117]. Hybrid plant and animal products can also be used to create steatosis phantoms through mixing vegetable oils and liver tissues [81]. Further, clinical fat emulsion supplements such as Intralipid® and Microlipid™ can also be used for constructing steatosis phantoms [150,187]. Alternatively, commercial steatosis phantoms are available from Calimetrix (Fat Fraction Phantom, Model 300) covering FF ranges from 0-50% and 100% [54].

Table 2. MRI fat phantom studies listing the phantom materials used, MR techniques, and fat fraction ranges.

Citation PMID	**Phantom Materials**	**MR Technique (Field Strength)**	**FF (%) Range**
Chang et al. 2006 16794122 [81]	Canola Oil Matrix: Calf liver	2-echo GRE, MRS (1.5T)	0-80%
Bernard et al. 2008 18064714 [181]	Soya oil Matrix: Carageenan	2-echo Dixon, chemical shift imaging, MRS (3.0T)	0-100%
Hamilton et al. 2011 21834002 [150]	Safflower oil (Microlipid®)	MRS (3.0T)	50%
Peng et al. 2011 21737754 [182]	Vegetable oil Matrix: Water	2-echo Dixon, chemical shift imaging, MRS (7.0T)	0-100%
Mashhood et al. 2013 23172799 [187]	Intralipid® fat emulsion Matrix: Water	2-, 4-, 6-echo Dixon (1.5T, 3.0T)	0-30%
Leporq et al. 2013 23588583 [183]	Olive oil Matrix: Agar	MRS, Multi-echo GRE (1.5T, 3T)	0-50%
Deng et al. 2014 24840769 [18]	Pork visceral fat Matrix: liver tissue	Multi-echo GRE (1.5T)	3.5-46.6%

Hernando et al. 2017 27080068 [52]	Peanut oil Matrix: 2% Agar	Multi-echo GRE (1.5T, 3.0T)	0-100%
Fukuzawa et al. 2017 28770394 [184] Hayashi et al. 2018 29425901 [185]	Vegetable oil (soybean & rapeseed) Matrix: 1% Agar	MRS, Multi-echo Dixon (3.0T)	0-50%
Pooler et al. 2018 29665193 [178]	Peanut oil Matrix: 2% Agar	MRS, Multi-echo GRE (1.5T)	0-100%
Pickhardt et al. 2018 30016142 [53]	Peanut oil Matrix: 2% Agar	Multi-echo GRE (1.5T, 3.0T)	0-100%
Kim et al. 2019 30430684 [186]	Lard Matrix: Agar	MRS, Multi-echo GRE (1.5T, 3.0T)	0-60%
Jaubert et al. 2020 31736146 [179]	Peanut oil Matrix: 2% Agar	6-echo Dixon (1.5T)	0-100%
Hu et al. 2021 33464181 [54]	Fat Fraction Phantom, Model 300 (Calimetrix)	Multi-echo GRE (1.5T, 3.0T)	0-100%
Schneider et al. 2021 33768291 [180]	Peanut oil Matrix: 2% Agar	Multi-echo GRE (3.0T)	0-100%
Zhao et al. 2021 34105167 [51]	Peanut oil Matrix: 2% Agar	Multi-echo GRE (1.5T, 3.0T)	0-100%

Abbreviations: GRE, gradient recalled echo; MRS, magnetic resonance spectroscopy, SS-EPI, single-shot echo planar imaging.

When emulating steatosis, emulsifying agents are typically needed to disperse oil droplets homogeneously throughout the sample. All emulsifiers have amphiphilic properties that interface between the oil and aqueous phases, but some emulsifiers are more soluble in oil than water and vice versa. In the case of phantoms, the most commonly used emulsifier is sodium dodecyl sulfate (SDS), an anionic surfactant [52,61,79,131]. SDS is an extremely hydrophilic emulsifier with a much higher affinity for aqueous media compared to oil-based media [188]. However, some researchers have opted for using oil-soluble emulsifiers such as Span 80 or lecithin [184,189-191]. This allows a lipophilic emulsifier to be added directly to oil during the phantom preparation to

stabilize water-in-oil emulsions rather than dissolving a hydrophilic emulsifying agent in water to stabilize oil-in-water emulsions [190]. However, caution must be taken when using emulsifiers in phantom studies as some emulsifying agents may alter the T1 and T2 relaxation times of the phantom [192].

During the production of steatosis phantoms, it is important to note that the mixing temperature of fat and matrix emulsions and other environmental conditions can affect the quality of the final phantom [189]. Notably, caution must be taken to mix oil and polysaccharide emulsions such as agar/agarose in a limited temperature range of ~40-50°C as mixing them at higher temperatures can cause creaming (i.e., separation of oil and aqueous media) while lower temperatures can solidify polysaccharide matrix solutions, both cases producing inhomogeneous suspensions [189]. When scanning, changes in room temperature will greatly change the resonance frequency of water, but the fat resonance frequency will remain relatively unaffected [146]. In fact, the frequency difference between main fat peak and water at room temperature is 3.5 ppm whereas it is 3.4 ppm in in vivo liver imaging [146,147]. However, changing the temperature of the scanning room to mimic body temperature is not practical, so creation of steatosis phantoms that retain the frequency difference of fat and water as in vivo liver is therefore an unmet need. Nevertheless, maintaining the temperature of the phantom throughout the duration of the scan and adjusting the chemical shift accordingly can produce higher reproducibility and accuracy in FF quantification [146].

Another issue in constructing fat phantoms emulating hepatic steatosis is the discrepancies in sizes between fat globules in in vivo hepatocytes and steatosis phantoms. Hines et al. acquired photomicrographs of a fat-water-SPIO phantom at fat fractions of 10% and 50%, and found that average diameters of the fat droplets were 47 ± 19 μm and 234 ± 66 μm, respectively, which were

much larger than the average diameter of the hepatocytes, 20-25 μm [61,193]. This dissimilarity is not only different from histologic conditions, but it may also contribute to faster R2* decay than in vivo samples [61,79]. Some recent studies have incorporated alternative mixing methods such as hand-held or high-pressure homogenization to reduce the sizes of fat droplets [68,191]. However, microscopy validation has not been performed in these studies to ensure that the diameter of the fat droplets match those of in vivo hepatocytes [68,191].

Fibrosis

Pathophysiology & Morphology

In cases of persistent liver injury such as in alcoholic liver disease, viral hepatitis, iron overload, and steatosis, functional liver tissue is progressively replaced primarily by extracellular matrix (ECM) components in a process called fibrosis [194]. In fibrosis, abnormal amounts of scar tissue replace functional hepatic cells and disrupt internal organ structure that over time limits the blood flow as well as the synthetic capabilities of the liver. Collagen is the most abundant ECM protein, and as fibrosis progresses, the type and composition of collagen changes dramatically with loss and over expression [195,196]. Predominantly, nanofibers of type I collagen with diameters of 300–500 nm replace functional hepatic tissues in fibrosis [197,198]. Initially, fibrosis does not cause noticeable symptoms, but as it worsens, it can lead to portal hypertension and cirrhosis [199]. Cirrhosis is the most advanced stage of liver fibrosis and is evidenced by fibrotic bands, parenchymal nodules, and vascular distortion – all of which derail hepatic function leading to liver failure [200]. The severity of fibrosis is graded semi-quantitatively on histology using the NASH CRN scoring system as follows: 0 (no fibrosis), 1A (mild zone 3 perisinusoidal fibrosis), 1B (moderate zone 3 perisinusoidal fibrosis), 1C (portal/periportal fibrosis only), 2 (perisinusoidal and portal/periportal fibrosis), 3 (bridging fibrosis), and 4 (cirrhosis) [201]. Accordingly, Figure 7

shows representative histology images and fibrosis morphology in patients with different fibrosis grades.

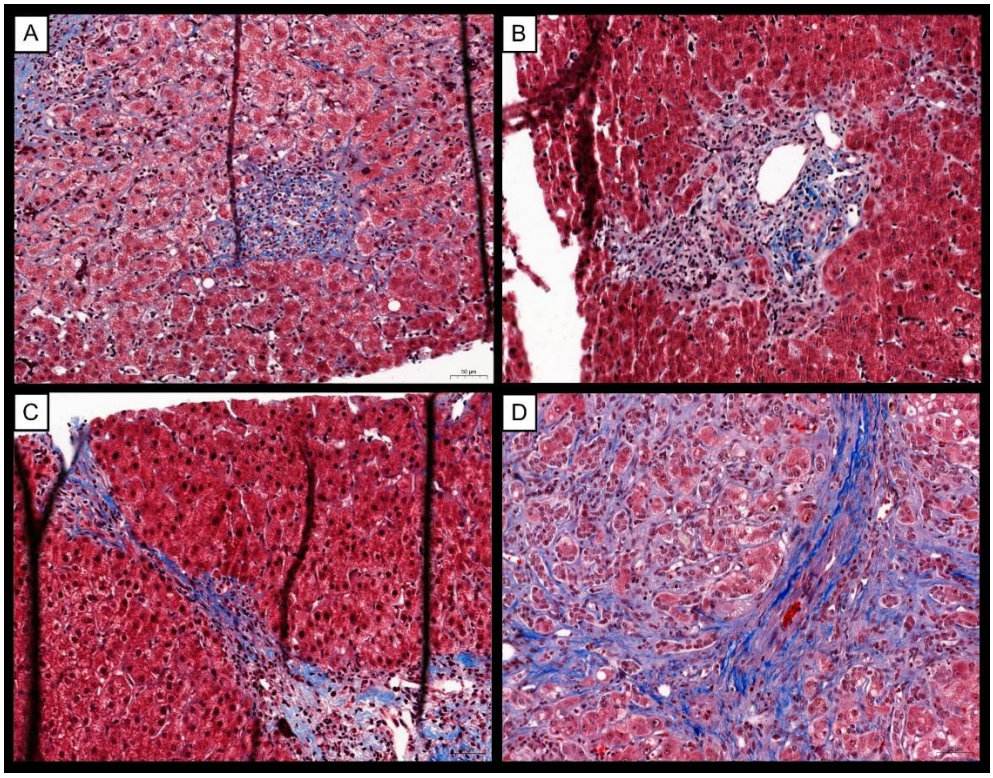

Figure 7. Histology images at 20x of liver biopsy samples showing the deposition of extracellular matrix (primarily collagen) with Mason's trichrome stain in patients with different fibrosis grades. The fibrosis grades of these histology samples based on the NASH CRN scoring system are stage 1, perisinusoidal (A), stage 2, perisinusoidal and periportal (B), stage 3, bridging fibrosis (C), and stage 4, cirrhosis (D).

Quantitative MR Techniques

Elastography

One of the most widely validated MRI techniques used in staging liver fibrosis is magnetic resonance elastography (MRE) [202]. Elastography takes advantage of the relationship between tissue stiffness and the speed of mechanical wave propagation, with waves propagating faster in harder tissues compared to soft tissues, to evaluate collagenous stiffening due to hepatic fibrosis [203]. Specifically, MRE methods use a low frequency vibration source (40-80 Hz) to generate mechanical waves, followed by the utilization of phase contrast techniques with motion encoding

gradients to capture microscopic displacements caused by wave propagation [204,205]. The resulting wave information is then processed to produce tissue stiffness maps using an inversion algorithm to recover mechanical parameters from the displacement data. [204,205]. MRE has been shown to have a high sensitivity and specificity for distinguishing among NAFLD, NASH, fibrosis, and cirrhosis [202,206] and can image longitudinal changes in stiffness in patients over time [207]. Previous studies demonstrated good correlation between MRE stiffness values with both ultrasound elastography (Fibroscan) [62,208,209] and biopsy fibrosis grades [206,210,211], which are often used for clinical diagnosis, thus, making MRE a promising non-invasive alternative for assessing hepatic fibrosis.

Although hepatic MRE is accurate, it can fail in some pathologies such as iron overload in which significant signal decay occurs when using gradient echo based MRE sequences [204,212]. The spatial resolution of MRE can be improved by increasing the shear wave frequency; however, high-frequency waves attenuate quickly, so there is a tradeoff between spatial resolution and propagation distance, thus restricting the depth that can be imaged [213]. Due to this, MRE techniques are limited in use in obese subjects and patients with ascites [214].

T1 Imaging

T1 imaging is arising as an alternative in staging fibrosis to overcome the limitations with MRE. In fibrotic conditions, widespread hepatocyte injury occurs, consequently inducing the recruitment of inflammatory cells. The progression of fibrosis thus leads to chronic inflammation and increases extracellular volume throughout the liver [215]. Because T1 relaxation is altered by the molecular environment of water molecules in tissue, the increased extracellular volume in fibrosis and cirrhosis also prolongs liver T1 values [216]. Therefore, T1 imaging could be used as a noninvasive MRI biomarker for evaluating fibrosis. In the literature, T1 mapping has been used

in staging myocardial fibrosis [217] as well as in many independent studies for assessing hepatic fibrosis [216,218-221]. While T1 has had high diagnostic accuracy, there are some significant drawbacks to this approach. Notably, T1 values can be confounded by other liver pathologies such as inflammation, steatosis, iron overload and portal hypertension [222-225].

Diffusion

Diffusion-weighted imaging (DWI) is one of the first MR techniques used for assessing liver fibrosis. DWI assesses the degree of Brownian motion of water protons by using motion sensitizing gradients and produces image contrast based on the fact that freely moving protons lose signal faster than restricted molecules [226]. Because ECM remodeling leads to a much higher expression of collagen, the flow of water is restricted in fibrotic tissues thus reducing the apparent diffusion coefficient (ADC) values [227,228]. The normalized ADC values for healthy livers are typically ~1.50-1.85 ($x10^{-3}$ mm^2/s) while for fibrotic livers are ~1.30-1.45 ($x10^{-3}$ mm^2/s) [227,229-232]. However, these ADC measurements can vary between vendors and scanners as they are sensitive to b-values and image noise, thus the cutoff values for staging liver fibrosis are difficult to establish [233]. More importantly, ADC values are also affected by iron overload and steatosis, hence limiting their usage for assessing co-occurring diffuse liver diseases [122,234].

Fibrosis Phantoms

The design requirements of fibrosis phantoms are to maintain characteristic relationship between MRI biomarkers (stiffness, T1, and ADC) and fibrosis biopsy grades and cover a wide range of clinical values of MRI biomarkers seen in conditions of liver fibrosis, stiffness: ~2.5-8.0 kPa [206,210,211,235], T1: ~500-1000 ms [45,74], ADC: 1.3 – 1.85 ($x10^{-3}$ mm^2/s) [227,229-232]. A variety of phantom materials are used to emulate the correlation with the three MRI biomarkers used for the evaluation of liver fibrosis as detailed in Table 3. Most frequently, fibrosis phantoms

are created with varying stiffnesses by changing the concentration of the medium. The differing Young's moduli between each sample allows MRE techniques to quantify the degree of stiffness in the phantom, thus allowing the emulation of different fibrosis grades [62]. In vivo, collagen is the primary component that makes up fibrosis pathologies, so some phantom studies have incorporated differing types and concentrations of collagen into their design [63,117]. Apart from collagen, gelatins, hydrogels, and polymers such as B-gel (bovine gelatin), agar, tofu, grenetine gel, Phytagel, Zerdine, silicone, polyvinyl alcohol, and polyacrylamide can also be used in MRE studies for emulating fibrosis [62,65,236-243]. Elastography phantoms are also available from commercial vendors such as Computerized Imaging Reference Systems, Inc. (Zerdine shear wave liver fibrosis phantom), which are designed specifically for ultrasound elastography but have been used in liver MRE studies [239]. Alternatively, commercial MRE phantoms with stiffness values between 2–4 kPa are also available from Resoundant, an MRE manufacturer, for verification and validation of the MRE system. Figure 8 shows a representative set of MRE phantoms with increasing stiffness values made using different concentrations of Phytagel covering the range of stiffness values similar to those seen in liver fibrosis.

Table 3. MRI fibrosis phantom studies listing the phantom materials used, MR techniques, and stiffness/T1/ADC ranges.

Citation PMID	**Phantom Materials**	**MR Technique (Field Strength)**	**Stiffness(kPa)/T1(ms)/ ADC(mm^2/s) Range**
Girometti et al. 2007 17440695 [244]	1) Water 2) Acetone	SE-EPI DWI (1.5T)	1) 2.45 ± 0.05 ($x10^{-3}$ mm^2/s), 2) 4.21 ± 0.05 ($x10^{-3}$ mm^2/s) (ADC)
Yin et al. 2007 17654577 [236]	15% B-gel	GRE MRE (1.5T)	11.2 kPa (G)
Oudry et al. 2009 19856447 [62]	B-gel (5-17.5%) Copolymer-in-oil (3-8.5%)	GRE MRE (1.5T)	~1.0 – 8.0 kPa (G)
Cui et al. 2015 26393236 [245]	Ice water	IVIM DWI (1.5T, 3.0T)	1.13 ± 0.03 ($x10^{-3}$ mm^2/s), 1.21 ± 0.02 ($x10^{-3}$ mm^2/s)
Salameh et al. 2016 26915977 [240]	7% Polyvinyl alcohol gel	Ultra-low field MRE (6.5 mT)	2.3 ± 1.0 kPa (G')
Morisaka et al. 2016 27662640 [65]	Polyacrylamide gel (6.2-7.7%)	SE-EPI, GRE MRE (3.0T)	2.4 - 4.2 kPa (S)
Kishimoto et al. 2017 28057657 [241]	Acrylamide gel	SE-EPI MRE (3.0T)	2.1 - 25 kPa (G')
Solamen et al. 2018 29877194 [237]	1) 55-70% A341 Silicone soft gel 2) 70%,100% A341 Silicone soft gel 3) Soft Tofu and 0.75% Agar 4) Soft Tofu and 0.65% Agar	NLI-MRE (3.0T)	1) 2.5 - 4.6 kPa (G') 2) 4 -15 kPa (G') 3) ~4 kPa (G') 4) 2.7 - 4.2 kPa (G')
Tirkes et al. 2019 31165353 [246]	System Phantom Model 130 (High Precision Devices, Inc.)	VFA, MOLLI, IR-SNAPSHOT, SASHA (1.5T)	20 - 1500 ms (T1)
Cho et al. 2020 33110134 [45]	Gadoterate meglumine (0.1-3 mmol/L) Matrix: Water	SE-IR, VFA, MOLLI (1.5T)	83 - 1310 ms (T1)
Usumura et. al 2021 34019551 [242]	Polyacrylamide gel (12 wt % Acrylamide, 45% Glycerin)	SE-EPI MRE (3.0T)	4.8 - 5.01 kPa (G')
Andoh et al. 2021 34037285 [239]	Zerdine® solid hydrogel (Computerized Imaging Reference Systems, Inc.)	SE MRE (1.5T, 3.0T)	1.7-14.9 kPa (G)

Meneses et al. 2021 34209547 [247]	Human serum albumin (0-20%)	T1 mapping (3.0T)	1800-4000 ms (T1)
Kishimoto et al. 2022 35061118 [243]	Polyacrylamide gel (13%)	SE-EPI MRE (0.3T)	3.1 kPa (G')

Abbreviations: B-gel, bovine skin powder; DWI, diffusion-weighted imaging; GRE, gradient recalled echo; IR-SNAPSHOT, inversion recovery snapshot FLASH; IVIM, intravoxel incoherent motion; MRE, magnetic resonance elastography; MOLLI, modified look-locker inversion recovery; NLI, non-linear inversion; SASHA, saturation recovery single-shot acquisition; SE-EPI, spin-echo echo planar imaging; SE-IR, spin echo inversion recovery; VFA, variable flip angle. **Note:** Elastography results are published using different variables: S, stiffness; G, shear modulus; G', storage modulus

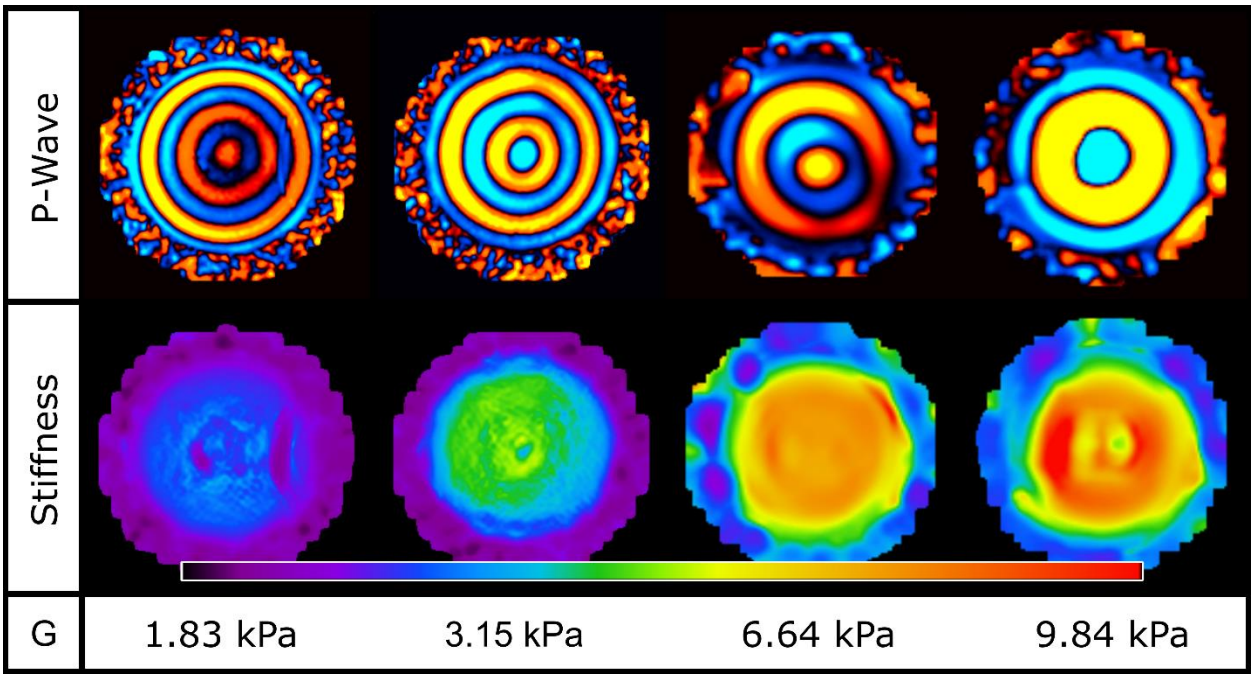

Figure 8: P-wave, stiffness maps, and shear moduli (G) obtained from four magnetic resonance elastography (MRE) phantoms made of Phytagel (1.25 – 1.875%) for emulating liver fibrosis [3]. The stiffness values obtained with MRE ranged from 1.83 – 9.84 kPa.

MRI fibrosis phantoms can also be created using T1 modulators to manipulate T1 times and emulate fibrosis conditions at different grades. Gadoterate meglumine (Dotarem®) is an FDA approved paramagnetic contrast agent capable of shortening T1 relaxation times, hence making it suitable for constructing fibrosis phantoms that are assessed using T1 mapping [45,248]. In contrast, a recent study incorporated human serum albumin as a biomarker for fibrosis as it has

similar relaxation times to human tissues and used it to modulate T1 times by varying its concentration for emulating fibrosis [247]. T1 phantoms are also commercially available from CaliberMRI (ISMRM/NIST System Phantom, Model 130) and Calimetrix (T1 Phantom, Model 300) [246,249]. Both phantoms use $NiCl_2$ as a T1 modulator, but the CaliberMRI System Phantom provides a wider coverage of T1 values of 20-1900 ms, whereas the Calimetrix T1 phantom provides a more limited range of 100-1200 ms; both phantoms' T1 values reported are at 3.0 T.

DWI phantoms are produced from a variety of materials including aqueous solutions (polyvinylpyrrolidone, sucrose, agarose, etc.), polymers (liquid paraffin and alkanes), and pure water. DWI phantoms are also available from commercial vendors such as CaliberMRI (Diffusion Phantom Model 128) and by organizations such as the National Institute of Standards and Technology (NIST) [56,250]. For DWI phantoms mimicking hepatic fibrosis, aqueous solutions of water, acetone or ice water are the most common materials used [228,244,245]. However, phantoms using water and acetone produced higher ADC values than observed in healthy or fibrotic livers but in contrast, using ice water produced ADC values closer to liver tissue [228,244]. Diffusion coefficients have a dependency on field strength and temperature, hence the phantom temperature should be maintained for consistent results [56]. Consequently, DWI phantoms that encompass clinical ranges of fibrosis are still an unmet need in the literature.

Combination Phantoms

Because of the common co-occurrence of iron overload, steatosis, and fibrosis, there have been efforts to combine these pathologies into a standardized set of phantoms, as documented in Table 4. Combination phantoms incorporate the same materials as a single pathology phantom. However, due to the confounding effects between iron, fat, and fibrosis on MRI signals, there have

been attempts to find unique biomarkers for each pathology, namely R2* or susceptibility for iron, FF for fat, and stiffness or T1 for fibrosis. Despite this effort, there are still challenges concerning these confounding effects that must be overcome to create an ideal set of combination liver phantoms.

Table 4: MRI iron-fat and iron-fat-fibrosis phantom studies listing the phantom materials, MR techniques, R2*, fat fraction and T1 ranges.

Condition Mimicked	Citation PMID	Phantom Materials	MR Technique (Field Strength)	R2*(s^{-1})/QSM (ppm) Range	FF (%) Range	T1 (ms) Range
Iron & Fat	Sharma et al. 2009 19243059 [251]	Iron: Ferumoxides (Feridex®, 0-0.5 mM) Fat: Vegetable oil Matrix: 2% Agar	MRS (1.5T)	11-133 s^{-1} (R2)	10, 30%	n/a
Iron & Fat	Hines et al. 2009, 19856457 [61]	Iron: Ferumoxides (Feridex®, 0-50 µg/mL) Fat: Peanut oil Matrix: 2% Agar	2-echo Dixon, Multi-echo GRE, MRS (1.5T)	~25-375 s^{-1}	0-100%	n/a
Iron & Fat	Boll et al. 2010 20308498 [252]	Iron: Ferumoxides (Feridex®, 0.002-0.027 mL) Fat: Caprylic/capric acid (3-12 mL) Matrix: Polyacrylamide	2-echo Dixon (3.0T)	n/a	10-40%	n/a
Iron & Fat	Lee et al. 2011 21591008 [131]	1) Iron: Ferumoxides (Feridex®, 0, 11.2 µg/mL) Fat: Canola oil (0-50%) Matrix: 2% Agar 2) Iron: Feriumoxides (Feridex®, 0-14 µg/mL) Fat: Canola oil (10%) Matrix - 2% Agar	Multi-echo GRE, MRS (1.5T)	1) n/a 2) ~45–100 s^{-1}	0–50%	n/a
Iron & Fat	Fukuzawa et al. 2017 28770394 [184]	Iron: SPIO (0-0.4 mM) Fat: Vegetable oil Matrix: 1% Agar	MRS, Multi-echo Dixon (3.0T)	33–217 s^{-1}	0, 20%	n/a

Iron & Fat	Tipirneni-Sajja et al. 2019 30761652 [44]	Iron: BNF (0-60 µg/mL) Fat: Peanut oil Matrix: 2% Agar	Multi-echo GRE (1.5T, 3.0T)	0–800 s^{-1}	0–40%	n/a
Iron & Fat	Wang et al. 2019 30859893 [191]	Iron: Iron dextran (0-30 µg/mL) Fat: Vegetable oil Matrix: Water	2-echo GRE (3.0T)	~0–900 s^{-1}	0–80%	n/a
Iron & Fat	Mobini et al. 2019 31732894 [79]	Iron: Magnetite (0-723.6 µg Fe/mL) Fat: Peanut oil Matrix: 0.9% Agar	Multi-echo GRE (3.0T)	~45–1000 s^{-1}	0–100%	n/a
Iron & Fat, Iron & Fibrosis	Li et al 2018 29566449 [117]	1) Iron: Gadolinium (0-10.0 mM) Fibrosis - Collagen (0-30%) Matrix – Water 2) Iron: Gadolinium (0-10.0 mM) Fat: Mayonnaise Matrix: Water	Multi-echo GRE (1.5T, 3.0T)	1) 0–150 s^{-1} 0–3 ppm 2) 0–350 s^{-1} 0–3 ppm	0–43.7%	n/a
Iron, Fat & Fibrosis	Zhao et al. 2021 32783200 [68]	1) Iron: $MnCl_2$ (0.17- 1.17 mM) & Magnetite (1.03-34.53 µg/mL) Fat - Peanut oil Matrix - 2% Agar 2) Iron: Magnetite (1.03-53.65 µg/mL) Fat - Peanut oil Fibrosis: $NiCl_2$ (0.28-2.10 mM) Matrix: 2% Agar	Multi-echo GRE, MRS (1.5T, 3.0T)	1) 100–500 s^{-1} 2) 50–600 s^{-1}	1) 5–30% 2) 0–40%	1) n/a 2) 500–1500 ms
Iron & Fat	Colgan et al. (2021) 33783066 [253]	Iron: Magnetite Fat: Peanut oil Matrix: 2% Agar	Multi-echo GRE (1.5T, 3.0T)	200-1000 s^{-1}	0-30%	n/a

Abbreviations: BNF, Bionized NanoFerrite; GRE, gradient recalled echo; $MnCl_2$, manganese chloride; $NiCl_2$, nickel chloride; SPIO, superparamagnetic iron oxide nanoparticles.

Iron-Fat Phantoms

Most literature on combination phantoms features two coexisting pathologies: iron overload and steatosis. For iron overload, iron nanoparticles are most frequently used to emulate the pathology [44,184,191], but contrast agents such as ferumoxides (Feridex®) [61,131,251] and magnetite microspheres [79,253] have been reported as well. Likewise, the most popular substitution for steatosis is peanut oil [44,61,68,79,253], but other vegetable oils such as canola and soybean oil [131,184,191,251] have also been used in iron-fat phantoms. Iron overload and steatosis combination phantoms, however, present additional complications compared to single-pathology phantoms. When placed in an aqueous environment, lipids will form large globules with signal-generating hydrophobic tails in the interior of the bilayer [61]. Conversely, some iron particles are only water-soluble and remain in aqueous solution [61]. Because of this compartmentalization, iron particles, especially of nanometer sizes, may preferentially affect the R2* of water molecules but not that of the R2* of large fat droplets, thereby causing inaccurate R2* and FF measurements, especially at high iron concentrations when a single R2* fitting model is used [61,173]. However, some recent studies used iron microparticles to produce single-R2* behavior in the presence of fat and water to emulate the in vivo conditions and yield accurate R2* and FF measurements [68,79]. Figure 9 shows a representative set of MRI iron-fat phantoms and their R2* and FF maps obtained using the NLSQ fat-water model with single R2* correction. As shown, both measured R2* and FF values showed an excellent linear correlation with iron concentrations and true FFs respectively, except for the highest iron concentration.

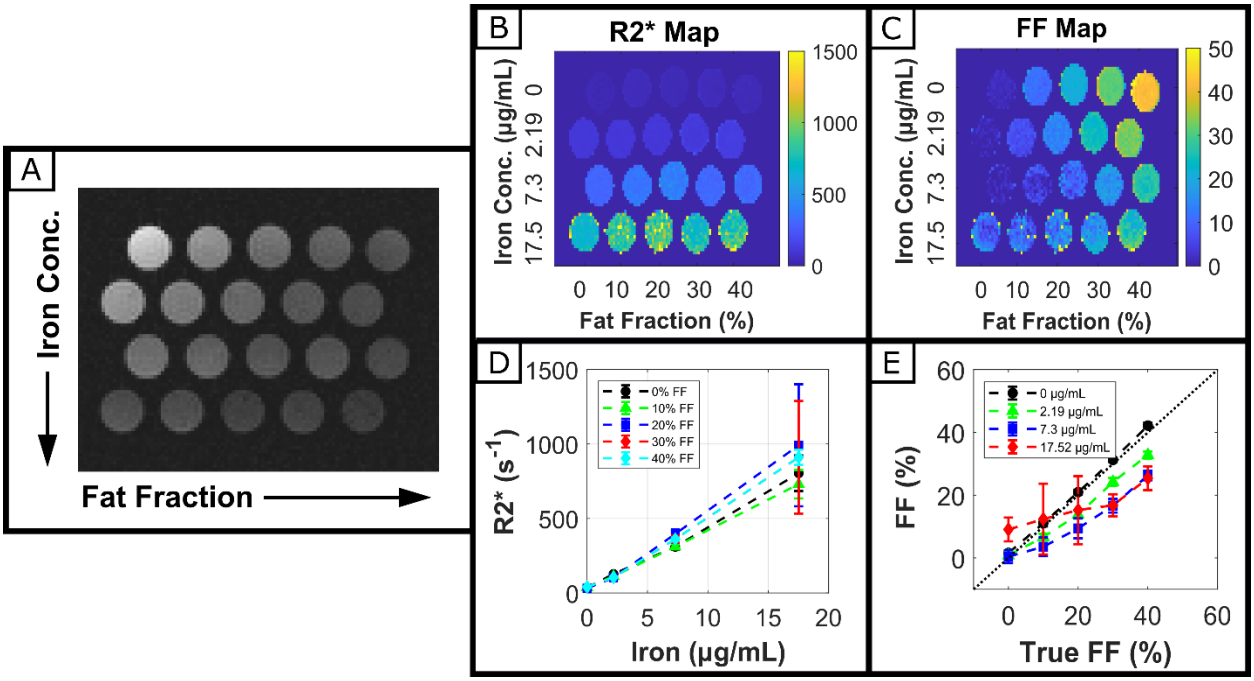

Figure 9. Representative MRI iron-fat phantoms mimicking both liver iron overload and steatosis. BNF iron particles (size: 80 nm) and peanut oil are used to emulate iron overload and steatosis, respectively. MRI magnitude images (A), R2* and fat fraction (FF) maps calculated by fitting a non-linear least squares (NLSQ) multi-spectral fat-water model with R2* correction (B, C) [4], and scatter plots (with error bars) of R2* (s^{-1}) vs iron concentrations (D) and measured fat fraction (FF) vs true FF values (E) are shown for these iron-fat phantoms. Both measured R2* and FF values showed an excellent linear correlation with iron concentrations and true FFs respectively, except for the highest iron concentration.

Iron-Fat-Fibrosis Phantoms

To date, very few studies have integrated fibrosis into iron-fat combination phantom designs to emulate all three diffuse liver pathologies. Zhao et al. incorporated $NiCl_2$ as a T1 modulator for emulating fibrosis and used peanut oil and iron microspheres for mimicking steatosis and iron overload, respectively [68]. $NiCl_2$ is suitable for combination phantoms as it is less sensitive to causing R2/R2* changes in combination iron phantoms [254]. However, iron shortens T1 times, so iron-fibrosis combination phantoms using iron particles in tandem with $NiCl_2$ should correct or account for the decrease in T1 values due to iron, which in fact mimics the shortening of liver T1 in the presence of iron overload [68,255-257]. Further, in this study, the R2* and T1

values in phantoms did not show the similar field strength dependency of these parameters between 1.5T and 3T that is observed in liver in vivo [68]. To investigate the effectiveness of QSM compared to R2* relaxometry for quantifying iron in coexisting pathologies, Li et al. made a set of iron-fibrosis phantoms using gadolinium and collagen, and iron-fat phantoms using gadolinium and mayonnaise [117]. Although it is well documented that iron and fat both influence R2* decay, this study reported that collagen used in fibrosis phantoms also has a positive association with R2* decay [117] and thus, can confound R2*-based HIC estimations. In contrast, susceptibility measurements were not confounded by the presence of fat or fibrosis in these combination phantoms, demonstrating that QSM is a better biomarker for iron estimation in coexisting pathologies [117].

Outlook

The morphology of in vivo tissues is often overlooked when creating liver phantoms emulating iron overload, steatosis, and fibrosis pathologies. Commercial iron particles are only available on the nano scale, but micron-sized particles are needed to mimic the sizes of hemosiderin deposits. The sizes of fat droplets are currently unvalidated in phantoms studies and may be much larger than the size of fat globules in hepatocytes. Therefore, homogenization of fat droplets is needed to reduce their size and mimic in vivo hepatocyte fat storage. The inclusion of materials that simulate fibrosis is important due to its frequent incidence in iron overload and/or steatosis pathologies. Currently, most phantom studies only focus on mimicking iron overload, steatosis or both. However, there is little research on combining these pathologies with the presence of fibrosis. Likewise, most fibrosis phantoms concentrate primarily on stiffness without considering the coexisting pathologies such as iron overload or steatosis. Hence, there is a gap in our understanding of imaging the complex interplay between these diffuse liver diseases in a

standardized phantom model using MRI. Further studies are needed in combining all three pathologies to produce a more precise set of phantoms that correspond to realistic disease progression in in vivo conditions and to investigate and validate MRI techniques for clinical use. Lastly, this study only focused on MRI phantoms mimicking diffuse liver pathologies of iron overload, steatosis, fibrosis and their combination, however there are other features of diffuse liver disease such as inflammation and ballooning as well as other hepatic pathologies (portal hypertension, focal lesions, etc.) and MR techniques such as dynamic contrast enhanced methods that are beyond the scope of this work.

Conclusion

Iron overload, steatosis, and combined overload are common manifestations of diffuse liver disease that may lead to further injury in the form of fibrosis. MRI has opened new avenues for noninvasive quantification of iron overload, steatosis and fibrosis as an alternative to liver biopsy. To standardize MRI techniques, liver phantoms that mimic these pathologies are developed using matrix materials such as water and agar. To simulate iron overload, iron particles are used as R2* modulators or as sources of magnetic susceptibility. Likewise, fatty oils or animal tissues are used to create steatosis phantoms using emulsifiers to ensure homogeneous dispersion. For emulating fibrosis, phantom materials that change stiffness values based on concentration or T1 modulators are used. However, the current phantom studies suffer from morphological discrepancies in phantom design when compared to in vivo sizes of these particles and also from confounding effects on MRI biomarkers in cases of co-occurring iron, fat, and fibrosis pathologies. Future studies should be aimed at selecting phantom materials that emulate the size and distribution of these diffuse liver pathologies in vivo and also consider the complex microenvironment of these

materials and how they impact the MRI signal for creating realistic morphological quantitative liver MRI phantoms.

Chapter IV

Impact of Particle Sizes on MRI Signal Relaxation in Phantoms for Assessment of Hepatic Steatosis and Iron Overload

Introduction

Current hepatic MRI phantoms have little to no standardization and do not consider the morphological sizes of iron particles and fat deposits seen in human tissues which may affect the MRI signal behavior differently [61,79]. Hepatic iron overload is characterized by differing ratios of ferritin (50-70nm) [91] and hemosiderin (0.1-2μm) [93], yet phantom studies typically employ iron oxide particles far larger or smaller than these iron storage proteins [68,122]. Notably, hemosiderin is the primary iron storage protein under conditions of severe iron overload and tends to aggregate in sizes ≥1μm [91], but most commercial iron particles are produced on the nano- scale rather than micro-. Further, the size of fat droplets in hepatic steatosis phantoms are often not controlled and are larger than the average diameter of hepatocytes (20-25 μm) [193]. Iron is speculated to preferentially effect water molecules over lipid molecules due to geographic limitations as the signal-generating lipid tails are located on the interior of globule bilayers and are less accessible to iron particles [61]. As seen on Figure 10 below, increasing the size of lipid globules will thereby allow less interactions between fat and iron as iron is soluble in water, but insoluble in fat [258]. Therefore, iron will be more isolated from lipid molecules than water, and this distinction becomes more apparent with a lesser emulsification. Likewise, increasing the size of iron particles causes a greater proportion of the particle volume to be consisted of the magnetic core rather than the magnetically dead polymer coating, thereby causing greater magnetic field inhomogeneities to be imposed in larger particles [259]. Therefore, the R2* decay rates of fat and water caused by the superparamagnetic effects of iron

particles on surrounding lipid and water molecules respectively in phantoms may be different than what is seen in vivo.

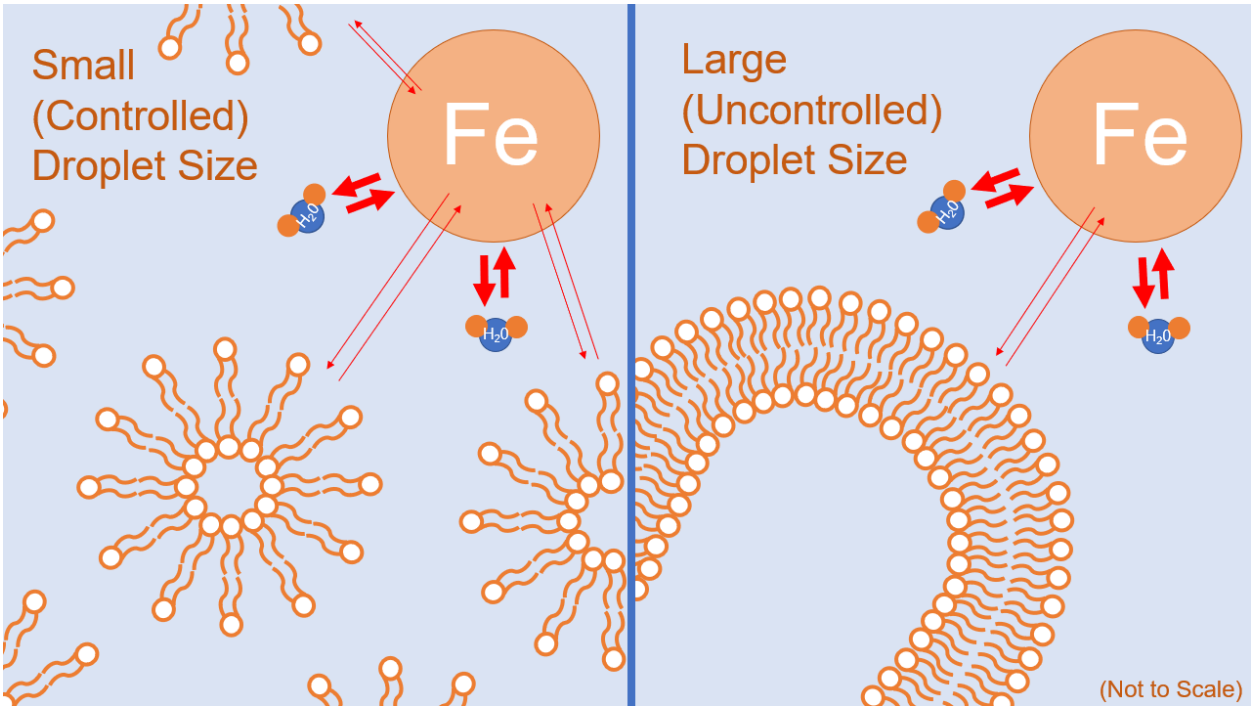

Figure 10. Overview of molecular interactions between iron, water, and lipids. (Left) lipid globules are controlled to be a smaller size via emulsification and/or homogenization, therefore allowing more interactions between iron particles. (Right) uncontrolled lipid globules form via self-assembly and are more geographically isolated from iron due to the large globule size.

Hence, the purpose of this study is to develop and evaluate quantitative iron and fat phantoms with the following goals: i) emulate morphological accuracy of particle size with respect to in vivo hepatic tissues; ii) assess the efficacy of mono-exponential, single-R2*, and dual-R2* fitting; iii) combine materials representing fat and iron to emulate co-occurring hepatic steatosis and iron overload.

Methods

Study Design

Fat Phantom

Fat-water emulsion phantoms were produced at fat fractions of 0%, 10%, 20%, 30%, and 40%. Previous studies claim that traditional methods produce fat droplets that are much greater than in vivo sizes [61]. To control the size of fat droplets, one set of phantoms was created using a stir bar for mixing while another set was mixed more vigorously with a hand-held homogenizer to potentially reduce the size of fat droplets. A total of 10 phantoms were created (5 fat fractions x 2 sets).

Iron-Fat Phantom

Homogeneous fat-water-iron emulsion phantoms were produced at fat fractions of 0%, 10%, 20%, 30%, and 40% at increasing iron concentrations. Three different iron-oxide particles were utilized to emulate iron overload over a wide range of particle sizes: BNF (Bionized Nanoferrite, 0.08 μm), Magnefy™ (0.85 μm), and COMPEL™ (3.3 μm). A total of 40 phantoms were created (5 fat fractions x 5 iron concentrations x 3 sets).

Materials

- *Fat Source:* Peanut Oil (LouAna, Brea, CA, USA) was chosen to mimic hepatic fat for the Iron-Fat phantom study because it has a similar NMR proton spectrum as triglycerides in adipose tissue.
- *Iron Nanoparticles:* Three different iron nanoparticles were used to emulate iron storage molecules in this study. Bionized Nanoferrite-Starch (Micromod, Rostock, Germany) with a diameter of 80 nm were used to emulate the lower bounds of hemosiderin (0.1-3 μm [93,260]). Hemosiderin is typically observed to be closer to the micro-scale, so

Magnefy™ (Bangs Laboratories, Fishers, Indiana) particles of 0.85µm and COMPEL™ (Bangs Laboratories, Fishers, Indiana) particles of 3.3 µm were chosen to encompass larger scale hemosiderin proteins.

- *T1 Modulator:* The spin-lattice relaxation rate T1 was modulated by adding 0.5 mM anhydrous $CuSO_4$ powder (Alfa Aesar, Tewksbury, MA, USA) to decrease the T1 times of the phantom to mimic T1 times seen in human tissues.
- *Base Components:* Each phantom was suspended in a matrix composed of agar powder (Fisher Scientific, Pittsburgh, PA, USA) to create a 2% w/v agar gel. Within this suspension included 43 mM sodium dodecyl sulfate (SDS) (Fisher Bioreagents, Pittsburgh, PA, USA) as a surfactant and 43 mM sodium chloride (NaCl) (Fisher Chemical, Pittsburgh, PA, USA) as a preservative.

Construction

For both studies, a 2% water-agar solution (including SDS, NaCl, and $CuSO_4$) was heated to boil at 90°C and later allow to settle as a gel upon cooling to room temperature after the mixture was completed.

Fat Phantom

Appropriate volumes of peanut oil were allotted into separate beakers from the agar solution. When the temperature of the agar solution fell to an appropriate range (45-55°C) agar was dispensed into the allotted beaker to fill a 50 mL volume. Exceeding this temperature range runs the risk of causing precipitation of the oil (creaming). One set of phantoms was homogenized using a hand-held homogenizer (D1000, Benchmark Scientific, Sayreville, NJ, USA) with a 10mm x 115mm saw tooth generator probe at approximately 15000 rpm, while the second set was mixed with a stir bar and magnetic hot plate at 1400 rpm. After approximately 60

seconds of blending, the mixture of each beaker was poured into 50 mL vials and allowed to settle to a solid state.

Iron-Fat Phantom

Iron-fat-water emulsion phantoms were produced at fat fractions of 0%, 10%, 20%, 30%, and 40% and with varied concentrations of iron nanoparticles. Again, volumes of peanut oil were allocated to separate beakers complementary to the fat fraction needed. When the temperature of the agar solution fell to 45-55°C, agar was dispensed into the allotted beakers to fill a 50 mL volume. Additionally, iron nanoparticles were added with concentrations that match clinical R2* ranges (~0-1000s^{-1}) using a micro-pipettor. A hand-held homogenizer was used to control the size of the fat droplets and distribute the iron nanoparticles homogeneously in solution. After approximately 60 seconds of blending, the mixture of each beaker was poured into 50 mL vials and allowed to settle at room temperature.

Data Acquisition

Light Microscopy

During phantom creation, a 100 µL sample of each phantom was extracted and placed on a glass microscopy slide. The fat droplet morphology of each phantom was then characterized at 200x using bright-field light microscopy with an Olympus BX63 microscope (Olympus, Waltham, MA, USA).

Scanning Electron Microscopy

Scanning electron microscopy (SEM) was used to quantify the size and distribution of the different iron nanoparticles used in this study. Each sample was sputter coated with a gold/palladium (80:20) coat using an EMS550x Sputter Coater (Quorum, Laughton, East Sussex, England) and mounted on 25 mm diameter aluminum specimen stubs. SEM analysis was

performed with a Nova NanoSEM 650 (FEI Company, Hillsboro, Oregon, USA) at a voltage of 20.00 kV, spot size of 3.0, working distance of 5.5-5.2 mm, and a field-free lens mode.

MRI Analysis

Magnetic resonance imaging was performed at 1.5T (MAGNETOM Avantofit, Siemens) using 2D GRE sequences with a monopolar gradient and 2D UTE sequences for iron and fat quantification. Single R2* correction was performed with NLSQ (Non-linear Least Squares) while the dual R2* model was implemented with ARMA (Autoregressive Moving Average) [4,44]. Imaging parameters used for the GRE sequence included: TE1 = 1.2 ms, echo spacing = 1.44 ms, TR = 200 ms, echo train length = 20, flip angle = 35°, 104 x 128 matrix, and 5 mm slices. Likewise, the imaging parameters of the UTE sequence are as follows: TE1 = 0.1 ms, echo spacing = 0.5 ms, TR = 172.2 ms, echo train length = 12, flip angle = 20°, 192 x 192 matrix, and 10 mm slices.

Data Processing and Statistical Analysis

Using MATLAB (2020b), segmentation algorithms based upon binary thresholding were incorporated to determine the radius and area of all fat droplets on light microscopy images.

MATLAB was also used to perform phantom image analysis by performing ROI selection, map generation, and R2* & fat fraction quantification. The code used was an adapted form of the Fat-Water toolbox provided by Hu et al. at ISMRM 2012 [261], Krafft et al. at ISMRM 2013 [177], and Tipineni-Sajja et al [44].

Results

Fat Phantom

The microscopy samples extracted from each steatosis phantom illustrated a considerable discrepancy in size and variability between the two mixing methods. Figure 11 displays a sample from a 40% FF stir bar and homogenized phantom paired against a liver biopsy sample of a patient with moderate steatosis. Visually, it appeared that the size and distribution of the fat globules in the stir bar phantom were more similar to the liver biopsy sample. However, statistical analysis was performed to confirm this assumption as shown on Table 12. Here, the droplet radii in the stir bar data more closely matched the biopsy sample than the homogenized data for the mean, median, and standard deviation. A one-way ANOVA and Tukey's HSD were performed and showed that the homogenized and biopsy data were significantly different with a p-value of 0.01989. Hence, if considering only particle size, the stir bar method would be most appropriate in matching in vivo size and distribution of fat globules.

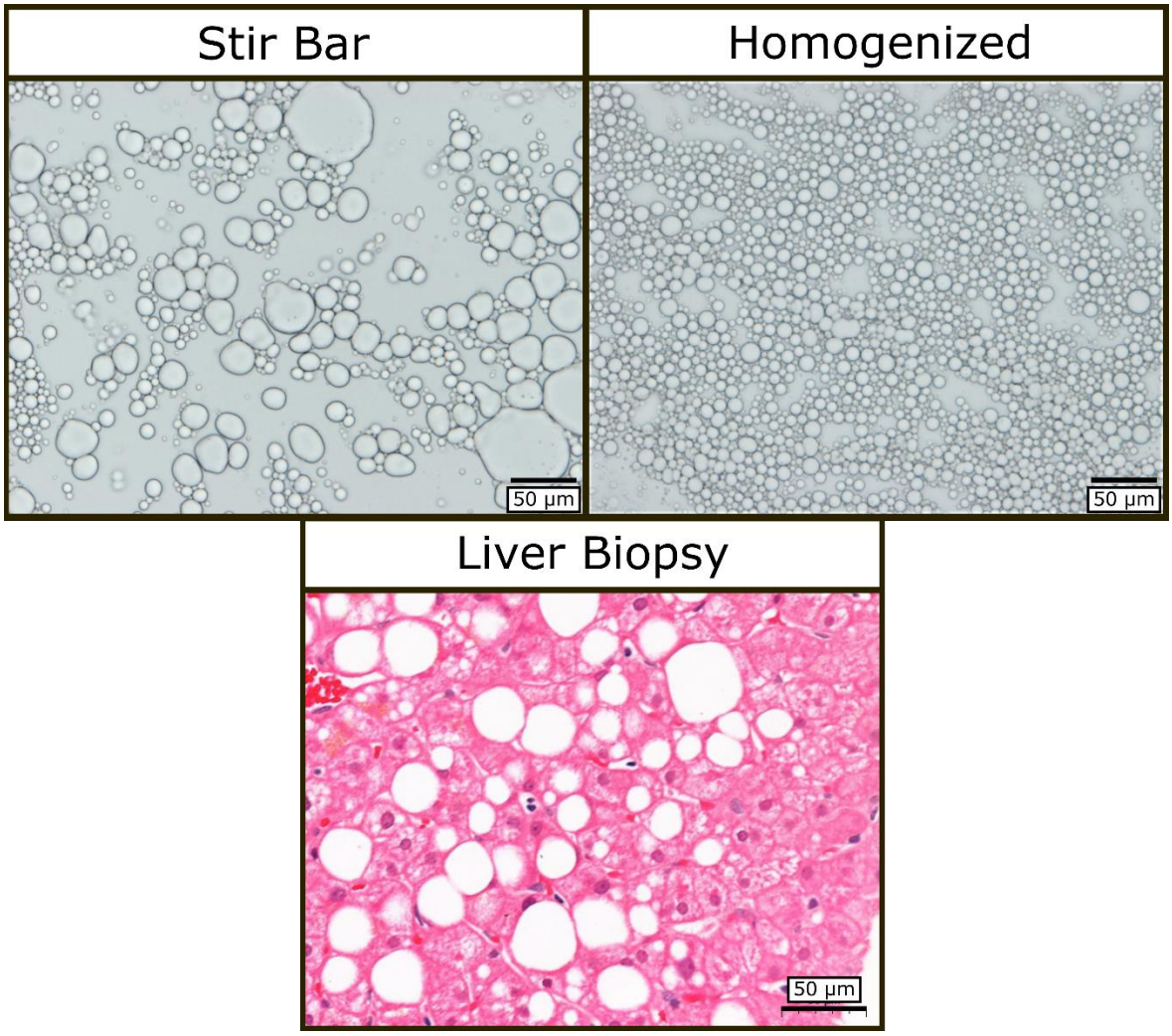

Figure 11: Light microscopy samples of a (top left) stir bar phantom, (top right) homogenized phantom, and (bottom) liver biopsy sample are shown. The phantom samples contain 40% FF while the biopsy sample is graded to be that of a moderately steatotic liver. The stir bar phantom is visually more similar to the biopsy sample that the homogenized phantom.

Table 12: Descriptive statistics results from lipid globules of steatosis phantoms mixed with a stir bar and homogenizer and liver biopsy samples from patients with mild to severe steatosis. The stir bar data more closely aligned with the mean, median, and standard deviations of the biopsy sample than the homogenized data.

Radius (µm)	Stir Bar	Homogenized	Biopsy
Mean	5.563	3.445	5.581
Median	5.629	3.405	4.957
St. Dev.	1.162	0.236	1.519

After evaluating the phantoms via microscopy, MRI analysis was performed. Figure 12 displays FF plots and maps of the steatosis phantoms mixed with a stir bar and homogenizer. Here, it can be seen that the theoretical and experimental FF values of both the stir bar and homogenized phantoms matched closely. However, the NLSQ model slightly underestimated the homogenized phantom FF while ARMA slightly overestimated the stir bar phantom FF. Accordingly, the FF plots reveal that ARMA FF maps were more inhomogeneous than NLSQ and therefore created more standard deviation of FF values in the plots. Overall, the difference in FF signal behavior between both mixing methods is negligible regardless of fitting method.

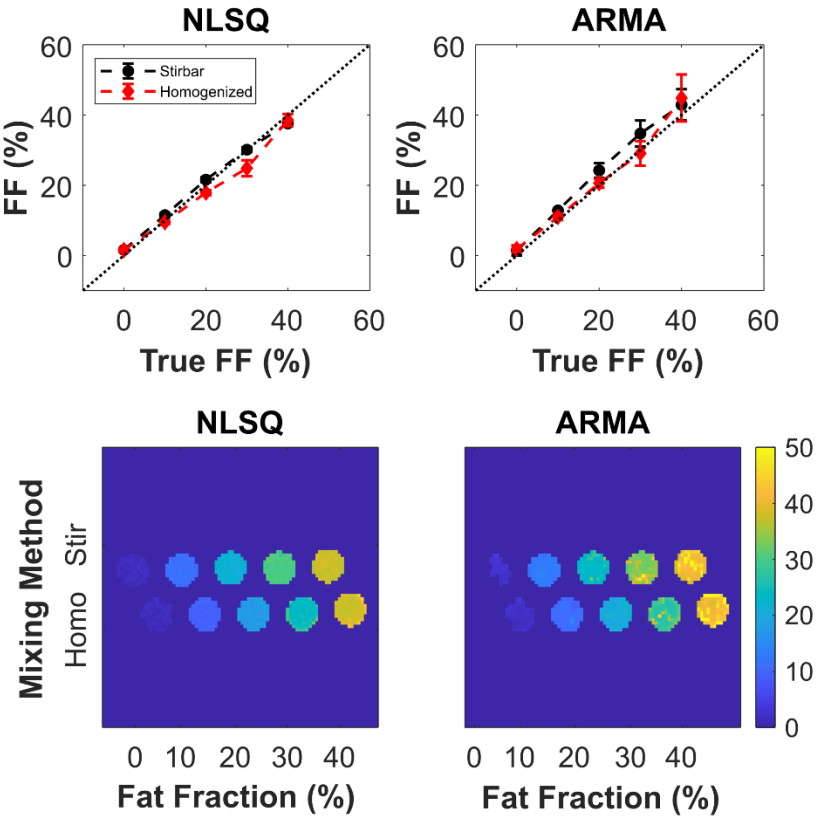

Figure 12: FF plots (top) and maps (bottom) of steatosis phantoms mixed with a stir bar and homogenizer with increasing FF values (0%, 10%, 20%, 30%, and 40%) using NLSQ and ARMA fitting models. The theoretical and experimental FF values of the phantoms matched well.

R2* was also calculated for these phantoms as illustrated in the plots and maps in Figure 13. Here, it can be seen that increasing the FF generally increases R2*. Additionally, the stir bar method produces R2* values slightly higher than the homogenized method, though this is not always the case. All three fitting models largely agree on the R2* values, unlike the FF maps previously.

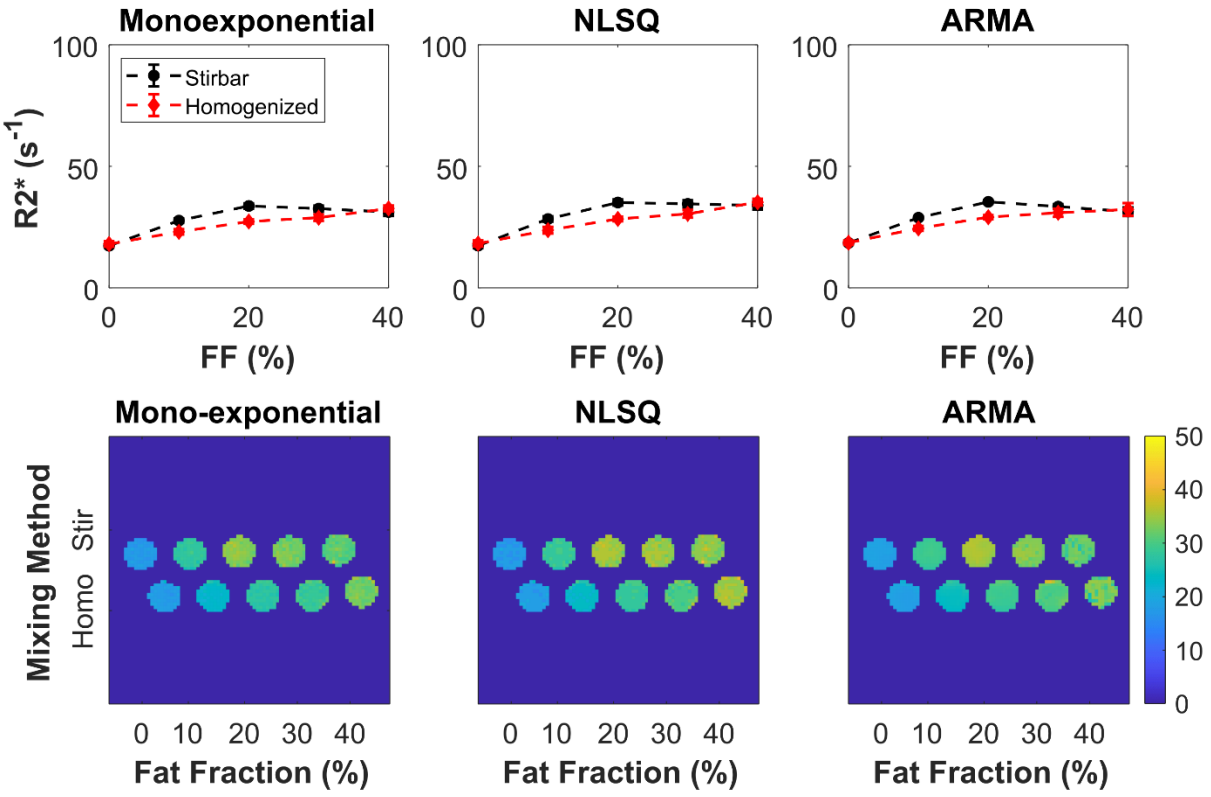

Figure 13: R2* plots (top) and maps (bottom) of steatosis phantoms mixed with a stir bar and homogenizer with increasing FF values (0%, 10%, 20%, 30%, and 40%). All three fitting models (monoexponential, NLSQ, and ARMA) largely agreed on the R2* values.

Iron-Fat Phantom

Scanning electron microscopy confirmed the sizes of the Compel, Magnefy, and BNF particles as per manufacturer specifications. Figure 14 displays each of these three particles at 25000x to further emphasize the difference in size. The Compel and BNF particles tended to distribute homogenously over the slide mount, but the Magnefy particles were more spaced out

and had smaller fragments surrounding them. Element analysis confirmed the presence of iron in each of these particles, including the fragmented Magnefy particles.

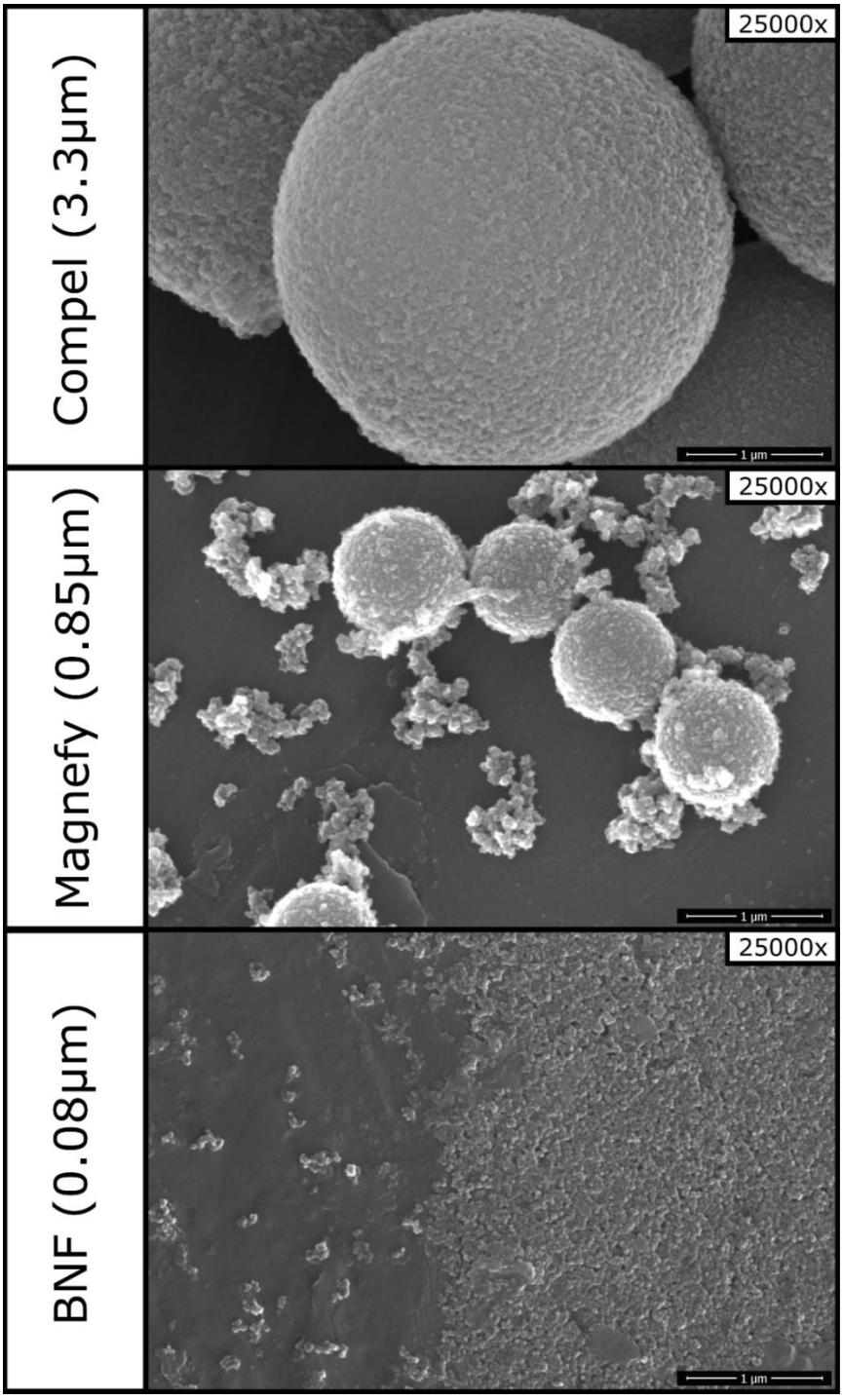

Figure 14: Scanning electron microscopy images of Compel, Magnefy, and BNF nanoparticles are shown at 25000x. Each particle type is noticeably different in size and matches manufacturer specifications.

After verifying the size of each iron particle, all three iron phantom sets were scanned using a GRE sequence and subsequently analyzed using ROI analysis in MATLAB. Figure 15 displays R2* plots for all three particle types using monoexponential, NLSQ, and ARMA models with a GRE sequence. Here, the Compel (3.3 μm) particle delivered the most consistent results with higher FF's producing greater R2* values as expected. However, Magnefy (0.85 μm) and to a lesser degree, BNF (0.08μm), yielded R2* values that increased with iron concentration, but increasing FF did not consistently increase R2* in a linear manner. For the models, ARMA produced the most linear results with the least number of inconsistencies. Mono-exponential evaluated the Compel phantoms well but underperformed on the BNF and Magnefy phantoms. NLSQ completely fails to fit values above $500s^{-1}$ and overestimates the R2* values with large standard deviations.

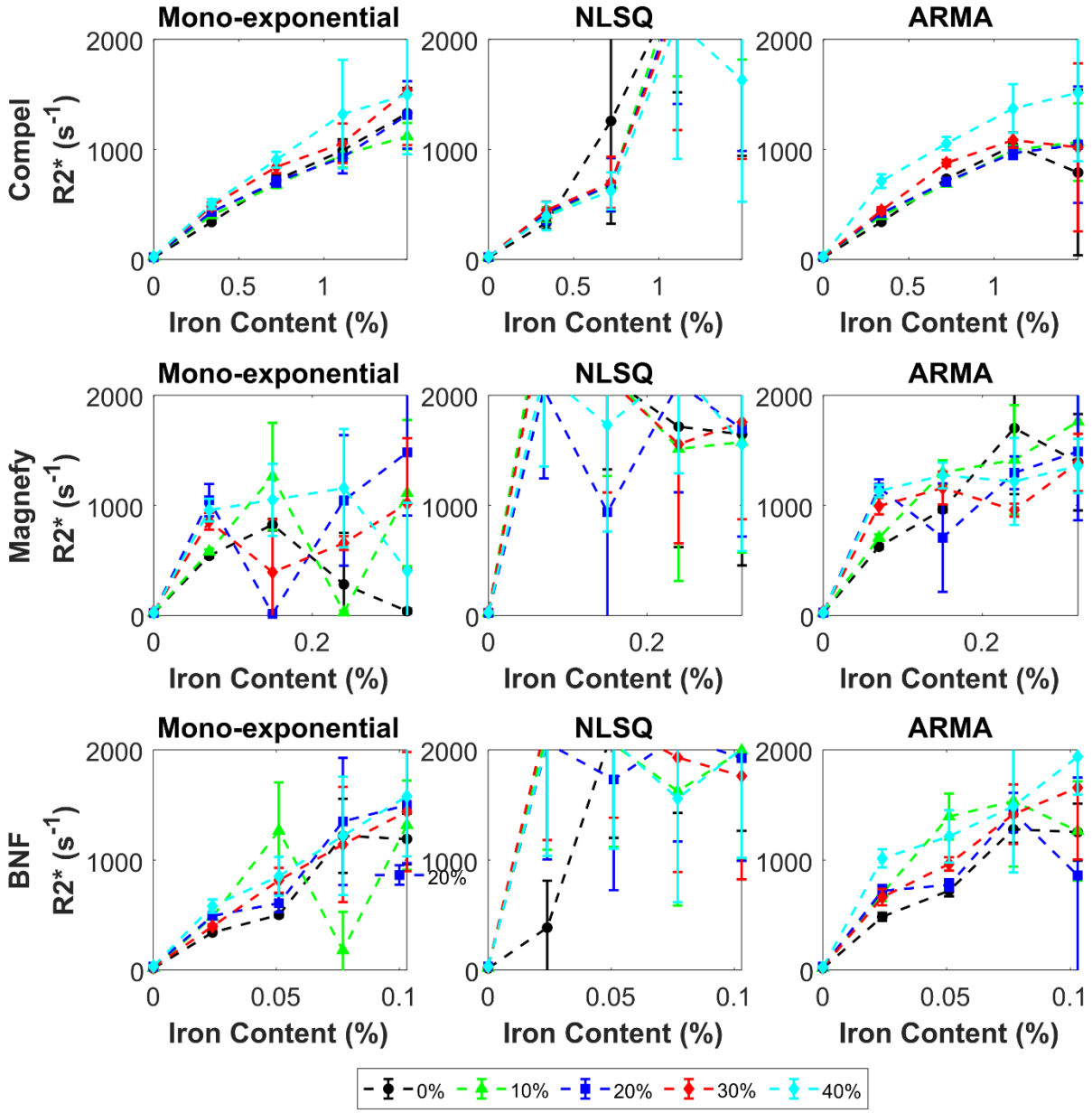

Figure 15: R2* plots of iron-fat phantoms with increasing iron concentrations and increasing FF values (0%, 10%, 20%, 30%, and 40%) are shown. These phantoms were analyzed with a GRE sequence. The three different iron particles used are as follows: Compel (top), Magnefy (middle), and BNF (bottom).

Iron-only phantoms (0% FF) were also of interest to investigate iron-water molecule interactions, so phantoms of each iron type with no oil added were analyzed separately as seen on the plots of Figure 16. Here, the Compel and BNF phantoms generated R2* values that were relatively

linear. However, mono-exponential performed better for the Compel phantoms, while ARMA was better for BNF. Conversely, the Magnefy phantoms did not show a linear trend for R2* and increasing iron in all three models as each failed to quantify the phantom with the highest iron. Notably, NLSQ failed to accurately calculate the R2* in all three phantom sets despite the absence of fat.

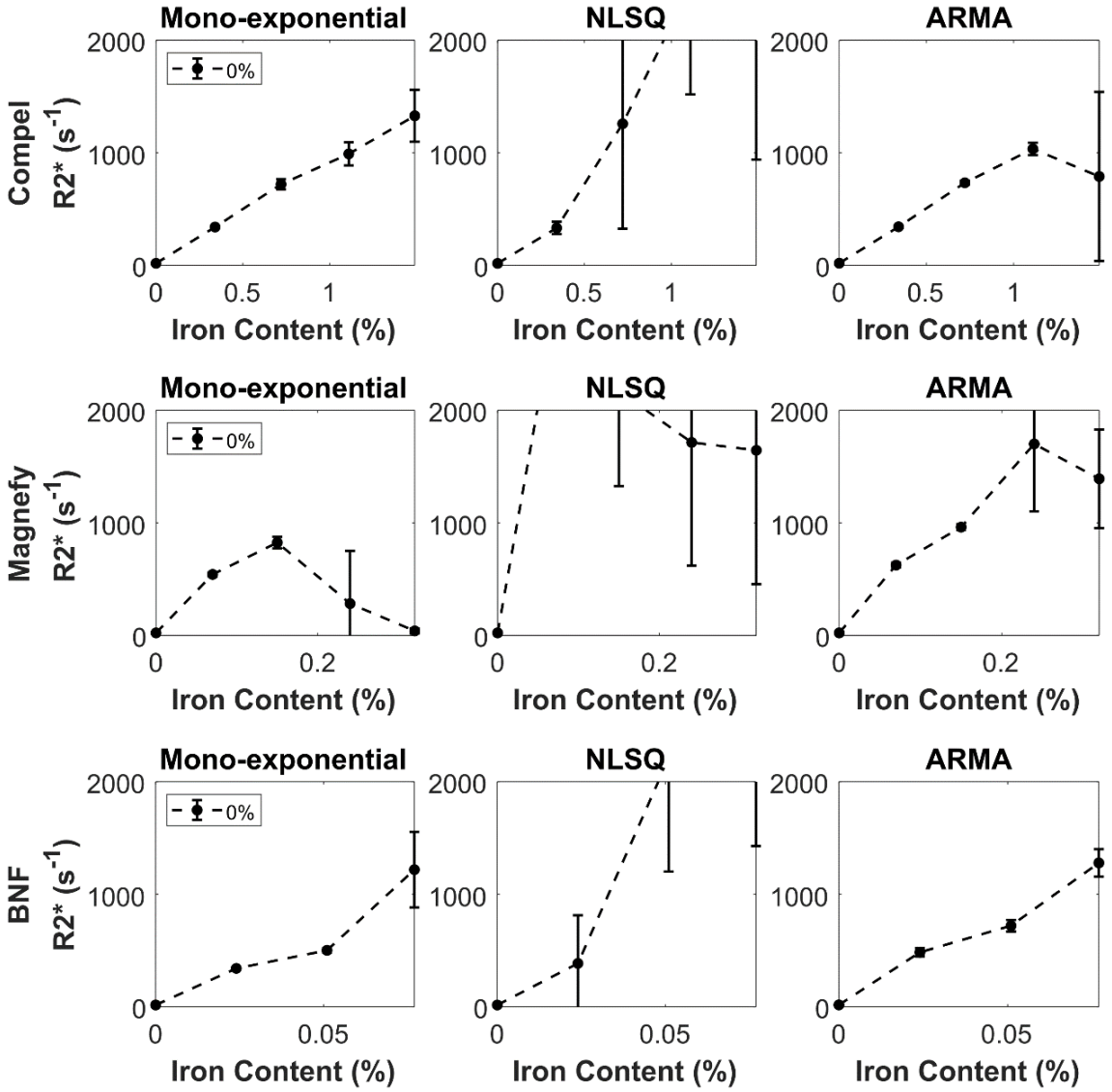

Figure 16: R2* plots of iron-only phantoms with increasing iron concentrations are shown. A GRE sequence was used. The three different iron particles used are as follows: Compel (top), Magnefy (middle), and BNF (bottom). Due to being an outlier, the BNF phantom with the highest concentration was excluded.

To get a top-down view, visual R2* maps were generated from each of these iron-fat phantoms and are displayed on Figure 17. Here, the inhomogeneities in each phantom set are more apparent, but the data still show the trends seen from Figure 15. Mono-exponential performed relatively well, especially for the Compel phantoms, but tended to outright fail to quantify R2* in some BNF and Magnefy phantoms. NLSQ successfully quantified the Compel phantoms, but completely overestimated R2* values in BNF and Magnefy phantoms that had iron in them. Finally, ARMA produced the most homogeneous results of all three models but still has inaccuracies as the iron concentration goes higher.

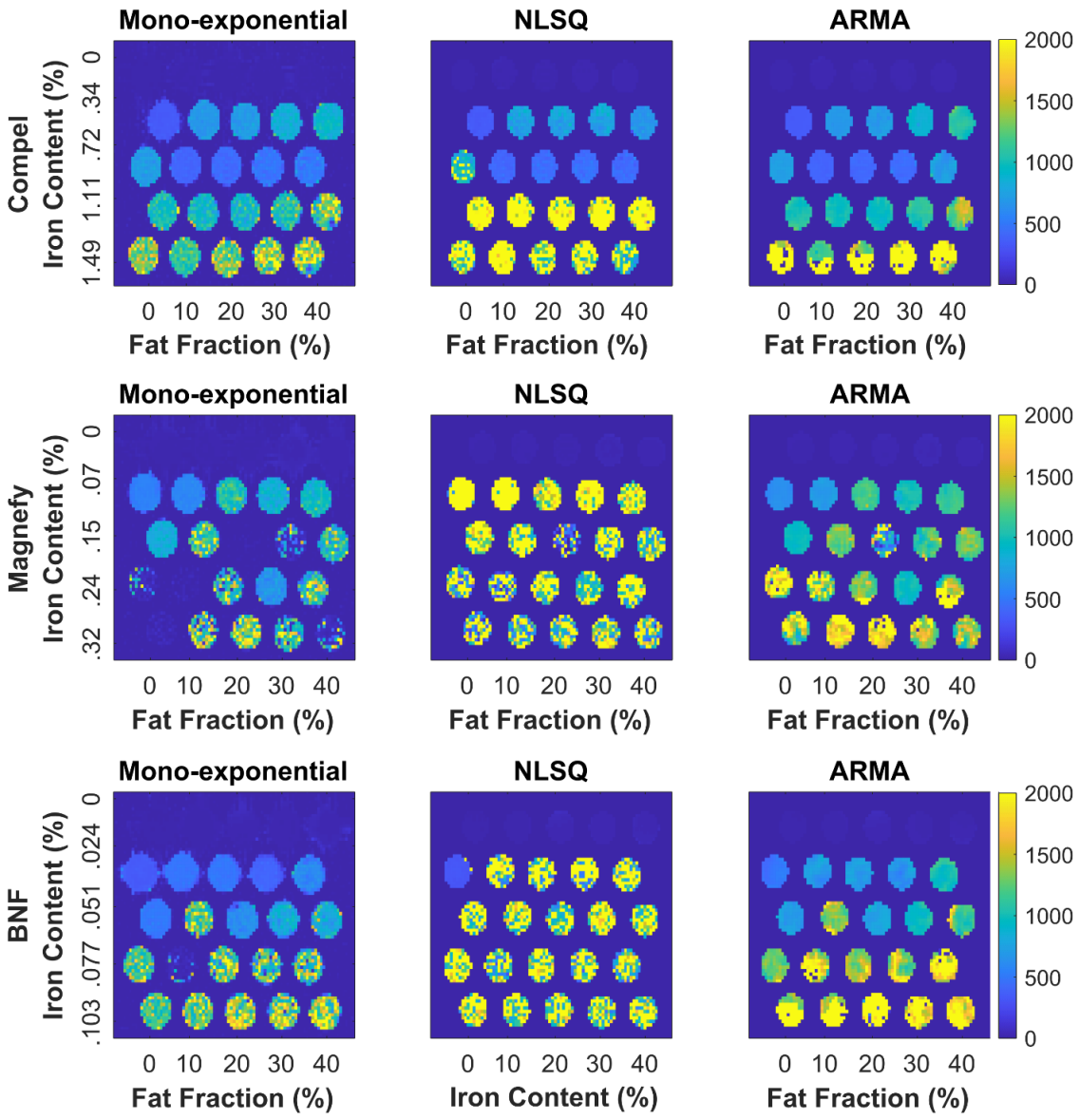

Figure 17: R2* maps of iron-fat phantoms with increasing iron concentrations and increasing FF values (0%, 10%, 20%, 30%, and 40%) are shown. These phantoms were analyzed with a GRE sequence. The three different iron particles used are as follows: Compel (top), Magnefy (middle), and BNF (bottom).

While GRE sequences are traditionally used for quantifying iron and fat, recent literature has investigated the potential for using UTE sequences to accurately quantify extremely high iron contents. Because the highest iron concentrations produced poor results with the GRE sequence, a UTE sequence was also utilized on the iron-fat phantoms. Figure 18 displays R2*

plots for all three particle types using mono-exponential, NLSQ, and ARMA models with a UTE sequence. All three iron-fat phantoms and fitting models performed much better for UTE acquisition, especially NLSQ model. The Compel phantoms still displayed the most linear and consistent results, and this phantom was the only one that correctly illustrated the known phenomenon of increasing FF also increasing the R2* value. UTE acquisition demonstrated substantial improvements for BNF phantoms in showing R2* linearity for the mono-exponential and NLSQ models, but there were few outliers for the 10% FF phantoms. The UTE sequence also revealed that the Magnefy phantoms reached a higher R2* value (~2500s^{-1}) than the Compel and BNF phantoms (1500s^{-1}), which may play a part in the larger standard deviations seen in this phantom. For the models, the mono-exponential and ARMA models agreed closely for most phantoms, but the NSLQ model produced more inconsistencies, albeit with similar trends.

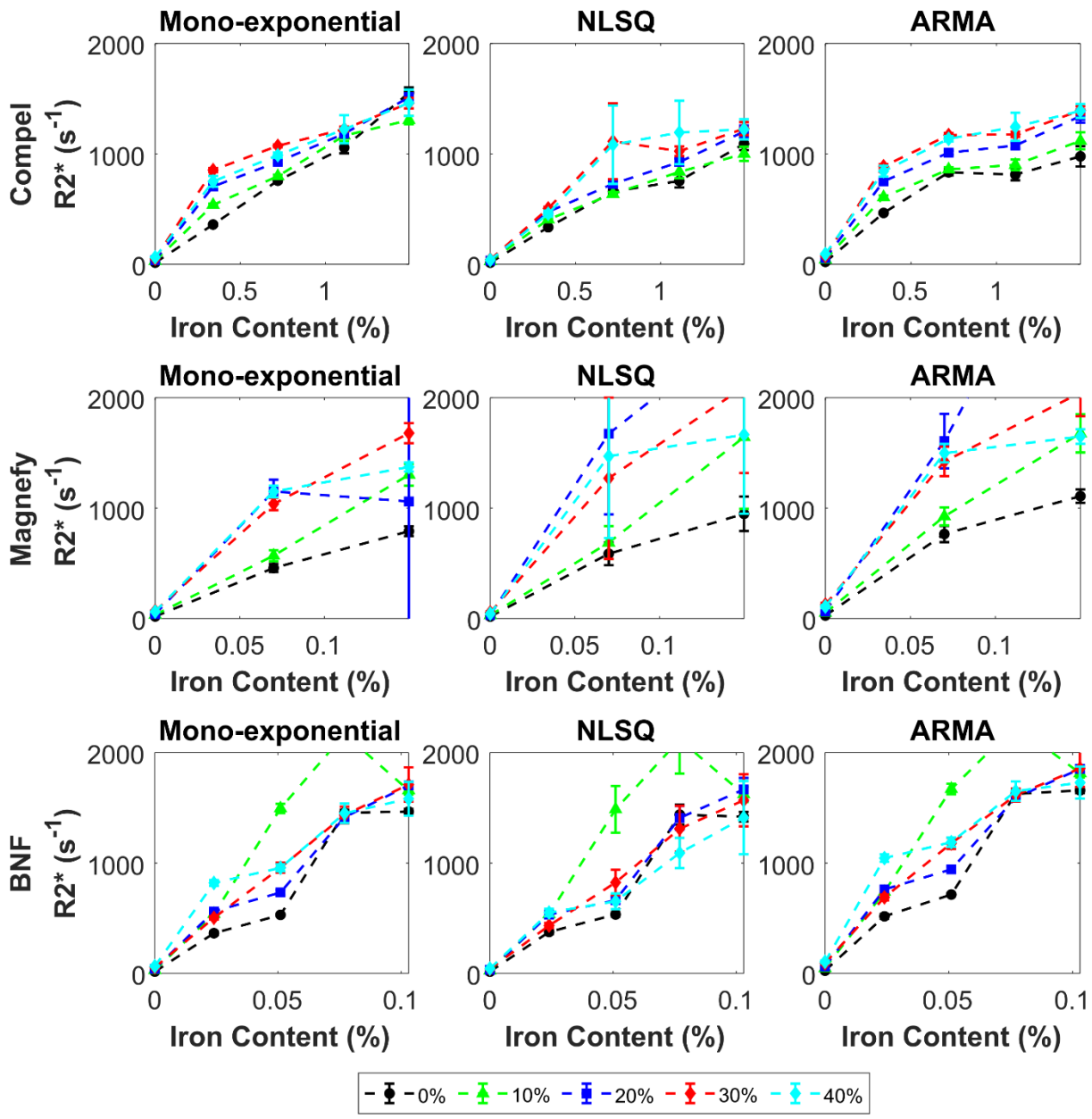

Figure 18: R2* plots of iron-fat phantoms with increasing iron concentrations and increasing FF values (0%, 10%, 20%, 30%, and 40%) are shown. These phantoms were analyzed with a UTE sequence to accurately quantify phantoms with high iron contents. The three different iron particles used are as follows: Compel (top), Magnefy (middle), and BNF (bottom).

Again, iron-only phantoms were independently investigated to analyze iron-water molecule interactions as seen on the plots of Figure 19, with a UTE sequence. The most notable

difference is the drastically improved R2* linearity for the Magnefy phantoms, though all three phantom sets improved. NLSQ and ARMA calculated that the two phantoms of the highest Compel concentration were lower than predicted by the mono-exponential model but also with more standard deviation. However, each model largely agreed on the values for the BNF and Magnefy phantoms which were not as linear, but still showed increasing R2* with increasing iron concentrations. Overall, NLSQ displayed the most uncertainty.

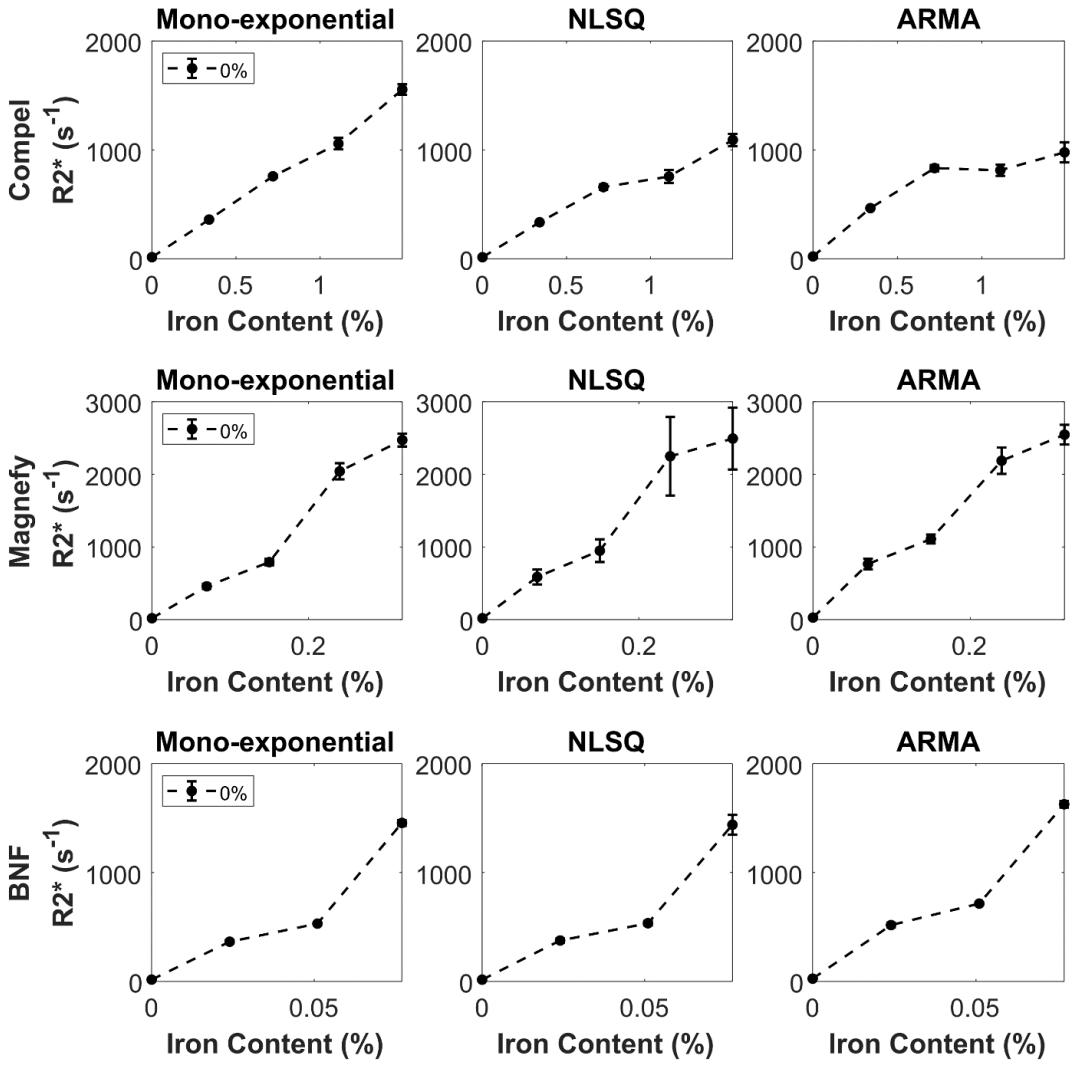

Figure 19: R2* plots of iron-only phantoms with increasing iron concentrations are shown. A UTE sequence was used to accurately quantify phantoms with high iron contents. The three different iron particles used are as follows: Compel (top), Magnefy (middle), and BNF (bottom). Due to being an outlier, the BNF phantom with the highest concentration was excluded.

In addition to the plots, UTE R2* maps were generated to improve visibility of the phantoms and are displayed on Figure 20. Here, some outliers are more apparent such as BNF (0.077%, 10% FF) and Magnefy (0.15%, 20% FF). With the UTE sequence, the trend of R2* increasing with increasing iron is more evident, and the increase in R2* with increasing FF is negligible in comparison. Overall, these maps produce ROI's that are much more homogenous compared to GRE counterparts.

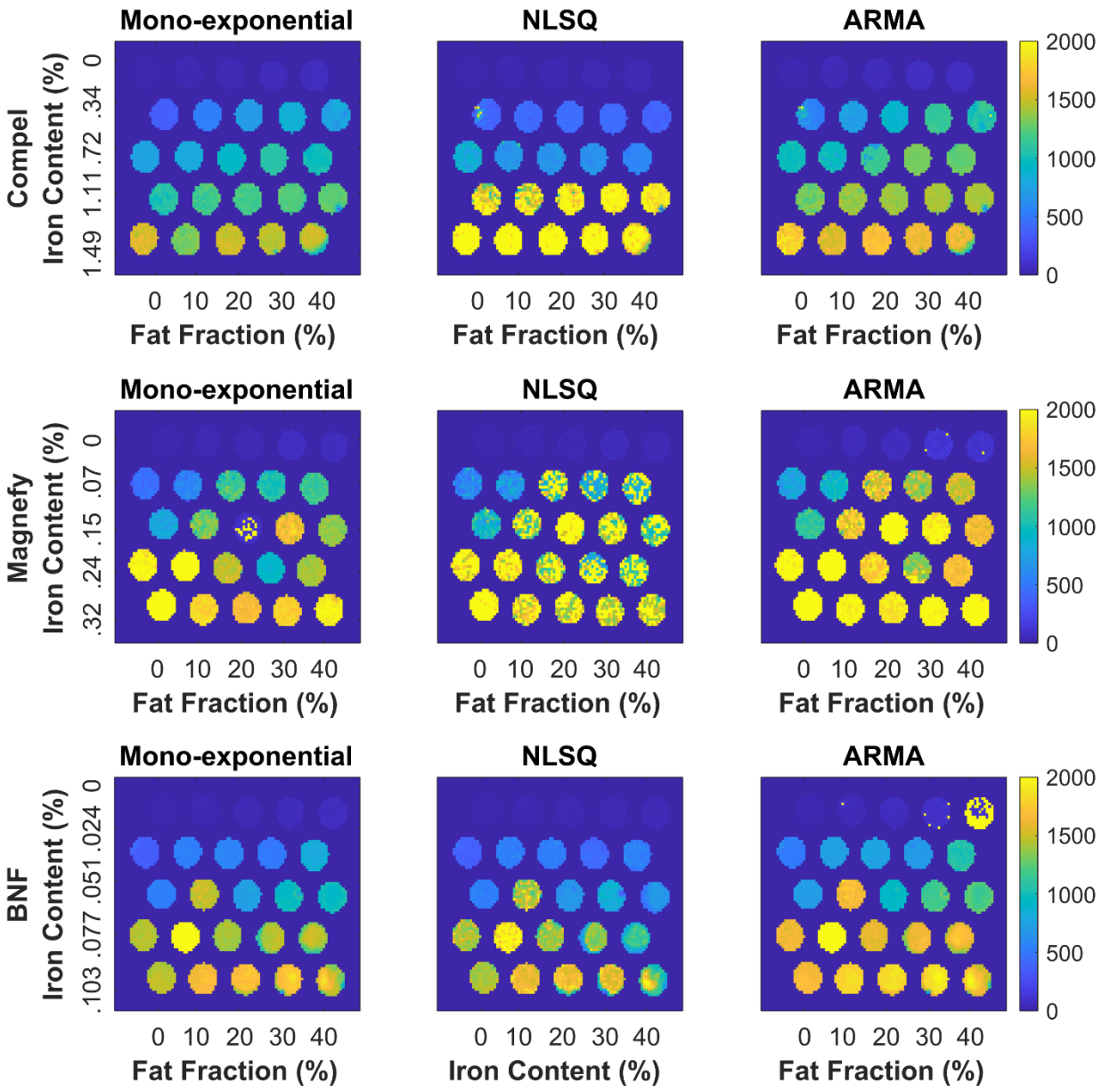

Figure 20: R2* maps of iron-fat phantoms with increasing iron concentrations and increasing FF values (0%, 10%, 20%, 30%, and 40%) are shown. These phantoms were analyzed with a UTE sequence. The three different iron particles used are as follows: Compel (top), Magnefy (middle), and BNF (bottom).

UTE sequences have only been validated in R2* fitting models based on magnitude data [42]. Therefore, complex-based multispectral fat models like ARMA may be unsuitable for mapping FF data. Because of this, GRE sequences were used for the plots seen in Figure 21. In

the Compel phantoms, the quantification of FF becomes increasingly worse as iron increases. At high iron concentrations, NLSQ overestimates FF while ARMA underestimates FF, both of which phenomena have been observed in the literature before [44]. These effects are more extreme in the BNF and Magnefy phantoms in which both models fail to quantify FF in phantoms with any iron present.

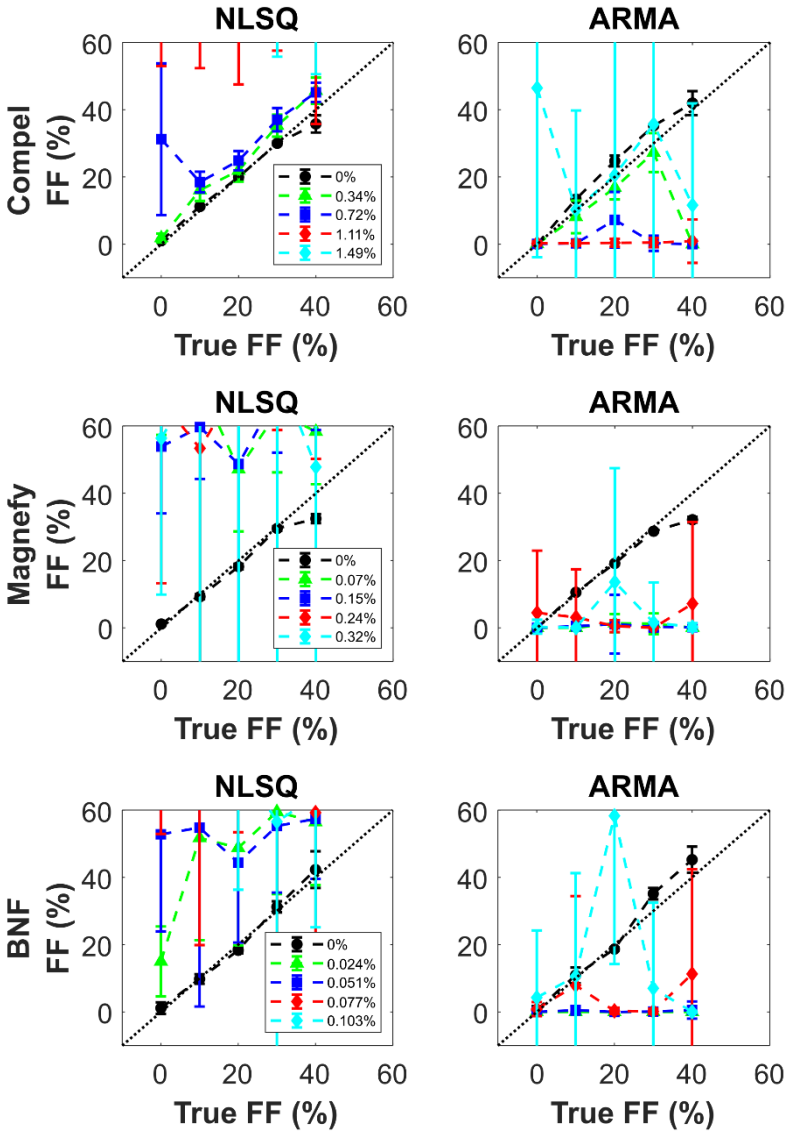

Figure 21: FF plots of iron-fat phantoms with increasing iron concentrations and increasing FF values (0%, 10%, 20%, 30%, and 40%) are shown. These phantoms were scanned with a GRE sequence and analyzed with NLSQ and ARMA fitting models. The three different iron particles used are as follows: Compel (top), Magnefy (middle), and BNF (bottom).

In addition to the FF plots, FF maps were generated to highlight areas of inhomogeneities and estimation failures in Figure 22. Here, it can be seen that ARMA either completely fails to quantify most phantoms or severely overestimates (by > 50% FF) regions of high iron phantoms. The exception to this was the row of 0.34% iron Compel phantoms in which most had an accurate quantification of FF. NLSQ had moderate success in quantifying the Compel phantoms up to 0.72% iron but failed to properly read iron phantoms from the BNF and Magnefy batches. However, both models accurately quantified phantoms without iron, but NLSQ performed better than ARMA on all other phantoms.

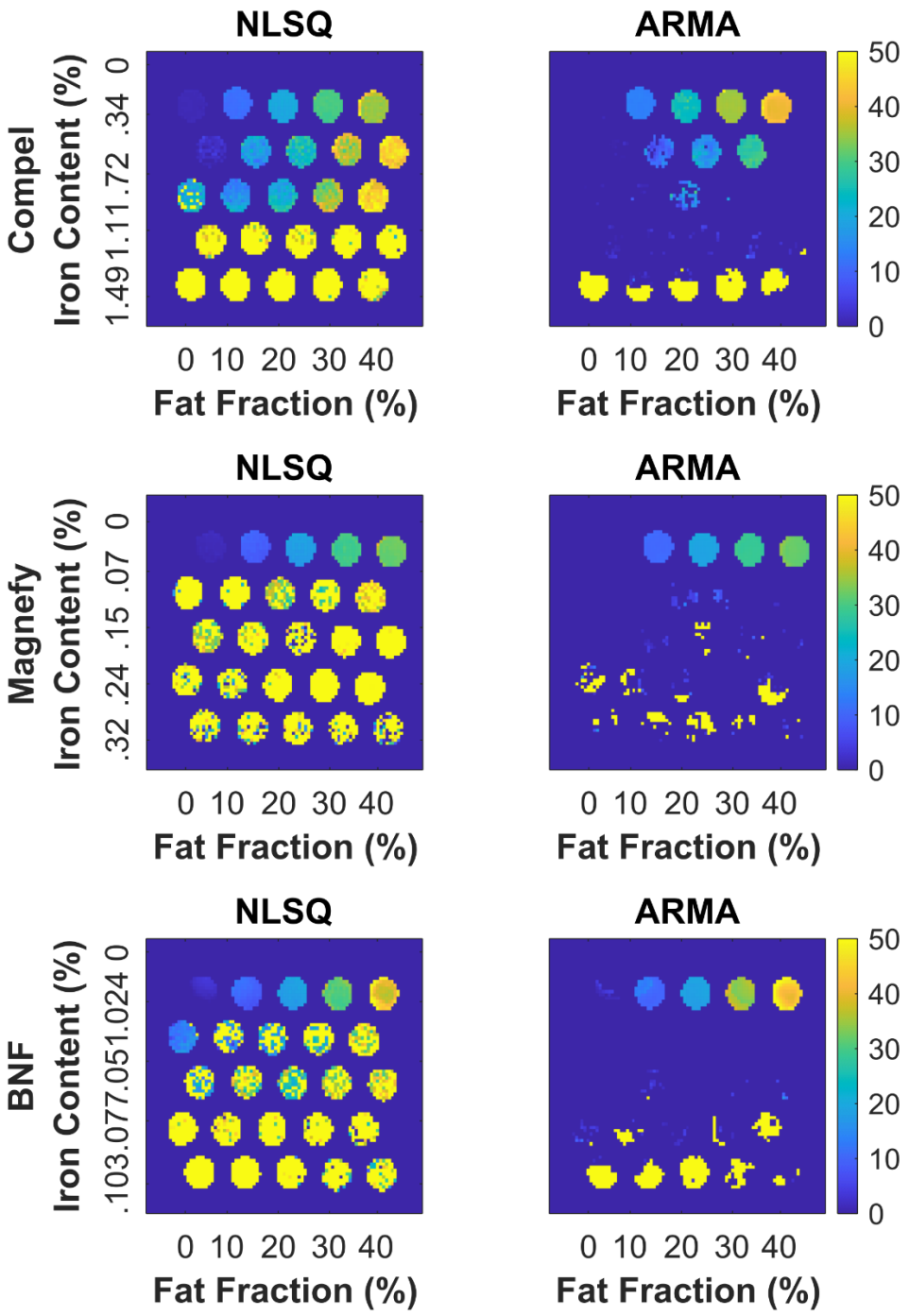

Figure 22: FF maps of iron-fat phantoms with increasing iron concentrations and increasing FF values (0%, 10%, 20%, 30%, and 40%) are shown. These phantoms were scanned with a GRE sequence and analyzed with NLSQ and ARMA fitting models. The three different iron particles used are as follows: Compel (top), Magnefy (middle), and BNF (bottom).

Discussion

In this study, MRI analysis of steatosis and iron overload phantoms was performed using GRE and UTE sequences to investigate the effects of particle size on the MR signal as well as the efficacy of MR fitting models. Evidence of particle size significantly impacting the signal came back inconclusive. Mixing via stir bar and homogenization revealed that stir bar lipid globules matched biopsy data in size and distribution more closely than homogenization, yet the difference in MR signal between both methods was negligible. For iron, SEM analysis validated the sizes listed by the manufacturer for each iron particle type. However, there was no apparent trend of particle size impacting MRI performance. Out of the fitting models, ARMA performed the most optimally for R2* quantification while using a UTE sequence. Conversely, running the NLSQ model with a GRE sequence was preferred for FF quantification.

In the fat phantom, it was found that the stir bar mixing method produced droplets that matched liver biopsy lipid globules more closely in size and distribution than homogenization. However, MRI analysis showed that the difference in fat-water signal behavior between the stir bar and homogenized phantoms was negligible. It is not known if the size and distribution of differing fat droplet sizes would affect the signal behavior of iron on fat differently. The iron-fat phantoms produced for this study were created exclusively with the homogenization method, which was shown to generate fat droplets that were of a more consistent size. Hence, it is possible that wider variations in fat droplets could in turn affect iron-fat interactions which were only partially investigated in this study. Ideally, another batch of phantoms could be created with the stir bar method to be used in comparison against homogenization. However, this is logistically impossible as iron will stick to the magnetic stir bar instead of remaining in solution. Therefore, alternate mixing methods would have to be considered in future work.

From the iron-fat phantoms, there is no clear indication that size of iron particles will noticeably affect the MR signal. Compel (3.3 μm) was the largest particle used and produced the most homogeneous values for both R2* and FF out of all the iron particle types. However, BNF (0.08 μm) outperformed the larger Magnefy (0.85 μm) particles despite a tenfold difference in size. Nonetheless, there is a case to be made about the distribution of the particles affecting the signal as Compel and BNF were consistently seen to be of the same shape and size via SEM, and they dispersed homogeneously over the slide. On the other hand, the Magnefy particles had smaller fragments located alongside particles of the proper size that also contributed to the signal produced by iron. Consequently, it is possible that the inhomogeneities seen in the Magnefy phantom are partially caused by inconsistencies in particle size.

Traditionally, clinical R2* values reach up to ~1000 s^{-1} but can go as high as 2000s^{-1} [35,44,262]. The Compel and BNF phantoms sat adequately in this range by reaching ~1500 s^{-1}. However, the Magnefy phantoms overshot this with a maximum R2* value of 2492 s^{-1}. While theoretically possible in patients, an R2* value this high would be quite rare. Hence, the concentration of Magnefy particles would be cut down in future work to both satisfy an appropriate clinical range and allow for a better comparison to the Compel and BNF particles in phantoms.

Traditionally, T2*-weighted GRE sequences have been employed to image iron via MRI. Because GRE sequences require a highly uniform magnetic field (B_0), any local field inhomogeneities, such as that produced by superparamagnetic iron, will greatly affect the signal output [263]. In short, GRE is very sensitive to iron. However, in cases of severe iron overload, the precision of GRE-based estimations of iron may fail as the signal decays too quickly to be reliably measured [42]. One reason for this failure is the inability of conventional GRE to image

echo times (TE) shorter than 1.0 ms, in which a significant degree of the MR signal may already be lost [42]. Alternatively, UTE sequences can reach TE values as low as 0.1-0.19 ms, thus can measure extremely short-lived signals [42].

As stated previously, UTE sequences have only been validated in R2* fitting models like NLSQ which are based on magnitude data, so models that use complex data such as ARMA may be unsuitable for fitting FF data. Traditionally, UTE sequences utilize fat suppression pulses to reduce streaking artifacts that make arise from subcutaneous fat [42]. However, the UTE sequence used in this study did not have fat suppression built into the sequence, and therefore could theoretically be used for imaging FF maps. Indeed, NSLQ could quantify FF when tested with the UTE sequence; however, ARMA completely failed to quantify FF from all phantoms that contained iron, likely due to low SNR.

From the results of the FF quantification with the GRE sequence, it was seen that NLSQ performed better than ARMA, but it tended to overestimate FF at high iron concentrations. NLSQ has multiple assumptions regarding the fat peaks built into the model as priori information. These assumptions will persist even when no fat is present or under rapid signal decay induced by iron ($R2^* > 500\ s^{-1}$) which may interfere with the quantification of parameters that produce the smallest least square error, therefore leading to false FF values [44]. While NLSQ did successfully quantify the FF of the Compel phantoms of up to ~$800\ s^{-1}$, significant error was displayed for all other phantoms. ARMA behaved similarly as the phantoms without iron or low iron were accurately quantified, but all other phantoms failed. This is likely because ARMA has no assumptions about the fat peaks built into the model, thus it fails in the presence of a low signal. Hence, NSLQ performed slightly better than ARMA.

R2* quantification revealed that the Compel particles followed the most linear distribution out of the three iron particle types, and this linearity is phenomenon that is also seen in the human liver [262]. Out of the fitting models, mono-exponential and ARMA fit the iron-fat phantoms more linearly than NLSQ, with mono-exponential model performing slightly better than ARMA. However, the mono-exponential model does not consider the presence of fat [2], so ARMA may be constructing the signal behavior more accurately despite the difference in linearity. NLSQ suffers from the same issues as before, as increasingly high iron in tandem with high FF causes more inhomogeneities in R2* quantification. Because of this, some investigators have tried using the NLSQ model to measure R2* without incorporating priori information on the fat peaks [264]. Because our phantoms feature fat, this was not a feasible alternative.

Conclusion

Despite controlling the size of fat and iron particles in steatosis and iron overload MRI phantoms, evidence showing that particle size impacts the signal to a significant degree remains inconclusive. Reproducing these results with different mixing methods and utilizing particles with homogeneous distributions may be necessary to give a definitive conclusion. UTE sequences improved the estimation of R2* in the presence of fat, but GRE sequences are still necessary for accurate FF quantification in the presence of iron. All three fitting models had their merits with R2* quantification most accurately being portrayed under the mono-exponential model under conditions of no fat and ARMA under conditions of iron and fat. Additionally, NLSQ handled FF quantification more consistently than ARMA. This study demonstrates different sequencing and post-processing assessments are critical for the analysis of sensitive biomarkers such as R2* and FF.

Chapter V

Conclusion and Future Work

Clinical quantitative MRI techniques are at their infancy, yet they provide non-invasive and sensible data that rival established methodologies such as biopsy. This work imitates realistic MRI signal behavior and clinical ranges of biomarkers in imaging phantoms while simultaneously addressing discrepancies between phantom media particle size and molecular interactions inside in vivo tissues. Ultimately, definitive conclusions regarding the impact of particle size on the MR signal cannot be drawn from this study, but several improvements in the design may reveal more solutions.

While the preceding analysis was theoretically sound, there are a few key changes that could be made to the experimental setup to improve upon the validity of this work. This study was fairly limited in scope to the available mixing methods and iron particles available on the market. To control the size of fat droplets, a magnetic stir bar and hand-held homogenizer were used as they are the most prevalent instruments used in hepatic phantom literature. However, there have been reports of other methods being used to develop phantoms [61,265]. In future studies, several more mixing instruments and methodologies could be used to compare against liver biopsy samples, including gentle inversion, overhead stirring, and ultrasonication. Also, while no apparent trend could be observed on the MR signal due to particle size, the polymer coating of each type of iron particle contained differing compositions and thus could have impacted internuclear interactions. Ideally, the same coating should be used for each size as the varying polymers may have differing solubilities, crosslinking agents, and charges, among other variables. Unfortunately, commercial particles that both covered the clinical ranges of hemosiderin and were coated with the same polymer could not be located for this study. Future

studies could either synthesize particles with a wide range of sizes and a consistent polymer composition or utilize commercial particles that meet these conditions.

In this study, there are several more pathologically relevant features that could be incorporated into the phantom design. As stated previously, iron overload is a heterogeneous disease with a mottled distribution across the liver. The severity of hepatic iron overload also impacts the amount of ferritin converted to hemosiderin with more hemosiderin forming in severe iron overload. Hence, the particle size of iron overload phantoms should theoretically reflect the ratios of ferritin to hemosiderin if preserving the integrity of tissue emulation. The effect this may have on the MRI signal may be minuscule, but could be investigated, nonetheless. Additionally, this work was primarily aimed at studying hepatic iron overload and steatosis as they often co-occur, and the resulting MR signal from both pathologies are known to confound quantification of each other. However, fibrosis often results from advanced cases of these diffuse liver diseases and can be traced with other MR biomarkers such as elastography or T1w imaging, so incorporating this pathology into combination iron overload and steatosis phantoms may be worthwhile.

In summary, more mixing methods along with a more consistent polymer coating could reveal additional insights on the impact of particle size in steatosis and iron overload phantoms, all of which could be expanded on to further mimic other hepatic tissues and severities.

References

1. Block KT, Chandarana H, Milla S, Bruno M, Mulholland T, Fatterpekar G, Hagiwara M, Grimm R, Geppert C, Kiefer B, Sodickson DK (2014) Towards Routine Clinical Use of Radial Stack-of-Stars 3D Gradient-Echo Sequences for Reducing Motion Sensitivity. jksmrm 18 (2):87-106.
2. Hankins JS, McCarville MB, Loeffler RB, Smeltzer MP, Onciu M, Hoffer FA, Li CS, Wang WC, Ware RE, Hillenbrand CM (2009) R2* magnetic resonance imaging of the liver in patients with iron overload. Blood 113 (20):4853-4855.
3. Thamizharasan G, Russell A, Beinkampen J, Holtrop J, Williams J, Tipirneni-Sajja A (2019) Magnetic Resonance Elastography Phantoms to Mimic Liver Tissue Stiffness and Validation with Uniaxial Compression Test. Paper presented at the Biomedical Engineering Society Meeting,
4. Hernando D, Liang ZP, Kellman P (2010) Chemical shift-based water/fat separation: a comparison of signal models. Magn Reson Med 64 (3):811-822.
5. Abbaspour N, Hurrell R, Kelishadi R (2014) Review on iron and its importance for human health. J Res Med Sci 19 (2):164-174.
6. Kohgo Y, Ikuta K, Ohtake T, Torimoto Y, Kato J (2008) Body iron metabolism and pathophysiology of iron overload. Int J Hematol 88 (1):7-15.
7. Sirlin CB, Reeder, S.B. (2012) MRI Quantification of liver iron. Magn Reson Imaging Clin N Am:1-40.
8. Alamri ZZ (2018) The role of liver in metabolism: an updated review with physiological emphasis. International Journal of Basic & Clinical Pharmacology 7 (11).
9. Takahashi Y, Fukusato T (2014) Histopathology of nonalcoholic fatty liver disease/nonalcoholic steatohepatitis. World J Gastroenterol 20 (42):15539-15548.
10. Yokoo T, Browning JD (2014) Fat and iron quantification in the liver: past, present, and future. Top Magn Reson Imaging 23 (2):73-94.
11. Nelson JE, Klintworth H, Kowdley KV (2012) Iron metabolism in Nonalcoholic Fatty Liver Disease. Curr Gastroenterol Rep 14 (1):8-16.
12. Fazeli Dehkordy S, Fowler KJ, Mamidipalli A, Wolfson T, Hong CW, Covarrubias Y, Hooker JC, Sy EZ, Schlein AN, Cui JY, Gamst AC, Hamilton G, Reeder SB, Sirlin CB (2019) Hepatic steatosis and reduction in steatosis following bariatric weight loss surgery differs between segments and lobes. Eur Radiol 29 (5):2474-2480.
13. Idilman IS, Akata D, Ozmen MN, Karcaaltincaba M (2016) Different forms of iron accumulation in the liver on MRI. Diagn Interv Radiol 22 (1):22-28.
14. Villeneuve J, Bilodeau M, Raymond L, Côté J, Lefebvre M (1996) Variability in hepatic iron concentration measurement from needle-biopsy specimens. Journal of Hepatology 25:172-177.
15. Angelucci E, Baronciani D, Lucarelli G, Baldassarri M, Galimberti M, Giardini C, Martinelli F, Polchi P, Polizzi V, Ripalti M, et al. (1995) Needle liver biopsy in thalassaemia: analyses of diagnostic accuracy and safety in 1184 consecutive biopsies. Br J Haematol 89 (4):757-761.
16. Neuberger J, Patel J, Caldwell H, Davies S, Hebditch V, Hollywood C, Hubscher S, Karkhanis S, Lester W, Roslund N, West R, Wyatt JI, Heydtmann M (2020) Guidelines on the use of liver biopsy in clinical practice from the British Society of Gastroenterology, the Royal College of Radiologists and the Royal College of Pathology. Gut 69 (8):1382-1403.

17. Labranche R, Gilbert G, Cerny M, Vu KN, Soulieres D, Olivie D, Billiard JS, Yokoo T, Tang A (2018) Liver Iron Quantification with MR Imaging: A Primer for Radiologists. Radiographics 38 (2):392-412.
18. Deng J, Fishbein MH, Rigsby CK, Zhang G, Schoeneman SE, Donaldson JS (2014) Quantitative MRI for hepatic fat fraction and T2* measurement in pediatric patients with non-alcoholic fatty liver disease. Pediatr Radiol 44 (11):1379-1387.
19. Edelstein WA, Mahesh M, Carrino JA (2010) MRI: time is dose--and money and versatility. J Am Coll Radiol 7 (8):650-652.
20. Purcell EM, Torrey HC, Pound RV (1945) Resonance Absorption by Nuclear Magnetic Moments in a Solid. Phys Rev 69 (1-2).
21. Bloch F, Hansen WW, Packard M (1946) The Nuclear Induction Experiment. Phys Rev 70 (7-8).
22. Crooks L, Herfkens R, Kaufman L, Hoenninger J, Arakawa M, McRee R, Watts J (1981) Nuclear magnetic resonance imaging. Prog Nucl Med 7:149-163.
23. Patching SG NMR-Active Nuclei for Biological and Biomedical Applications. In, 2016.
24. Bhinderwala F, Evans P, Jones K, Laws BR, Smith TG, Morton M, Powers R (2020) Phosphorus NMR and Its Application to Metabolomics. Anal Chem 92 (14):9536-9545.
25. Mlynarik V (2017) Introduction to nuclear magnetic resonance. Anal Biochem 529:4-9.
26. Berger A (2002) Magnetic resonance imaging. BMJ 324 (7328):35.
27. Lugauer F, Wetzl J (2018) Medical Imaging Systems

An Introductory Guide. In: Maier A, Steidl S, Christlein V, Hornegger J (eds) Medical Imaging Systems: An Introductory Guide, doi:10.1007/978-3-319-96520-8. Cham (CH).
28. Siemens-Aktiengesellschaft. Berlin W, Solutions MM, Hendrix A (2003) Magnets, spins, and resonances: an introduction to the basics of magnetic resonance. Siemens AG,
29. Currie S, Hoggard N, Craven IJ, Hadjivassiliou M, Wilkinson ID (2013) Understanding MRI: basic MR physics for physicians. Postgrad Med J 89 (1050):209-223.
30. Chavhan GB, Babyn PS, Thomas B, Shroff MM, Haacke EM (2009) Principles, techniques, and applications of T2*-based MR imaging and its special applications. Radiographics 29 (5):1433-1449.
31. Müller M (2015) Fourier Analysis of Signals. In: Fundamentals of Music Processing Audio, Analysis, Algorithms, Applications, doi:10.1007/978-3-319-21945-5. Springer International Publishing Switzerland
32. Čuperlović-Culf M (2013) 4 - Metabolomics NMR data preprocessing – analysis of individual spectrum. In: Čuperlović-Culf M (ed) NMR Metabolomics in Cancer Research, doi:https://doi.org/10.1533/9781908818263.215. Woodhead Publishing, pp 215-259.
33. Moratal D, Vallés-Luch A, Martí-Bonmatí L, Brummer M (2008) k-Space tutorial: an MRI educational tool for a better understanding of k-space. Biomed Imaging Interv J (1823-5530 (Print)).
34. Wright KL, Hamilton JI, Griswold MA, Gulani V, Seiberlich N (2014) Non-Cartesian parallel imaging reconstruction. J Magn Reson Imaging 40 (5):1022-1040.
35. Krafft AJ, Loeffler RB, Song R, Tipirneni-Sajja A, McCarville MB, Robson MD, Hankins JS, Hillenbrand CM (2017) Quantitative ultrashort echo time imaging for assessment of massive iron overload at 1.5 and 3 Tesla. Magn Reson Med 78 (5):1839-1851.
36. Mahesh M (2013) Magnetic Resonance Basics: Magnetic Fields, Nuclear Magnetic Characteristics, Tissue Contrast, Image Acquisition. In: The Essential Physics of Medical

Imaging, Third Edition doi:10.1118/1.4811156 American Association of Physicists in Medicine, Medical Physics.
37. Henninger B, Alustiza J, Garbowski M, Gandon Y (2020) Practical guide to quantification of hepatic iron with MRI. Eur Radiol 30 (1):383-393.
38. Elster AD (1993) Gradient-echo MR imaging: techniques and acronyms. Radiology 186 (1):1-8.
39. Markl M, Leupold J (2012) Gradient echo imaging. J Magn Reson Imaging 35 (6):1274-1289.
40. Liu J, Christiansen SD, Drangova M (2018) Single multi-echo GRE acquisition with short and long echo spacing for simultaneous quantitative mapping of fat fraction, B0 inhomogeneity, and susceptibility. Neuroimage 172:703-717.
41. Kafali SG, Armstrong T, Shih SF, Kim GJ, Holtrop JL, Venick RS, Ghahremani S, Bolster BD, Jr., Hillenbrand CM, Calkins KL, Wu HH (2022) Free-breathing radial magnetic resonance elastography of the liver in children at 3 T: a pilot study. Pediatr Radiol 52 (7):1314-1325.
42. Tipirneni-Sajja A, Loeffler RB, Krafft AJ, Sajewski AN, Ogg RJ, Hankins JS, Hillenbrand CM (2019) Ultrashort echo time imaging for quantification of hepatic iron overload: Comparison of acquisition and fitting methods via simulations, phantoms, and in vivo data. J Magn Reson Imaging 49 (5):1475-1488.
43. Robson MD, Gatehouse PD, Bydder M, Bydder GM (2003) Magnetic resonance: an introduction to ultrashort TE (UTE) imaging. J Comput Assist Tomogr 27 (6):825-846.
44. Tipirneni-Sajja A, Krafft AJ, Loeffler RB, Song R, Bahrami A, Hankins JS, Hillenbrand CM (2019) Autoregressive moving average modeling for hepatic iron quantification in the presence of fat. J Magn Reson Imaging 50 (5):1620-1632.
45. Cho YJ, Kim WS, Choi YH, Lee SB, Lee S, Cheon JE, Paek M, Woo S (2020) Validation and feasibility of liver T1 mapping using free breathing MOLLI sequence in children and young adults. Sci Rep 10 (1):18390.
46. Sirlin CB, Reeder SB (2010) Magnetic resonance imaging quantification of liver iron. Magn Reson Imaging Clin N Am 18 (3):359-381, ix.
47. Lazo M, Hernaez R, Eberhardt MS, Bonekamp S, Kamel I, Guallar E, Koteish A, Brancati FL, Clark JM (2013) Prevalence of nonalcoholic fatty liver disease in the United States: the Third National Health and Nutrition Examination Survey, 1988-1994. American journal of epidemiology 178 (1):38-45.
48. Janiszewski PM, Oeffinger KC, Church TS, Dunn AL, Eshelman DA, Victor RG, Brooks S, Turoff AJ, Sinclair E, Murray JC, Bashore L, Ross R (2007) Abdominal obesity, liver fat, and muscle composition in survivors of childhood acute lymphoblastic leukemia. J Clin Endocrinol Metab 92 (10):3816-3821.
49. Harris R, Harman DJ, Card TR, Aithal GP, Guha IN (2017) Prevalence of clinically significant liver disease within the general population, as defined by non-invasive markers of liver fibrosis: a systematic review. Lancet Gastroenterol Hepatol 2 (4):288-297.
50. St Pierre TG, El-Beshlawy A, Elalfy M, Al Jefri A, Al Zir K, Daar S, Habr D, Kriemler-Krahn U, Taher A (2014) Multicenter validation of spin-density projection-assisted R2-MRI for the noninvasive measurement of liver iron concentration. Magn Reson Med 71 (6):2215-2223.
51. Zhao R, Hernando D, Harris DT, Hinshaw LA, Li K, Ananthakrishnan L, Bashir MR, Duan X, Ghasabeh MA, Kamel IR, Lowry C, Mahesh M, Marin D, Miller J, Pickhardt PJ, Shaffer J, Yokoo T, Brittain JH, Reeder SB (2021) Multisite multivendor validation of a quantitative MRI and CT compatible fat phantom. Med Phys 48 (8):4375-4386.

52. Hernando D, Sharma SD, Aliyari Ghasabeh M, Alvis BD, Arora SS, Hamilton G, Pan L, Shaffer JM, Sofue K, Szeverenyi NM, Welch EB, Yuan Q, Bashir MR, Kamel IR, Rice MJ, Sirlin CB, Yokoo T, Reeder SB (2017) Multisite, multivendor validation of the accuracy and reproducibility of proton-density fat-fraction quantification at 1.5T and 3T using a fat-water phantom. Magn Reson Med 77 (4):1516-1524.
53. Pickhardt PJ, Graffy PM, Reeder SB, Hernando D, Li K (2018) Quantification of Liver Fat Content With Unenhanced MDCT: Phantom and Clinical Correlation With MRI Proton Density Fat Fraction. AJR Am J Roentgenol 211 (3):W151-W157.
54. Hu HH, Yokoo T, Bashir MR, Sirlin CB, Hernando D, Malyarenko D, Chenevert TL, Smith MA, Serai SD, Middleton MS, Henderson WC, Hamilton G, Shaffer J, Shu Y, Tkach JA, Trout AT, Obuchowski N, Brittain JH, Jackson EF, Reeder SB, Committee RQIBAPB (2021) Linearity and Bias of Proton Density Fat Fraction as a Quantitative Imaging Biomarker: A Multicenter, Multiplatform, Multivendor Phantom Study. Radiology 298 (3):640-651.
55. Ehman RL (2022) Magnetic resonance elastography: from invention to standard of care. Abdom Radiol (NY) 47 (9):3028-3036.
56. Shukla-Dave A, Obuchowski NA, Chenevert TL, Jambawalikar S, Schwartz LH, Malyarenko D, Huang W, Noworolski SM, Young RJ, Shiroishi MS, Kim H, Coolens C, Laue H, Chung C, Rosen M, Boss M, Jackson EF (2019) Quantitative imaging biomarkers alliance (QIBA) recommendations for improved precision of DWI and DCE-MRI derived biomarkers in multicenter oncology trials. J Magn Reson Imaging 49 (7):e101-e121.
57. QIBA MR Biomarker Committee. MR Elastography of the Liver, Quantitative Imaging Biomarekrs Alliance. Profile Stage: Technically Confirmed. February 14, 2022. Available from: https://qibawikirsnaorg/indexphp/Profiles.
58. Hellerbach A, Schuster V, Jansen A, Sommer J (2013) MRI phantoms - are there alternatives to agar? PLoS One 8 (8):e70343.
59. Krafft AJ, Loeffler RB, Song R, Bian X, McCarville MB, Hankins JS, Hillenbrand CM (2016) Does fat suppression via chemically selective saturation affect R2*-MRI for transfusional iron overload assessment? A clinical evaluation at 1.5T and 3T. Magn Reson Med 76 (2):591-601.
60. Hong W, He Q, Fan S, Carl M, Shao H, Chen J, Chang EY, Du J (2017) Imaging and quantification of iron-oxide nanoparticles (IONP) using MP-RAGE and UTE based sequences. Magn Reson Med 78 (1):226-232.
61. Hines CD, Yu H, Shimakawa A, McKenzie CA, Brittain JH, Reeder SB (2009) T1 independent, T2* corrected MRI with accurate spectral modeling for quantification of fat: validation in a fat-water-SPIO phantom. J Magn Reson Imaging 30 (5):1215-1222.
62. Oudry J, Chen J, Glaser KJ, Miette V, Sandrin L, Ehman RL (2009) Cross-validation of magnetic resonance elastography and ultrasound-based transient elastography: a preliminary phantom study. J Magn Reson Imaging 30 (5):1145-1150.
63. Jiang K, Ferguson CM, Ebrahimi B, Tang H, Kline TL, Burningham TA, Mishra PK, Grande JP, Macura SI, Lerman LO (2017) Noninvasive Assessment of Renal Fibrosis with Magnetization Transfer MR Imaging: Validation and Evaluation in Murine Renal Artery Stenosis. Radiology 283 (1):77-86.
64. Alustiza JM, Emparanza JI, Castiella A, Casado A, Garrido A, Aldazabal P, San Vicente M, Garcia N, Asensio AB, Banales J, Salvador E, Moyua A, Arozena X, Zarco M, Jauregui L, Vicente O (2015) Measurement of liver iron concentration by MRI is reproducible. Biomed Res Int 2015:294024.

65. Morisaka H, Motosugi U, Glaser KJ, Ichikawa S, Ehman RL, Sano K, Ichikawa T, Onishi H (2017) Comparison of diagnostic accuracies of two- and three-dimensional MR elastography of the liver. J Magn Reson Imaging 45 (4):1163-1170.
66. Reeder SB, Robson PM, Yu H, Shimakawa A, Hines CD, McKenzie CA, Brittain JH (2009) Quantification of hepatic steatosis with MRI: the effects of accurate fat spectral modeling. Journal of Magnetic Resonance Imaging: An Official Journal of the International Society for Magnetic Resonance in Medicine 29 (6):1332-1339.
67. Hernando D, Liang ZP, Kellman P (2010) Chemical shift–based water/fat separation: A comparison of signal models. Magnetic resonance in medicine 64 (3):811-822.
68. Zhao R, Hamilton G, Brittain JH, Reeder SB, Hernando D (2021) Design and evaluation of quantitative MRI phantoms to mimic the simultaneous presence of fat, iron, and fibrosis in the liver. Magn Reson Med 85 (2):734-747.
69. Ahmad MS, Makhamrah O, Suardi N, Shukri A, Razak NNANA, Mohammad H (2021) Agarose and Wax Tissue-Mimicking Phantom for Dynamic Magnetic Resonance Imaging of the Liver. Journal of Medical - Clinical Research & Reviews 5 (12):11.
70. In E, Naguib H, Haider M (2014) Mechanical stability analysis of carrageenan-based polymer gel for magnetic resonance imaging liver phantom with lesion particles. J Med Imaging (Bellingham) 1 (3):035502.
71. Keenan KE, Ainslie M, Barker AJ, Boss MA, Cecil KM, Charles C, Chenevert TL, Clarke L, Evelhoch JL, Finn P, Gembris D, Gunter JL, Hill DLG, Jack CR, Jr., Jackson EF, Liu G, Russek SE, Sharma SD, Steckner M, Stupic KF, Trzasko JD, Yuan C, Zheng J (2018) Quantitative magnetic resonance imaging phantoms: A review and the need for a system phantom. Magn Reson Med 79 (1):48-61.
72. Stupic KF, Ainslie M, Boss MA, Charles C, Dienstfrey AM, Evelhoch JL, Finn P, Gimbutas Z, Gunter JL, Hill DLG, Jack CR, Jackson EF, Karaulanov T, Keenan KE, Liu G, Martin MN, Prasad PV, Rentz NS, Yuan C, Russek SE (2021) A standard system phantom for magnetic resonance imaging. Magn Reson Med 86 (3):1194-1211.
73. Kato H, Kuroda M, Yoshimura K, Yoshida A, Hanamoto K, Kawasaki S, Shibuya K, Kanazawa S (2005) Composition of MRI phantom equivalent to human tissues. Med Phys 32 (10):3199-3208.
74. Hoffman DH, Ayoola A, Nickel D, Han F, Chandarana H, Shanbhogue KP (2020) T1 mapping, T2 mapping and MR elastography of the liver for detection and staging of liver fibrosis. Abdom Radiol (NY) 45 (3):692-700.
75. Obmann VC, Mertineit N, Marx C, Berzigotti A, Ebner L, Heverhagen JT, Christe A, Huber AT (2019) Liver MR relaxometry at 3T - segmental normal T1 and T2* values in patients without focal or diffuse liver disease and in patients with increased liver fat and elevated liver stiffness. Sci Rep 9 (1):8106.
76. Ahmad MS, Suardi N, Shukri A, Mohammad H, Oglat AA, Alarab A, Makhamrah O (2020) Chemical Characteristics, Motivation and Strategies in choice of Materials used as Liver Phantom: A Literature Review. J Med Ultrasound 28 (1):7-16.
77. Mathur-De Vre R, Grimee R, Parmentier F, Binet J (1985) The use of agar gel as a basic reference material for calibrating relaxation times and imaging parameters. Magn Reson Med 2 (2):176-179.
78. Yoshimura K, Kato H, Kuroda M, Yoshida A, Hanamoto K, Tanaka A, Tsunoda M, Kanazawa S, Shibuya K, Kawasaki S, Hiraki Y (2003) Development of a tissue-equivalent MRI phantom using carrageenan gel. Magn Reson Med 50 (5):1011-1017.

79. Mobini N, Malekzadeh M, Haghighatkhah H, Saligheh Rad H (2020) A hybrid (iron-fat-water) phantom for liver iron overload quantification in the presence of contaminating fat using magnetic resonance imaging. MAGMA 33 (3):385-392.
80. Szurowska E, Sikorska K, Izycka-Swieszewska E, Nowicki T, Romanowski T, Bielawski KP, Studniarek M (2010) The role of MR imaging in detection of hepatic iron overload in patients with cirrhosis of different origins. BMC Gastroenterol 10:13.
81. Chang JS, Taouli B, Salibi N, Hecht EM, Chin DG, Lee VS (2006) Opposed-phase MRI for fat quantification in fat-water phantoms with 1H MR spectroscopy to resolve ambiguity of fat or water dominance. AJR Am J Roentgenol 187 (1):W103-106.
82. Hernando D, Levin YS, Sirlin CB, Reeder SB (2014) Quantification of liver iron with MRI: state of the art and remaining challenges. J Magn Reson Imaging 40 (5):1003-1021.
83. Pietrangelo A (2004) Hereditary hemochromatosis--a new look at an old disease. N Engl J Med 350 (23):2383-2397.
84. Franca M, Alberich-Bayarri A, Marti-Bonmati L, Oliveira P, Costa FE, Porto G, Vizcaino JR, Gonzalez JS, Ribeiro E, Oliveira J, Pessegueiro Miranda H (2017) Accurate simultaneous quantification of liver steatosis and iron overload in diffuse liver diseases with MRI. Abdom Radiol (NY) 42 (5):1434-1443.
85. Berdoukas V, Bohane T, Tobias V, De Silva K, Fraser I, Aessopos A, Lindeman R (2005) Liver iron concentration and fibrosis in a cohort of transfusion-dependent patients on long-term desferrioxamine therapy. Hematol J 5 (7):572-578.
86. Brown K, Subramony C, May W, Megason G, Liu H, Bishop P, Walker T, Nowicki MJ (2009) Hepatic iron overload in children with sickle cell anemia on chronic transfusion therapy. J Pediatr Hematol Oncol 31 (5):309-312.
87. Risdon RA, Barry M, Flynn DM (1975) Transfusional iron overload: the relationship between tissue iron concentration and hepatic fibrosis in thalassaemia. J Pathol 116 (2):83-95.
88. Thakerngpol K, Fucharoen S, Boonyaphipat P, Srisook K, Sahaphong S, Vathanophas V, Stitnimankarn T (1996) Liver injury due to iron overload in thalassemia: histopathologic and ultrastructural studies. Biometals 9 (2):177-183.
89. Chmieliauskas S, Banionis D, Laima S, Andriuskeviciute G, Mazeikiene S, Stasiuniene J, Jasulaitis A, Jarmalaite S (2017) Autopsy relevance determining hemochromatosis: Case report. Medicine (Baltimore) 96 (49):e8788.
90. Iancu TC, Deugnier Y, Halliday JW, Powell LW, Brissot P (1997) Ultrastructural sequences during liver iron overload in genetic hemochromatosis. J Hepatol 27 (4):628-638.
91. Wood JC, Fassler JD, Meade T (2004) Mimicking liver iron overload using liposomal ferritin preparations. Magn Reson Med 51 (3):607-611.
92. Guindi M (2011) Hemochromatosis. In: Saxena R (ed) Practical Hepatic Pathology: A Diagnostic Approach, doi:https://doi.org/10.1016/B978-0-443-06803-4.00014-9. W.B. Saunders, pp 177-189.
93. Ghugre NR (2008) Calibration of iron-mediated MRI relaxation by Monte Carlo modeling.
94. Brittenham GM, Badman DG (2003) Noninvasive measurement of iron: report of an NIDDK workshop. Blood, The Journal of the American Society of Hematology 101 (1):15-19.
95. Wortmann AC, Froehlich PE, Pinto RB, Magalhães RB, Alvares-da-Silva MR, Ferreira JJ, Silveira TR (200) Hepatic iron quantification by atomic absorption spectrophotometry: Full validation of an analytical methodusing a fast sample preparation. Spectroscopy 21:161-167.
96. Henninger B (2018) Demystifying liver iron concentration measurements with MRI. Eur Radiol 28 (6):2535-2536.

97. St Pierre TG, Clark PR, Chua-anusorn W, Fleming AJ, Jeffrey GP, Olynyk JK, Pootrakul P, Robins E, Lindeman R (2005) Noninvasive measurement and imaging of liver iron concentrations using proton magnetic resonance. Blood 105 (2):855-861.
98. Alexopoulou E, Stripeli F, Baras P, Seimenis I, Kattamis A, Ladis V, Efstathopoulos E, Brountzos EN, Kelekis AD, Kelekis NL (2006) R2 relaxometry with MRI for the quantification of tissue iron overload in beta-thalassemic patients. Journal of magnetic resonance imaging : JMRI 23 (2):163-170.
99. Bonny JM, Zanca M, Boire JY, Veyre A (1996) T2 maximum likelihood estimation from multiple spin-echo magnitude images. Magnetic resonance in medicine : official journal of the Society of Magnetic Resonance in Medicine / Society of Magnetic Resonance in Medicine 36 (2):287-293.
100. Voskaridou E, Douskou M, Terpos E, Papassotiriou I, Stamoulakatou A, Ourailidis A, Loutradi A, Loukopoulos D (2004) Magnetic resonance imaging in the evaluation of iron overload in patients with beta thalassaemia and sickle cell disease. British journal of haematology 126 (5):736-742.
101. Chandarana H, Lim RP, Jensen JH, Hajdu CH, Losada M, Babb JS, Huffman S, Taouli B (2009) Hepatic iron deposition in patients with liver disease: preliminary experience with breath-hold multiecho T2*-weighted sequence. AJR American journal of roentgenology 193 (5):1261-1267.
102. Westwood M, Anderson LJ, Firmin DN, Gatehouse PD, Charrier CC, Wonke B, Pennell DJ (2003) A single breath-hold multiecho T2* cardiovascular magnetic resonance technique for diagnosis of myocardial iron overload. Journal of magnetic resonance imaging : JMRI 18 (1):33-39.
103. Wood JC, Enriquez C, Ghugre N, Tyzka JM, Carson S, Nelson MD, Coates TD (2005) MRI R2 and R2* mapping accurately estimates hepatic iron concentration in transfusion-dependent thalassemia and sickle cell disease patients. Blood 106 (4):1460-1465.
104. St Pierre TG, Clark PR, Chua-anusorn W, Fleming AJ, Jeffrey GP, Olynyk JK, Pootrakul P, Robins E, Lindeman R (2005) Noninvasive measurement and imaging of liver iron concentrations using proton magnetic resonance. Blood 105 (2):855-861.
105. Doyle EK, Toy K, Valdez B, Chia JM, Coates T, Wood JC (2018) Ultra-short echo time images quantify high liver iron. Magn Reson Med 79 (3):1579-1585.
106. Sharma P, Altbach M, Galons JP, Kalb B, Martin DR (2014) Measurement of liver fat fraction and iron with MRI and MR spectroscopy techniques. Diagn Interv Radiol 20 (1):17-26.
107. Taylor BA, Loeffler RB, Song R, McCarville MB, Hankins JS, Hillenbrand CM (2012) Simultaneous field and R2 mapping to quantify liver iron content using autoregressive moving average modeling. Journal of magnetic resonance imaging : JMRI 35 (5):1125-1132.
108. Wang Y (2012) Principles of magnetic resonance imaging: Physics concepts, pulse sequences, and biomedical applications. CreateSpace Independent Publishing Platform,
109. Liu C, Li W, Tong KA, Yeom KW, Kuzminski S (2015) Susceptibility-weighted imaging and quantitative susceptibility mapping in the brain. J Magn Reson Imaging 42 (1):23-41.
110. Dong J, Liu T, Chen F, Zhou D, Dimov A, Raj A, Cheng Q, Spincemaille P, Wang Y (2015) Simultaneous phase unwrapping and removal of chemical shift (SPURS) using graph cuts: application in quantitative susceptibility mapping. IEEE Trans Med Imaging 34 (2):531-540.

111. Liu T, Khalidov I, de Rochefort L, Spincemaille P, Liu J, Tsiouris AJ, Wang Y (2011) A novel background field removal method for MRI using projection onto dipole fields (PDF). NMR Biomed 24 (9):1129-1136.
112. Liu T, Liu J, de Rochefort L, Spincemaille P, Khalidov I, Ledoux JR, Wang Y (2011) Morphology enabled dipole inversion (MEDI) from a single-angle acquisition: comparison with COSMOS in human brain imaging. Magn Reson Med 66 (3):777-783.
113. Tipirneni-Sajja A, Loeffler RB, Hankins JS, Morin C, Hillenbrand CM (2021) Quantitative Susceptibility Mapping Using a Multispectral Autoregressive Moving Average Model to Assess Hepatic Iron Overload. J Magn Reson Imaging 54 (3):721-727.
114. Sharma SD, Hernando D, Horng DE, Reeder SB (2015) Quantitative susceptibility mapping in the abdomen as an imaging biomarker of hepatic iron overload. Magn Reson Med 74 (3):673-683.
115. Sharma SD, Fischer R, Schoennagel BP, Nielsen P, Kooijman H, Yamamura J, Adam G, Bannas P, Hernando D, Reeder SB (2017) MRI-based quantitative susceptibility mapping (QSM) and R2* mapping of liver iron overload: Comparison with SQUID-based biomagnetic liver susceptometry. Magn Reson Med 78 (1):264-270.
116. Lin H, Wei H, He N, Fu C, Cheng S, Shen J, Wang B, Yan X, Liu C, Yan F (2018) Quantitative susceptibility mapping in combination with water-fat separation for simultaneous liver iron and fat fraction quantification. Eur Radiol 28 (8):3494-3504.
117. Li J, Lin H, Liu T, Zhang Z, Prince MR, Gillen K, Yan X, Song Q, Hua T, Zhao X, Zhang M, Zhao Y, Li G, Tang G, Yang G, Brittenham GM, Wang Y (2018) Quantitative susceptibility mapping (QSM) minimizes interference from cellular pathology in R2* estimation of liver iron concentration. J Magn Reson Imaging 48 (4):1069-1079.
118. Zhu A, Colgan TJ, Reeder SB, Hernando D Test-retest Repeatability of R2* Mapping and Quantitative Susceptibility Mapping for Liver Iron Quantification. In: Joint Annual Meeting ISMRM-ESMRMB, Paris, 2018.
119. Birkl C, Birkl-Toeglhofer AM, Kames C, Goessler W, Haybaeck J, Fazekas F, Ropele S, Rauscher A (2020) The influence of iron oxidation state on quantitative MRI parameters in post mortem human brain. Neuroimage 220:117080.
120. Baldock C, Harris PJ, Piercy AR, Healy B (2001) Experimental determination of the diffusion coefficient in two-dimensions in ferrous sulphate gels using the finite element method. Australas Phys Eng Sci Med 24 (1):19-30.
121. Ibrahim EH, Khalifa AM, Eldaly AK (2016) MRI T2* imaging for assessment of liver iron overload: study of different data analysis approaches. Acta Radiol 57 (12):1453-1459.
122. Chandarana H, Do RK, Mussi TC, Jensen JH, Hajdu CH, Babb JS, Taouli B (2012) The effect of liver iron deposition on hepatic apparent diffusion coefficient values in cirrhosis. AJR Am J Roentgenol 199 (4):803-808.
123. Tsai YS, Chen JS, Wang CK, Lu CH, Cheng CN, Kuo CS, Liu YS, Tsai HM (2014) Quantitative assessment of iron in heart and liver phantoms using dual-energy computed tomography. Exp Ther Med 8 (3):907-912.
124. Yokoo T, Yuan Q, Senegas J, Wiethoff AJ, Pedrosa I (2015) Quantitative R2* MRI of the liver with rician noise models for evaluation of hepatic iron overload: Simulation, phantom, and early clinical experience. J Magn Reson Imaging 42 (6):1544-1559.
125. Guimaraes AR, Siqueira L, Uppal R, Alford J, Fuchs BC, Yamada S, Tanabe K, Chung RT, Lauwers G, Chew ML, Boland GW, Sahani DV, Vangel M, Hahn PF, Caravan P (2016) T2 relaxation time is related to liver fibrosis severity. Quant Imaging Med Surg 6 (2):103-114.

126. Brown GC, Cowin GJ, Galloway GJ (2017) A USPIO doped gel phantom for R2* relaxometry. MAGMA 30 (1):15-27.
127. Lu X, Ma Y, Chang EY, He Q, Searleman A, von Drygalski A, Du J (2018) Simultaneous quantitative susceptibility mapping (QSM) and R2* for high iron concentration quantification with 3D ultrashort echo time sequences: An echo dependence study. Magn Reson Med 79 (4):2315-2322.
128. Headley AM, Grice JV, Pickens DR (2020) Reproducibility of liver iron concentration estimates in MRI through R2* measurement determined by least-squares curve fitting. J Appl Clin Med Phys 21 (12):295-303.
129. Nath S, Kaittanis C, Ramachandran V, Dalal N, Perez JM (2009) Synthesis, magnetic characterization and sensing applications of novel dextran-coated iron oxide nanorods. Chem Mater 21 (8):1761-1767.
130. Predescu AM, Matei E, Berbecaru AC, Pantilimon C, Dragan C, Vidu R, Predescu C, Kuncser V (2018) Synthesis and characterization of dextran-coated iron oxide nanoparticles. R Soc Open Sci 5 (3):171525.
131. Lee SS, Lee Y, Kim N, Kim SW, Byun JH, Park SH, Lee MG, Ha HK (2011) Hepatic fat quantification using chemical shift MR imaging and MR spectroscopy in the presence of hepatic iron deposition: validation in phantoms and in patients with chronic liver disease. J Magn Reson Imaging 33 (6):1390-1398.
132. Wang YX (2011) Superparamagnetic iron oxide based MRI contrast agents: Current status of clinical application. Quant Imaging Med Surg 1 (1):35-40.
133. Xiao YD, Paudel R, Liu J, Ma C, Zhang ZS, Zhou SK (2016) MRI contrast agents: Classification and application (Review). Int J Mol Med 38 (5):1319-1326.
134. Pan D, Schmieder AH, Wickline SA, Lanza GM (2011) Manganese-based MRI contrast agents: past, present and future. Tetrahedron 67 (44):8431-8444.
135. Kee Y, Sandino CM, Syed AB, Cheng JY, Shimakawa A, Colgan TJ, Hernando D, Vasanawala SS (2021) Free-breathing R 2 * mapping of hepatic iron overload in children using 3D multi-echo UTE cones MRI. Magn Reson Med 85 (5):2608-2621.
136. Younossi Z, Tacke F, Arrese M, Chander Sharma B, Mostafa I, Bugianesi E, Wai-Sun Wong V, Yilmaz Y, George J, Fan J (2019) Global perspectives on nonalcoholic fatty liver disease and nonalcoholic steatohepatitis. Hepatology 69 (6):2672-2682.
137. Bellentani S, Saccoccio G, Masutti F, Crocè LS, Brandi G, Sasso F, Cristanini G, Tiribelli C (2000) Prevalence of and risk factors for hepatic steatosis in Northern Italy. Annals of Internal Medicine 132 (2):112-117.
138. Browning JD, Szczepaniak LS, Dobbins R, Nuremberg P, Horton JD, Cohen JC, Grundy SM, Hobbs HH (2004) Prevalence of hepatic steatosis in an urban population in the United States: impact of ethnicity. Hepatology 40 (6):1387-1395.
139. Ekstedt M, Nasr P, Kechagias S (2017) Natural history of NAFLD/NASH. Current hepatology reports 16 (4):391-397.
140. Zezos P, Renner EL (2014) Liver transplantation and non-alcoholic fatty liver disease. World journal of gastroenterology: WJG 20 (42):15532.
141. Lai J, Wang HL, Zhang X, Wang H, Liu X (2022) Pathologic Diagnosis of Nonalcoholic Fatty Liver Disease. Archives of Pathology & Laboratory Medicine 146 (8):940-946.
142. Tanikawa K (1968) Ultrastructural aspects of the liver and its disorders. Tokyo: Igaku Shoin Ltd., 5-29-11 Hongo Bunkyo-ku, Tokyo, Japan. Berlin, etc.: Springer-Verlag,

143. Kleiner DE, Brunt EM, Van Natta M, Behling C, Contos MJ, Cummings OW, Ferrell LD, Liu YC, Torbenson MS, Unalp-Arida A (2005) Design and validation of a histological scoring system for nonalcoholic fatty liver disease. Hepatology 41 (6):1313-1321.
144. Szczepaniak LS, Nurenberg P, Leonard D, Browning JD, Reingold JS, Grundy S, Hobbs HH, Dobbins RL (2005) Magnetic resonance spectroscopy to measure hepatic triglyceride content: prevalence of hepatic steatosis in the general population. Am J Physiol Endocrinol Metab 288 (2):E462-468.
145. Caussy C, Reeder SB, Sirlin CB, Loomba R (2018) Noninvasive, Quantitative Assessment of Liver Fat by MRI-PDFF as an Endpoint in NASH Trials. Hepatology 68 (2):763-772.
146. Hernando D, Sharma SD, Kramer H, Reeder SB (2014) On the confounding effect of temperature on chemical shift-encoded fat quantification. Magn Reson Med 72 (2):464-470.
147. Navaratna R, Zhao R, Colgan TJ, Hu HH, Bydder M, Yokoo T, Bashir MR, Middleton MS, Serai SD, Malyarenko D, Chenevert T, Smith M, Henderson W, Hamilton G, Shu Y, Sirlin CB, Tkach JA, Trout AT, Brittain JH, Hernando D, Reeder SB, Committee RQIBA-PDFFB (2021) Temperature-corrected proton density fat fraction estimation using chemical shift-encoded MRI in phantoms. Magn Reson Med 86 (1):69-81.
148. Tognarelli JM, Dawood M, Shariff MI, Grover VP, Crossey MM, Cox IJ, Taylor-Robinson SD, McPhail MJ (2015) Magnetic Resonance Spectroscopy: Principles and Techniques: Lessons for Clinicians. J Clin Exp Hepatol 5 (4):320-328.
149. Bydder M, Girard O, Hamilton G (2011) Mapping the double bonds in triglycerides. Magn Reson Imaging 29 (8):1041-1046.
150. Hamilton G, Yokoo T, Bydder M, Cruite I, Schroeder ME, Sirlin CB, Middleton MS (2011) In vivo characterization of the liver fat (1)H MR spectrum. NMR Biomed 24 (7):784-790.
151. Kurhanewicz J, Vigneron DB, Nelson SJ (2000) Three-dimensional magnetic resonance spectroscopic imaging of brain and prostate cancer. Neoplasia 2 (1-2):166-189.
152. Cassidy FH, Yokoo T, Aganovic L, Hanna RF, Bydder M, Middleton MS, Hamilton G, Chavez AD, Schwimmer JB, Sirlin CB (2009) Fatty liver disease: MR imaging techniques for the detection and quantification of liver steatosis. Radiographics 29 (1):231-260.
153. Omoumi P (2022) The Dixon method in musculoskeletal MRI: from fat-sensitive to fat-specific imaging. Skeletal Radiol 51 (7):1365-1369.
154. Hayashi T, Saitoh S, Takahashi J, Tsuji Y, Ikeda K, Kobayashi M, Kawamura Y, Fujii T, Inoue M, Miyati T, Kumada H (2017) Hepatic fat quantification using the two-point Dixon method and fat color maps based on non-alcoholic fatty liver disease activity score. Hepatol Res 47 (5):455-464.
155. Clarke CN, Choi H, Hou P, Davis CH, Ma J, Rashid A, Vauthey JN, Aloia TA (2017) Using MRI to non-invasively and accurately quantify preoperative hepatic steatosis. HPB (Oxford) 19 (8):706-712.
156. Pacifico L, Martino MD, Catalano C, Panebianco V, Bezzi M, Anania C, Chiesa C (2011) T1-weighted dual-echo MRI for fat quantification in pediatric nonalcoholic fatty liver disease. World J Gastroenterol 17 (25):3012-3019.
157. Kim G, Giannini C, Pierpont B, Feldstein AE, Santoro N, Kursawe R, Shaw M, Duran E, Goldberg R, Dziura J, Caprio S (2013) Longitudinal effects of MRI-measured hepatic steatosis on biomarkers of glucose homeostasis and hepatic apoptosis in obese youth. Diabetes Care 36 (1):130-136.
158. Lins CF, Salmon CEG, Nogueira-Barbosa MH (2021) Applications of the Dixon technique in the evaluation of the musculoskeletal system. Radiol Bras 54 (1):33-42.

159. Ma J (2008) Dixon techniques for water and fat imaging. J Magn Reson Imaging 28 (3):543-558.
160. Bhat V, Velandai S, Belliappa V, Illayraja J, Halli KG, Gopalakrishnan G (2017) Quantification of Liver Fat with mDIXON Magnetic Resonance Imaging, Comparison with the Computed Tomography and the Biopsy. J Clin Diagn Res 11 (7):TC06-TC10.
161. Reeder SB, Sirlin CB (2010) Quantification of liver fat with magnetic resonance imaging. Magnetic Resonance Imaging Clinics 18 (3):337-357.
162. Kuhn JP, Jahn C, Hernando D, Siegmund W, Hadlich S, Mayerle J, Pfannmoller J, Langner S, Reeder S (2014) T1 bias in chemical shift-encoded liver fat-fraction: role of the flip angle. J Magn Reson Imaging 40 (4):875-883.
163. Wang X, Colgan TJ, Hinshaw LA, Roberts NT, Bancroft LCH, Hamilton G, Hernando D, Reeder SB (2020) T1 -corrected quantitative chemical shift-encoded MRI. Magn Reson Med 83 (6):2051-2063.
164. Eggers H, Bornert P (2014) Chemical shift encoding-based water-fat separation methods. J Magn Reson Imaging 40 (2):251-268.
165. Reeder SB, Cruite I, Hamilton G, Sirlin CB (2011) Quantitative Assessment of Liver Fat with Magnetic Resonance Imaging and Spectroscopy. J Magn Reson Imaging 34 (4):729-749.
166. Henninger B, Zoller H, Kannengiesser S, Zhong X, Jaschke W, Kremser C (2017) 3D Multiecho Dixon for the Evaluation of Hepatic Iron and Fat in a Clinical Setting. J Magn Reson Imaging 46 (3):793-800.
167. Kuhn JP, Hernando D, Mensel B, Kruger PC, Ittermann T, Mayerle J, Hosten N, Reeder SB (2014) Quantitative chemical shift-encoded MRI is an accurate method to quantify hepatic steatosis. J Magn Reson Imaging 39 (6):1494-1501.
168. Yokoo T, Shiehmorteza M, Hamilton G, Wolfson T, Schroeder ME, Middleton MS, Bydder M, Gamst AC, Kono Y, Kuo A, Patton HM, Horgan S, Lavine JE, Schwimmer JB, Sirlin CB (2011) Estimation of hepatic proton-density fat fraction by using MR imaging at 3.0 T. Radiology 258 (3):749-759.
169. Idilman IS, Keskin O, Celik A, Savas B, Elhan AH, Idilman R, Karcaaltincaba M (2016) A comparison of liver fat content as determined by magnetic resonance imaging-proton density fat fraction and MRS versus liver histology in non-alcoholic fatty liver disease. Acta Radiol 57 (3):271-278.
170. Tang A, Tan J, Sun M, Hamilton G, Bydder M, Wolfson T, Gamst AC, Middleton M, Brunt EM, Loomba R, Lavine JE, Schwimmer JB, Sirlin CB (2013) Nonalcoholic fatty liver disease: MR imaging of liver proton density fat fraction to assess hepatic steatosis. Radiology 267 (2):422-431.
171. Tang A, Desai A, Hamilton G, Wolfson T, Gamst A, Lam J, Clark L, Hooker J, Chavez T, Ang BD, Middleton MS, Peterson M, Loomba R, Sirlin CB (2015) Accuracy of MR imaging-estimated proton density fat fraction for classification of dichotomized histologic steatosis grades in nonalcoholic fatty liver disease. Radiology 274 (2):416-425.
172. Beyer C, Hutton C, Andersson A, Imajo K, Nakajima A, Kiker D, Banerjee R, Dennis A (2021) Comparison between magnetic resonance and ultrasound-derived indicators of hepatic steatosis in a pooled NAFLD cohort. PLoS One 16 (4):e0249491.
173. Chebrolu VV, Hines CD, Yu H, Pineda AR, Shimakawa A, McKenzie CA, Samsonov A, Brittain JH, Reeder SB (2010) Independent estimation of T* 2 for water and fat for improved accuracy of fat quantification. Magnetic Resonance in Medicine: An Official Journal of the International Society for Magnetic Resonance in Medicine 63 (4):849-857.

174. Horng DE, Hernando D, Hines CD, Reeder SB (2013) Comparison of R2* correction methods for accurate fat quantification in fatty liver. Journal of Magnetic Resonance Imaging 37 (2):414-422.
175. Hernando D, Kramer JH, Reeder SB (2013) Multipeak fat-corrected complex R2* relaxometry: theory, optimization, and clinical validation. Magn Reson Med 70 (5):1319-1331.
176. Taylor BA, Hwang KP, Hazle JD, Stafford RJ (2009) Autoregressive moving average modeling for spectral parameter estimation from a multigradient echo chemical shift acquisition. Med Phys 36 (3):753-764.
177. Krafft AJ, Taylor BA, Lin H, Loeffler RB, Hillenbrand CM A Systematic Evaluation of an Auto Regressive Moving Average (ARMA) Model for Fat-water Quantification and Simultaneous T2* Mapping. In: International Society of Magnetic Resonance in Medicine, Salt Lake City, Utah, 2013.
178. Pooler BD, Hernando D, Ruby JA, Ishii H, Shimakawa A, Reeder SB (2018) Validation of a motion-robust 2D sequential technique for quantification of hepatic proton density fat fraction during free breathing. J Magn Reson Imaging 48 (6):1578-1585.
179. Jaubert O, Cruz G, Bustin A, Schneider T, Lavin B, Koken P, Hajhosseiny R, Doneva M, Rueckert D, Botnar RM, Prieto C (2020) Water-fat Dixon cardiac magnetic resonance fingerprinting. Magn Reson Med 83 (6):2107-2123.
180. Schneider E, Remer EM, Obuchowski NA, McKenzie CA, Ding X, Navaneethan SD (2021) Long-term inter-platform reproducibility, bias, and linearity of commercial PDFF MRI methods for fat quantification: a multi-center, multi-vendor phantom study. Eur Radiol 31 (10):7566-7574.
181. Bernard CP, Liney GP, Manton DJ, Turnbull LW, Langton CM (2008) Comparison of fat quantification methods: a phantom study at 3.0T. J Magn Reson Imaging 27 (1):192-197.
182. Peng XG, Ju S, Qin Y, Fang F, Cui X, Liu G, Ni Y, Teng GJ (2011) Quantification of liver fat in mice: comparing dual-echo Dixon imaging, chemical shift imaging, and 1H-MR spectroscopy. J Lipid Res 52 (10):1847-1855.
183. Leporq B, Lambert SA, Ronot M, Vilgrain V, Van Beers BE (2014) Quantification of the triglyceride fatty acid composition with 3.0 T MRI. NMR Biomed 27 (10):1211-1221.
184. Fukuzawa K, Hayashi T, Takahashi J, Yoshihara C, Tano M, Kotoku J, Saitoh S (2017) Evaluation of six-point modified dixon and magnetic resonance spectroscopy for fat quantification: a fat-water-iron phantom study. Radiol Phys Technol 10 (3):349-358.
185. Hayashi T, Fukuzawa K, Yamazaki H, Konno T, Miyati T, Kotoku J, Oba H, Kondo H, Toyoda K, Saitoh S (2018) Multicenter, multivendor phantom study to validate proton density fat fraction and T2* values calculated using vendor-provided 6-point DIXON methods. Clin Imaging 51:38-42.
186. Kim HJ, Cho HJ, Kim B, You MW, Lee JH, Huh J, Kim JK (2019) Accuracy and precision of proton density fat fraction measurement across field strengths and scan intervals: A phantom and human study. J Magn Reson Imaging 50 (1):305-314.
187. Mashhood A, Railkar R, Yokoo T, Levin Y, Clark L, Fox-Bosetti S, Middleton MS, Riek J, Kauh E, Dardzinski BJ, Williams D, Sirlin C, Shire NJ (2013) Reproducibility of hepatic fat fraction measurement by magnetic resonance imaging. J Magn Reson Imaging 37 (6):1359-1370.
188. Water in Mineral Oil in Water (W-O-W) Double Emulsion Production using SDS, PGPR and Tween® 80 as Emulsifiers (2019). Dolomite Microfluidics.

189. Bush EC, Gifford A, Coolbaugh CL, Towse TF, Damon BM, Welch EB (2018) Fat-Water Phantoms for Magnetic Resonance Imaging Validation: A Flexible and Scalable Protocol. J Vis Exp doi:10.3791/57704 (139).
190. Zdrali E, Etienne G, Smolentsev N, Amstad E, Roke S (2019) The interfacial structure of nano- and micron-sized oil and water droplets stabilized with SDS and Span80. J Chem Phys 150 (20):204704.
191. Wang Q, Ye F, Ma P, Chen F, Che Y, Zhao X, Yang L (2019) Quantitative magnetic resonance imaging evaluation of hepatic fat content with iron deposition: will it be disturbed? J Int Med Res 47 (5):1958-1974.
192. Fritz V, Martirosian P, Machann J, Daniels R, Schick F (2022) A comparison of emulsifiers for the formation of oil-in-water emulsions: stability of the emulsions within 9 h after production and MR signal properties. MAGMA 35 (3):401-410.
193. Nahmias Y, Berthiaume F, Yarmush ML (2007) Integration of technologies for hepatic tissue engineering. Adv Biochem Eng Biotechnol 103:309-329.
194. Khurana A, Sayed N, Allawadhi P, Weiskirchen R (2021) It's all about the spaces between cells: role of extracellular matrix in liver fibrosis. Ann Transl Med 9 (8):728.
195. Karsdal MA, Nielsen SH, Leeming DJ, Langholm LL, Nielsen MJ, Manon-Jensen T, Siebuhr A, Gudmann NS, Ronnow S, Sand JM, Daniels SJ, Mortensen JH, Schuppan D (2017) The good and the bad collagens of fibrosis - Their role in signaling and organ function. Adv Drug Deliv Rev 121:43-56.
196. Nielsen MJ, Leeming, D. J., Karsdal, M. A., & Krag, A. (2015) Biomarkers of Extracellular Matrix Remodeling in Liver Diseases. . In: Biomarkers in Liver Disease, doi:https://doi.org/10.1007/978-94-007-7675-3_14. Springer.
197. Chen G, Xia B, Fu Q, Huang X, Wang F, Chen Z, Lv Y (2019) Matrix Mechanics as Regulatory Factors and Therapeutic Targets in Hepatic Fibrosis. International Journal of Biological Sciences 15 (12):2509-2521.
198. Bazrafshan Z, Stylios GK (2019) Spinnability of collagen as a biomimetic material: A review. International Journal of Biological Macromolecules 129:693-705.
199. Civan JM (2019) Hepatic Fibrosis. merckmanuals.com/professional/hepatic-and-biliary-disorders/fibrosis-and-cirrhosis/hepatic-fibrosis.
200. Milic S, Mikolasevic I, Orlic L, Devcic E, Starcevic-Cizmarevic N, Stimac D, Kapovic M, Ristic S (2016) The Role of Iron and Iron Overload in Chronic Liver Disease. Med Sci Monit 22:2144-2151.
201. Puri P, Sanyal AJ (2012) Nonalcoholic fatty liver disease: Definitions, risk factors, and workup. Clin Liver Dis (Hoboken) 1 (4):99-103.
202. Idilman IS, Li J, Yin M, Venkatesh SK (2020) MR elastography of liver: current status and future perspectives. Abdom Radiol (NY) 45 (11):3444-3462.
203. Guglielmo FF, Venkatesh SK, Mitchell DG (2019) Liver MR Elastography Technique and Image Interpretation: Pearls and Pitfalls. Radiographics 39 (7):1983-2002.
204. Venkatesh SK, Yin M, Ehman RL (2013) Magnetic resonance elastography of liver: technique, analysis, and clinical applications. J Magn Reson Imaging 37 (3):544-555.
205. Serai SD, Yin M (2021) MR Elastography of the Abdomen: Basic Concepts. Methods Mol Biol 2216:301-323.
206. Wang Y, Ganger DR, Levitsky J, Sternick LA, McCarthy RJ, Chen ZE, Fasanati CW, Bolster B, Shah S, Zuehlsdorff S, Omary RA, Ehman RL, Miller FH (2011) Assessment of

chronic hepatitis and fibrosis: comparison of MR elastography and diffusion-weighted imaging. AJR Am J Roentgenol 196 (3):553-561.
207. Serai SD, Obuchowski NA, Venkatesh SK, Sirlin CB, Miller FH, Ashton E, Cole PE, Ehman RL (2017) Repeatability of MR Elastography of Liver: A Meta-Analysis. Radiology 285 (1):92-100.
208. Ozturk A, Olson MC, Samir AE, Venkatesh SK (2022) Liver fibrosis assessment: MR and US elastography. Abdom Radiol (NY) 47 (9):3037-3050.
209. Tang A, Cloutier G, Szeverenyi NM, Sirlin CB (2015) Ultrasound Elastography and MR Elastography for Assessing Liver Fibrosis: Part 2, Diagnostic Performance, Confounders, and Future Directions. AJR Am J Roentgenol 205 (1):33-40.
210. Yin M, Talwalkar JA, Glaser KJ, Manduca A, Grimm RC, Rossman PJ, Fidler JL, Ehman RL (2007) Assessment of hepatic fibrosis with magnetic resonance elastography. Clin Gastroenterol Hepatol 5 (10):1207-1213 e1202.
211. Akkaya HE, Erden A, Kuru Oz D, Unal S, Erden I (2018) Magnetic resonance elastography: basic principles, technique, and clinical applications in the liver. Diagn Interv Radiol 24 (6):328-335.
212. Hoodeshenas S, Yin M, Venkatesh SK (2018) Magnetic Resonance Elastography of Liver: Current Update. Top Magn Reson Imaging 27 (5):319-333.
213. Mariappan YK, Glaser KJ, Ehman RL (2010) Magnetic resonance elastography: a review. Clin Anat 23 (5):497-511.
214. Banerjee R, Pavlides M, Tunnicliffe EM, Piechnik SK, Sarania N, Philips R, Collier JD, Booth JC, Schneider JE, Wang LM, Delaney DW, Fleming KA, Robson MD, Barnes E, Neubauer S (2014) Multiparametric magnetic resonance for the non-invasive diagnosis of liver disease. J Hepatol 60 (1):69-77.
215. Tanwar S, Rhodes F, Srivastava A, Trembling PM, Rosenberg WM (2020) Inflammation and fibrosis in chronic liver diseases including non-alcoholic fatty liver disease and hepatitis C. World J Gastroenterol 26 (2):109-133.
216. Li Z, Sun J, Hu X, Huang N, Han G, Chen L, Zhou Y, Bai W, Yang X (2016) Assessment of liver fibrosis by variable flip angle T1 mapping at 3.0T. J Magn Reson Imaging 43 (3):698-703.
217. Haaf P, Garg P, Messroghli DR, Broadbent DA, Greenwood JP, Plein S (2016) Cardiac T1 Mapping and Extracellular Volume (ECV) in clinical practice: a comprehensive review. J Cardiovasc Magn Reson 18 (1):89.
218. Ding Y, Rao SX, Zhu T, Chen CZ, Li RC, Zeng MS (2015) Liver fibrosis staging using T1 mapping on gadoxetic acid-enhanced MRI compared with DW imaging. Clin Radiol 70 (10):1096-1103.
219. Heye T, Yang SR, Bock M, Brost S, Weigand K, Longerich T, Kauczor HU, Hosch W (2012) MR relaxometry of the liver: significant elevation of T1 relaxation time in patients with liver cirrhosis. Eur Radiol 22 (6):1224-1232.
220. Haimerl M, Utpatel K, Verloh N, Zeman F, Fellner C, Nickel D, Teufel A, Fichtner-Feigl S, Evert M, Stroszczynski C, Wiggermann P (2017) Gd-EOB-DTPA-enhanced MR relaxometry for the detection and staging of liver fibrosis. Sci Rep 7:41429.
221. Sheng RF, Wang HQ, Yang L, Jin KP, Xie YH, Fu CX, Zeng MS (2017) Assessment of liver fibrosis using T1 mapping on Gd-EOB-DTPA-enhanced magnetic resonance. Dig Liver Dis 49 (7):789-795.

222. Elsafty HG, El Shafey M, El Arabawy R, Mahrous MR, Dawoud TM (2021) Could native T1 mapping replace late gadolinium enhancement in the assessment of myocardial fibrosis in patients with cardiomyopathy? Egyptian Journal of Radiology and Nuclear Medicine 52 (1).
223. Mojtahed A, Kelly CJ, Herlihy AH, Kin S, Wilman HR, McKay A, Kelly M, Milanesi M, Neubauer S, Thomas EL, Bell JD, Banerjee R, Harisinghani M (2019) Reference range of liver corrected T1 values in a population at low risk for fatty liver disease-a UK Biobank sub-study, with an appendix of interesting cases. Abdom Radiol (NY) 44 (1):72-84.
224. Hoad CL, Palaniyappan N, Kaye P, Chernova Y, James MW, Costigan C, Austin A, Marciani L, Gowland PA, Guha IN, Francis ST, Aithal GP (2015) A study of T(1) relaxation time as a measure of liver fibrosis and the influence of confounding histological factors. NMR Biomed 28 (6):706-714.
225. Obmann VC, Berzigotti A, Catucci D, Ebner L, Grani C, Heverhagen JT, Christe A, Huber AT (2021) T1 mapping of the liver and the spleen in patients with liver fibrosis-does normalization to the blood pool increase the predictive value? Eur Radiol 31 (6):4308-4318.
226. Faria SC, Ganesan K, Mwangi I, Shiehmorteza M, Viamonte B, Mazhar S, Peterson M, Kono Y, Santillan C, Casola G, Sirlin CB (2009) MR imaging of liver fibrosis: current state of the art. Radiographics 29 (6):1615-1635.
227. Talwalkar JA, Yin M, Fidler JL, Sanderson SO, Kamath PS, Ehman RL (2008) Magnetic resonance imaging of hepatic fibrosis: emerging clinical applications. Hepatology 47 (1):332-342.
228. Girometti R, Furlan A, Esposito G, Bazzocchi M, Como G, Soldano F, Isola M, Toniutto P, Zuiani C (2008) Relevance of b-values in evaluating liver fibrosis: a study in healthy and cirrhotic subjects using two single-shot spin-echo echo-planar diffusion-weighted sequences. J Magn Reson Imaging 28 (2):411-419.
229. Zhu J, Zhang J, Gao JY, Li JN, Yang DW, Chen M, Zhou C, Yang ZH (2017) Apparent diffusion coefficient normalization of normal liver: Will it improve the reproducibility of diffusion-weighted imaging at different MR scanners as a new biomarker? Medicine (Baltimore) 96 (3):e5910.
230. Mostafa MA, Kamal O, Yassin A, Nagi MA, Ahmed OA, Ahmed HA (2020) The diagnostic value of normalized ADC using spleen as reference organ in assessment liver fibrosis. Egyptian Journal of Radiology and Nuclear Medicine 51 (1).
231. Shin MK, Song JS, Hwang SB, Hwang HP, Kim YJ, Moon WS (2019) Liver Fibrosis Assessment with Diffusion-Weighted Imaging: Value of Liver Apparent Diffusion Coefficient Normalization Using the Spleen as a Reference Organ. Diagnostics (Basel) 9 (3).
232. El-Hariri M, Ali TFT, Hussien HIM (2013) Apparent diffusion coefficient (ADC) in liver fibrosis: Usefulness of normalized ADC using the spleen as reference organ. The Egyptian Journal of Radiology and Nuclear Medicine 44 (3):441-451.
233. Petitclerc L, Sebastiani G, Gilbert G, Cloutier G, Tang A (2017) Liver fibrosis: Review of current imaging and MRI quantification techniques. J Magn Reson Imaging 45 (5):1276-1295.
234. Leitao HS, Doblas S, d'Assignies G, Garteiser P, Daire JL, Paradis V, Geraldes CF, Vilgrain V, Van Beers BE (2013) Fat deposition decreases diffusion parameters at MRI: a study in phantoms and patients with liver steatosis. Eur Radiol 23 (2):461-467.
235. Liu CH, Liang CC, Huang KW, Liu CJ, Chen SI, Lin JW, Hung PH, Tsai HB, Lai MY, Chen PJ, Chen JH, Chen DS, Kao JH (2011) Transient elastography to assess hepatic fibrosis in hemodialysis chronic hepatitis C patients. Clin J Am Soc Nephrol 6 (5):1057-1065.

236. Yin M, Woollard J, Wang X, Torres VE, Harris PC, Ward CJ, Glaser KJ, Manduca A, Ehman RL (2007) Quantitative assessment of hepatic fibrosis in an animal model with magnetic resonance elastography. Magn Reson Med 58 (2):346-353.
237. Solamen LM, McGarry MD, Tan L, Weaver JB, Paulsen KD (2018) Phantom evaluations of nonlinear inversion MR elastography. Phys Med Biol 63 (14):145021.
238. Rojas GS, Dies P, Tobón SH (2019) Stiffness of liver-mimicking phantom for magnetic resonance elastography.
239. Andoh F, Yue JL, Julea F, Tardieu M, Nous C, Page G, Garteiser P, Van Beers BE, Maitre X, Pellot-Barakat C (2021) Multifrequency magnetic resonance elastography for elasticity quantitation and optimal tissue discrimination: A two-platform liver fibrosis mimicking phantom study. NMR Biomed 34 (8):e4543.
240. Salameh N, Sarracanie M, Armstrong BD, Rosen MS, Comment A (2016) Overhauser-enhanced magnetic resonance elastography. NMR Biomed 29 (5):607-613.
241. Kishimoto R, Suga M, Koyama A, Omatsu T, Tachibana Y, Ebner DK, Obata T (2017) Measuring shear-wave speed with point shear-wave elastography and MR elastography: a phantom study. BMJ Open 7 (1):e013925.
242. Usumura M, Kishimoto R, Ishii K, Hotta E, Kershaw J, Higashi T, Obata T, Suga M (2021) Longitudinal stability of a multimodal visco-elastic polyacrylamide gel phantom for magnetic resonance and ultrasound shear-wave elastography. PLoS One 16 (5):e0250667.
243. Kishimoto R, Suga M, Usumura M, Iijima H, Yoshida M, Hachiya H, Shiina T, Yamakawa M, Konno K, Obata T, Yamaguchi T (2022) Shear wave speed measurement bias in a viscoelastic phantom across six ultrasound elastography systems: a comparative study with transient elastography and magnetic resonance elastography. J Med Ultrason (2001) 49 (2):143-152.
244. Girometti R, Furlan A, Bazzocchi M, Soldano F, Isola M, Toniutto P, Bitetto D, Zuiani C (2007) Diffusion-weighted MRI in evaluating liver fibrosis: a feasibility study in cirrhotic patients. Radiol Med 112 (3):394-408.
245. Cui Y, Dyvorne H, Besa C, Cooper N, Taouli B (2015) IVIM Diffusion-weighted Imaging of the Liver at 3.0T: Comparison with 1.5T. Eur J Radiol Open 2:123-128.
246. Tirkes T, Zhao X, Lin C, Stuckey AJ, Li L, Giri S, Nickel D (2019) Evaluation of variable flip angle, MOLLI, SASHA, and IR-SNAPSHOT pulse sequences for T1 relaxometry and extracellular volume imaging of the pancreas and liver. MAGMA 32 (5):559-566.
247. Meneses A, Santabarbara JM, Romero JA, Aliaga R, Maceira AM, Moratal D (2021) Determination of Non-Invasive Biomarkers for the Assessment of Fibrosis, Steatosis and Hepatic Iron Overload by MR Image Analysis. A Pilot Study. Diagnostics (Basel) 11 (7).
248. Tartaro A, Maccarone MT (2015) The utility of gadoteric acid in contrast-enhanced MRI: a review. Reports in Medical Imaging doi:10.2147/rmi.S46798.
249. Statton BK, Smith J, Finnegan ME, Koerzdoerfer G, Quest RA, Grech-Sollars M (2022) Temperature dependence, accuracy, and repeatability of T1 and T2 relaxation times for the ISMRM/NIST system phantom measured using MR fingerprinting. Magn Reson Med 87 (3):1446-1460.
250. Lewis B, Guta A, Mackey S, Gach HM, Mutic S, Green O, Kim T (2021) Evaluation of diffusion-weighted MRI and geometric distortion on a 0.35T MR-LINAC at multiple gantry angles. J Appl Clin Med Phys 22 (2):118-125.

251. Sharma P, Martin DR, Pineda N, Xu Q, Vos M, Anania F, Hu X (2009) Quantitative analysis of T2-correction in single-voxel magnetic resonance spectroscopy of hepatic lipid fraction. J Magn Reson Imaging 29 (3):629-635.
252. Boll DT, Marin D, Redmon GM, Zink SI, Merkle EM (2010) Pilot study assessing differentiation of steatosis hepatis, hepatic iron overload, and combined disease using two-point dixon MRI at 3 T: in vitro and in vivo results of a 2D decomposition technique. AJR Am J Roentgenol 194 (4):964-971.
253. Colgan TJ, Zhao R, Roberts NT, Hernando D, Reeder SB (2021) Limits of Fat Quantification in the Presence of Iron Overload. J Magn Reson Imaging 54 (4):1166-1174.
254. Thangavel K, SaritaŞ EÜ (2017) Aqueous paramagnetic solutions for MRI phantoms at 3 T:A detailed study on relaxivities. Turkish Journal of Electrical Engineering & Computer Sciences 25:2108-2121.
255. Wood JC, Otto-Duessel M, Aguilar M, Nick H, Nelson MD, Coates TD, Pollack H, Moats R (2005) Cardiac Iron Determines Cardiac T2*, T2, and T1 in the Gerbil Model of Iron Cardiomyopathy. Circulation 112 (4):535-543.
256. Henninger B, Kremser C, Rauch S, Eder R, Zoller H, Finkenstedt A, Michaely HJ, Schocke M (2012) Evaluation of MR imaging with T1 and T2* mapping for the determination of hepatic iron overload. Eur Radiol 22 (11):2478-2486.
257. Simchick G, Zhao R, Hamilton G, Reeder SB, Hernando D (2021) Spectroscopy-based multi-parametric quantification in subjects with liver iron overload at 1.5T and 3T. Magnetic Resonance in Medicine 87 (2):597-613.
258. Chebrolu VV, Hines CD, Yu H, Pineda AR, Shimakawa A, McKenzie CA, Samsonov A, Brittain JH, Reeder SB (2010) Independent estimation of T*2 for water and fat for improved accuracy of fat quantification. Magn Reson Med 63 (4):849-857.
259. Jeon M, Halbert MV, Stephen ZR, Zhang M (2021) Iron Oxide Nanoparticles as T1 Contrast Agents for Magnetic Resonance Imaging: Fundamentals, Challenges, Applications, and Prospectives. Adv Mater 33 (23):e1906539.
260. Shrestha A, Sen I, Stephen E, Premkumar P, Agarwal S, Chandran S (2012) Urinary hemosiderin: role in evaluation of chronic venous insufficiency. Veins and Lymphatics 1.
261. Hu HH, Bornert P, Hernando D, Kellman P, Ma J, Reeder S, Sirlin C (2012) ISMRM workshop on fat-water separation: insights, applications and progress in MRI. Magn Reson Med 68 (2):378-388.
262. Wood JC, Enriquez C, Ghugre N, Tyzka JM, Carson S, Nelson MD, Coates TD (2005) MRI R2 and R2* mapping accurately estimates hepatic iron concentration in transfusion-dependent thalassemia and sickle cell disease patients. Blood 106 (4):1460-1465.
263. Tang MY, Chen TW, Zhang XM, Huang XH (2014) GRE T2 *-weighted MRI: principles and clinical applications. Biomed Res Int 2014:312142.
264. Hernando D, Zhao R, Taviani V, Ghasabeh M, Pan L, Yuan Q, Ruschke S, Karampinos D, Zhong X, Mattison R, Kamel I, Pedrosa I, Vasanawala S, Yokoo T, Reeder S Liver R2* as a Biomarker of Liver Iron Concentration: Interim Results from a Multi-Center, Multi-Vendor Reproducibility Study at 1.5T and 3T. In: Proceedings 26th Scientific Meeting, Paris, France, 2018. International Sociceity for Magnetic Resonance in Medicine.
265. Menikou G, Dadakova T, Pavlina M, Bock M, Damianou C (2015) MRI compatible head phantom for ultrasound surgery. Ultrasonics 57:144-152.

Appendices

Table 6. One-way ANOVA results from lipid globules of steatosis phantoms mixed with a stir bar and homogenizer and liver biopsy samples from patients with mild to severe steatosis. A significant difference between groups was found at a p-value of 0.02587.

ANOVA

	Stir Bar	Homogenized	Biopsy	
Radius (µm):	6.859	3.204	4.062966401	4.780511095
	6.028	3.362	4.702170354	4.355492429
	5.23	3.447	7.268451196	6.665140275
	4.133	3.765	4.197894114	6.56897126
			4.441882233	4.675188192
			4.82505242	4.72726259
			9.224104445	3.846604582
			5.674506909	8.78644816
			4.372134251	4.026578345
			5.596148197	4.567648516
			7.599731753	5.707555069
			4.525249029	6.350870351
			5.186230513	5.947062098
			5.783878949	6.360781628
			4.234846866	4.442131402
			5.090082197	4.811299563
			9.785633706	7.657573946
			5.522910222	4.562867232
Skewness:	-0.287874	0.933369	1.292792	
Excess Kurtosis:	-0.596959	1.4319	1.070118	
Normality:	1	0.9533	0.0002731	
Outliers:			9.224104445	9.785633706
Mean:	5.5625	3.4445	5.5815	
S:	1.16213	0.2362	1.51874	

Source	DF	Sum of Square	Mean Square	F Statistic	P-value
Groups (between groups)	2	16.5782	8.2891	4.0007	0.02587
Error (within groups)	41	84.9488	2.0719		
Total	43	101.5269	2.3611		

Table 7. Tukey's HSD results from lipid globules of steatosis phantoms mixed with a stir bar and homogenizer and liver biopsy samples from patients with mild to severe steatosis. A significant difference was found between the biopsy and homogenized groups at a p-value of 0.01989.

Tukey's HSD

Pair	Difference	SE	Q	Lower CI	Upper CI	Critical Mean	p-value
Stir Bar- Homogenized	2.118	0.7197	2.9429	-0.357	4.593	2.475	0.1064
Stir Bar - Biopsy	0.019	0.5364	0.03541	-1.8258	1.8637	1.8447	0.9997
Biopsy - Homogenized	2.137	0.5364	3.9837	0.2922	3.9817	1.8447	0.01989

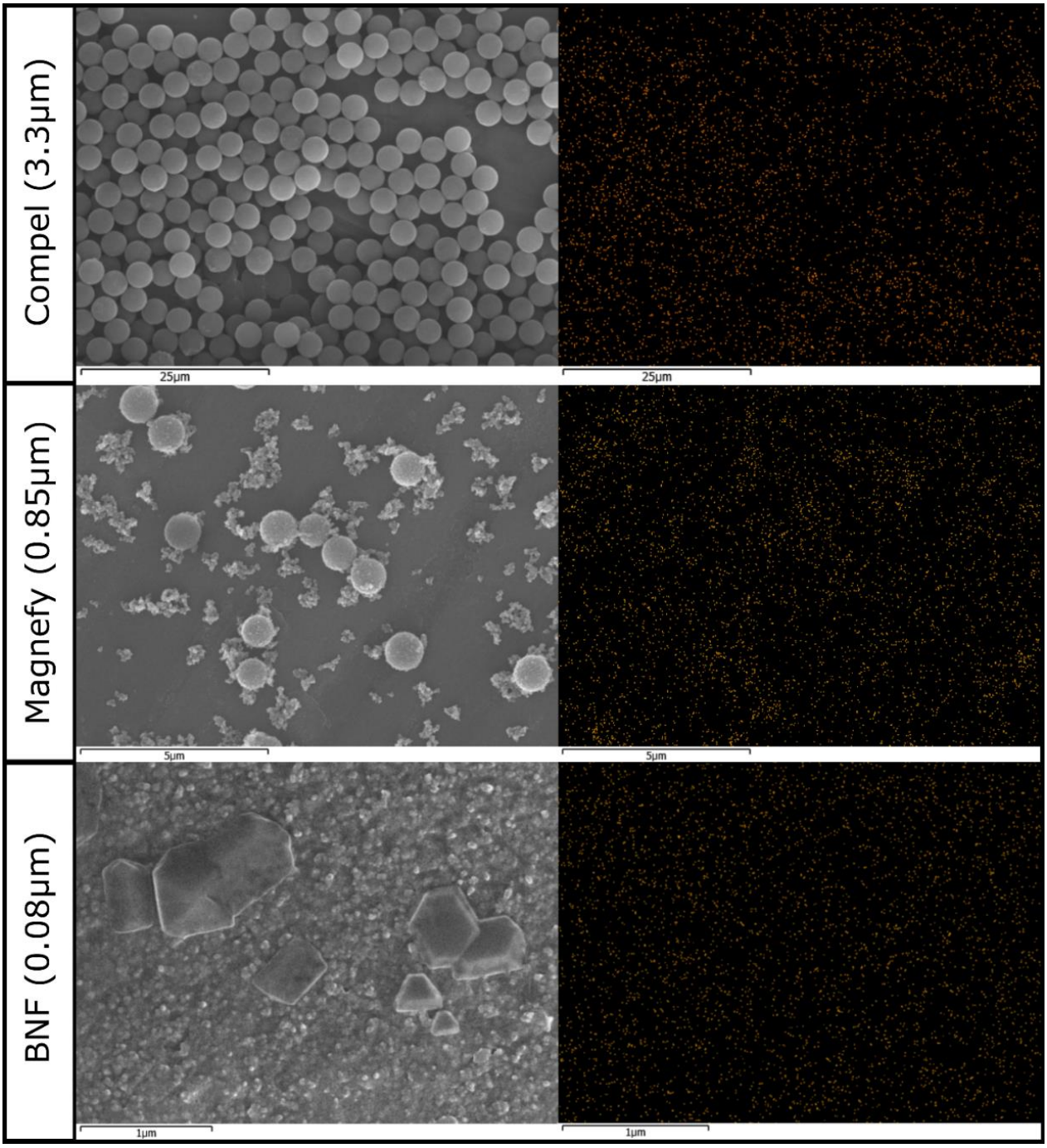

Figure 23. Scanning electron microscopy images of (top left) Compel, (middle left) Magnefy, and (bottom left) BNF iron nanoparticles are shown. Element analysis (right) was performed on each particle to confirm the presence of iron in each sample. The distribution of iron in the element analysis matches the shape of the nanoparticles, thus demonstrating the presence of iron. Notably, the large crystals shown the BNF image are composed of NaCl.

Table 8. Concentrations of oil and iron particles needed to make iron-fat phantoms of BNF concentrations 0%, 0.024%, 0.051%, 0.077%, & 0.103% and fat fractions of 0%, 10%, 20%, 30%, & 40%.

BNF		Oil Needed				
		0% FF	10% FF	20% FF	30% FF	40% FF
Iron Needed	0%	0 mL 0 µL	4.6 mL 0 µL	9.2 mL 0 µL	13.8 mL 0 µL	18.4 mL 0 µL
	0.024%	0 mL 70.3 µL	4.6 mL 70.3 µL	9.2 mL 70.3 µL	13.8 mL 70.3 µL	18.4 mL 70.3 µL
	0.051%	0 mL 146.8 µL	4.6 mL 146.8 µL	9.2 mL 146.8 µL	13.8 mL 146.8 µL	18.4 mL 146.8 µL
	0.077%	0 mL 223.3 µL	4.6 mL 223.3 µL	9.2 mL 223.3 µL	13.8 mL 223.3 µL	18.4 mL 223.3 µL
	0.103%	0 mL 299.8 µL	4.6 mL 299.8 µL	9.2 mL 299.8 µL	13.8 mL 299.8 µL	18.4 mL 299.8 µL

Table 9. Concentrations of oil and iron particles needed to make iron-fat phantoms of Magnefy concentrations 0%, 0.07%, 0.15%, 0.24%, & 0.32% and fat fractions of 0%, 10%, 20%, 30%, & 40%.

Magnefy		Oil Needed				
		0% FF	10% FF	20% FF	30% FF	40% FF
Iron Needed	0%	0 mL 0 µL	4.6 mL 0 µL	9.2 mL 0 µL	13.8 mL 0 µL	18.4 mL 0 µL
	0.07%	0 mL 70 µL	4.6 mL 70 µL	9.2 mL 70 µL	13.8 mL 70 µL	18.4 mL 70 µL
	0.15%	0 mL 153.3 µL	4.6 mL 153.3 µL	9.2 mL 153.3 µL	13.8 mL 153.3 µL	18.4 mL 153.3 µL
	0.24%	0 mL 236.6 µL	4.6 mL 236.6 µL	9.2 mL 236.6 µL	13.8 mL 236.6 µL	18.4 mL 236.6 µL
	0.32%	0 mL 320 µL	4.6 mL 320 µL	9.2 mL 320 µL	13.8 mL 320 µL	18.4 mL 320 µL

Table 10. Concentrations of oil and iron particles needed to make iron-fat phantoms of Compel concentrations 0%, 0.34%, 0.72%, 1.11%, & 1.49% and fat fractions of 0%, 10%, 20%, 30%, & 40%.

Compel		Oil Needed				
		0% FF	10% FF	20% FF	30% FF	40% FF
Iron Needed	0%	0 mL 0 µL	4.6 mL 0 µL	9.2 mL 0 µL	13.8 mL 0 µL	18.4 mL 0 µL
	0.34%	0 mL 338.4 µL	4.6 mL 338.4 µL	9.2 mL 338.4 µL	13.8 mL 338.4 µL	18.4 mL 338.4 µL
	0.72%	0 mL 723 µL	4.6 mL 723 µL	9.2 mL 723 µL	13.8 mL 723 µL	18.4 mL 723 µL
	1.11%	0 mL 1107.6 µL	4.6 mL 1107.6 µL	9.2 mL 1107.6 µL	13.8 mL 1107.6 µL	18.4 mL 1107.6 µL
	1.49%	0 mL 1492.3 µL	4.6 mL 1492.3 µL	9.2 mL 1492.3 µL	13.8 mL 1492.3 µL	18.4 mL 1492.3 µL